The Diversity of Chemical Composition and the Effects on Stellar Evolution and Planetary Habitability

by

Amanda R. Truitt

A Dissertation Presented in Partial Fulfillment
of the Requirements for the Degree
Doctor of Philosophy

Approved June 2017 by the
Graduate Supervisory Committee:

Patrick Young, Chair
Ariel Anbar
Steven Desch
Jennifer Patience
Evgenya Shkolnik

ARIZONA STATE UNIVERSITY

August 2017

ABSTRACT

I present a catalog of 1,794 stellar evolution models for solar-type and low-mass stars, which is intended to help characterize real host-stars of interest during the ongoing search for potentially habitable exoplanets. The main grid is composed of 904 tracks, for 0.5-1.2 $M_{\odot}$ at scaled metallicity values of 0.1-1.5 $Z_{\odot}$ and specific elemental abundance ratio values of 0.44-2.28 $O/Fe_{\odot}$, 0.58-1.72 $C/Fe_{\odot}$, 0.54-1.84 $Mg/Fe_{\odot}$, and 0.5-2.0 $Ne/Fe_{\odot}$. The catalog includes a small grid of late stage evolutionary tracks (25 models), as well as a grid of M-dwarf stars for 0.1-0.45 $M_{\odot}$ (856 models). The time-dependent habitable zone evolution is calculated for each track, and is strongly dependent on stellar mass, effective temperature, and luminosity parameterizations. I have also developed a subroutine for the stellar evolution code TYCHO that implements a minimalist coupled model for estimating changes in the stellar X-ray luminosity, mass loss, rotational velocity, and magnetic activity over time; to test the utility of the updated code, I created a small grid (9 models) for solar-mass stars, with variations in rotational velocity and scaled metallicity. Including this kind of information in the catalog will ultimately allow for a more robust consideration of the long-term conditions that orbiting planets may experience.

In order to gauge the true habitability potential of a given planetary system, it is extremely important to characterize the host-star's mass, specific chemical composition, and thus the timescale over which the star will evolve. It is also necessary to assess the likelihood that a planet found in the "instantaneous" habitable zone has actually had sufficient time to become "detectably" habitable. This catalog provides accurate stellar evolution predictions for a large collection of theoretical host-stars; the models are of particular utility in that they represent the real variation in stellar parameters that have been observed in nearby stars.

DEDICATION

To Alex: I could not have done this without you!

You are my best friend, cat co-herder, crossword puzzle buddy, trivia companion, and duet partner on long road trips. Thank you for always knowing how to make me laugh, for your unconditional love and support, for exploring National Parks with me, curating our movie collection, and for letting me play The Office on a near-constant loop. I am so excited to begin the next chapter of our life together in New Mexico.

ACKNOWLEDGMENTS

First of all, a huge thank you to my advisor, Patrick Young, for your unwavering confidence in my abilities (even if a month would pass where I could not seem to get anything done). I will always appreciate your patience, understanding, and guidance in helping me to become a successful independent researcher, and for pushing me to take on more than I would have thought to do myself. Your advice and encouragement over the last five years have been invaluable to me.

Thanks to my committee members, past and present: Ariel Anbar, for taking on an astrophysics student to work on a geochemistry project; Phil Christensen, for being the fifth member of my exam committee and asking thoughtful questions; Steve Desch, for allowing me to get involved with the astrobiology-related initiatives and collaborations at ASU, for writing recommendation letters, and for helping to send me to every conference I've asked to attend – so much of my graduate school experience has been shaped by those opportunities; Hillary Hartnett, for taking time to explain unfamiliar chemistry concepts and boosting my confidence during my oral exam preparation; Jenny Patience, for your recommendations during the horrifying process that was applying for post-doc positions; and Evgenya Shkolnik, for your helpful suggestions and advice at my annual meetings.

I also want to thank my family for inspiring me to follow my dreams; I would not be where I am today without your love and support. Thanks to my Mom, Patricia Truitt, for your creativity, for your passion, and your humor; I am so grateful that you are still here to see me achieve this goal. Thanks to Jessica Truitt for listening, for quoting movie lines with me, and for being my sister, oldest friend, and confidant. Thanks to my Dad, Steve Truitt, for supporting me through school, for always working so hard to provide for us, for sending me funny panda videos, for thinking Rick and Morty is awesome, and for teaching me to appreciate a good scenic drive.

Thank you to Fern Truitt for the Words With Friends games, and appreciating my cat pictures. Thank you to Nellie Truitt and (the loving memory of) my grandfather, Robert Truitt, for always being so excited that I was going to become "Dr. Truitt." Thanks to Jon Stricklan for helping to move me out to Arizona, and for offering me a place to stay when I visit Texas. Thanks to Laura George for giving me the opportunity to lead a workshop at the BTNW conference, for showing real interest in my astronomy research, and for helping me find my spirit animal.

To friends who have kept me sane: shout out to Luke Probst for the Marvel movie marathons; to Teresa Ashcraft for game nights and Camp T trips; to Natalie Hinkel for sharing a tiny room with me, for climbing the fence, and for all your insights and advice; to Brent Smith and Duho Kim for great times at Monkey Pants karaoke; to George and Cailin Che for the memorable AZ State Fair excursions. To Amanda Johnson, Nicole Massey, Bianca Longoria, Adrienne Willi, and Katharina Zahn, thank you for being such loyal and amazing friends over the years and for believing in me when I doubted myself. And to Sneezy and Flurry, thanks for being purry cats.

I would like to acknowledge support from the following grants: NASAs Follow the Elements team under cooperative agreement NNH08ZDA002C, and NASA's Nexus for Exoplanet System Science (NExSS) research coordination network sponsored by NASA's Science Mission Directorate. Thanks to the ASU Graduate and Professional Student Association for awarding me travel grants on several occasions. Also, thanks to John Shumway for maintaining this dissertation format and making it available online. Thanks to Chester Harman for stimulating discussion on statistical considerations of habitability; to Anusha Kalyaan for helping to develop our astrobiology outreach activities; to Mike Pagano for providing the information on stellar compositions that I've used throughout my work; and to Jeremy, Jerry, and Suzanne W. Dietrich for advice and assistance in setting up the online stellar track database.

TABLE OF CONTENTS

CHAPTER Page

LIST OF TABLES

LIST OF FIGURES

Figure Page

Figure Page

Figure Page

Figure Page

Figure Page

Chapter 1

OVERTURE

Since the very first discovery of an exoplanet, astronomers have hoped to discover a habitable "Earth-like" planet, and to identify whether that planet may potentially harbor life. Even with improved technology and the ever-accelerating discovery of terrestrial-type planets – of particular note, the recent discovery of seven Earth-size planets around a single star, three of which are located in the habitable zone (Gillon et al., 2017) – we have yet to find a world that is truly Earth's twin. With so many potential planetary candidates, it is more important than ever that we are able to categorically define *how* we search for potentially habitable exoplanets. Specifically, we propose narrowing the search based on the likelihood that the exoplanet is *presently* located in the host star's habitable zone (HZ), which can be estimated from the measured surface properties of the star. However, if the end goal is the eventual discovery of life, the stellar evolution *and* the associated HZ evolution must both be considered in order to assess the system's habitability throughout time. If we can define boundary conditions for habitability based on certain observable stellar physical parameters, we will be better equipped to assess whether a planet discovered in a star's HZ is a worthwhile candidate for follow-up characterization.

Attempting to define what makes a planetary system "habitable" is a broad and complex task that requires inclusive and interdisciplinary science. My contribution to this massive endeavor has been to create a catalog of stellar evolution tracks that are meant to reflect the variability of real host star candidates, and to model how these stars influence the habitability environment of their associated planetary systems. My goal has been to understand how information from stellar evolution models can

be used to identify the best candidates for host stars of habitable exoplanets. This is somewhat complicated by two factors: (1) because stars evolve over time, the HZ is a constantly-changing entity; and (2) chemical abundances within stars are measurably different, so two stars of identical mass may have divergent evolutionary paths depending on variations in specific elemental composition. Though stellar evolution is not the only component to consider when working to understand planetary habitability, it is nonetheless one of the most important and physically well-understood factors. The host star plays a literal central role in creating a habitable environment by providing energy to orbiting planets.

In this work, I have defined a continuously habitable zone (CHZ), for the star's entire main sequence (MS) lifetime, as well as for the range of distances that would be continuously habitable for at least 2 Gyr at some point within the MS evolution; it is important to impose this constraint, though I will discuss why it is not necessarily a sufficient criterion for determining long-term habitability (especially for M-stars, which can live longer than several Hubble times). I have made the entire catalog presented in this work available as an online database [1] , with an included interactive interpolation tool; it is designed for use by the astrobiology and exoplanet communities to characterize the evolution of stars and HZs for any real planetary candidates of interest. Especially with the recent release of Gaia data, the catalog of stellar evolution models and the corresponding HZ predictions are even more relevant: Gaia's high precision distance measurements will allow for a more accurate determination of luminosities, the largest source of error in stellar age (e.g. Lebreton et al. (1995)).

For my dissertation, I have investigated how stars of different mass and composition evolve and how the stellar evolution impacts the location of the HZ around a star.

[1] bahamut.sese.asu.edu/~payoung/AST_522/Evolutionary_Tracks_Database.html

The HZ location is determined (on the astrophysical side) primarily by the host star's luminosity and secondarily by its spectral characteristics. The initial mass of a star is the most important factor in determining its lifetime, since a more massive star will more quickly use up its hydrogen fuel on the main sequence (MS), demonstrated by

$$\frac{t_{MS}}{t_{\odot}} \sim \left(\frac{M_*}{M_{\odot}}\right)^{-2.5} \tag{1.1}$$

where $t_{\odot}$ is $\sim$10 Gyr, $M_{\odot}$ is solar mass, and M_* is the mass of the star.

However, to fully understand the variation that can exist in stellar lifetimes, it is also important to consider the specific chemical composition of stars. Heavy elements present in the stellar interior produce fundamental differences in the overall opacity that translate to measurable surface properties. The metallicity (Z) in a star (i.e. elements heavier than hydrogen and helium) primarily affects the amount of bound-free absorption in the stellar interior. A low opacity star would have much more efficient energy escape, resulting in a reduced outward pressure; this would require the energy production (i.e. luminosity) to increase in order to maintain hydrostatic equilibrium and prevent collapse. Thus, based on the initial mass and composition, we see changes in physical surface properties over the course of MS evolution; we calculate both L and T_{eff}, as they are the most important values to parameterize the calculation of HZ limits (e.g. Forget & Pierrehumbert (1997); Jones et al. (2006)).

In chapter 2, I present my first published paper in its entirety, Truitt et al. (2015). I examine how three stellar parameters of interest (mass, metallicity, and the specific oxygen abundance) impact the stellar evolution and may influence the long term habitability of planetary systems. I present a grid of stellar evolution models for Sun-like stars, with masses of 0.5-1.2 $M_{\odot}$, metallicities of Z = 0.1-1.5 $Z_{\odot}$, and a spread in oxygen values ranging from O/Fe = 0.44-2.28 $O/Fe_{\odot}$. When calculating the time-dependent inner and outer HZ radii for each stellar evolutionary track, I

use a widely cited set of prescriptions (Kopparapu et al., 2014), though CHAD (my code for Calculating HAbitable Distances) can be readily upgraded for use with any particular set of HZ limit equations. I discuss why the detailed chemical characterization of exoplanet host stars and a consideration of their evolutionary history are both necessary to assess the likelihood that a planet found in the instantaneous HZ has had sufficient time to develop a biosphere capable of producing detectable biosignatures.

In chapter 3, I present my second published paper, Truitt & Young (2017), wherein I explore the results and implications of an expanded grid of models. In this paper, I have further investigated the effects of variations to the elemental abundance ratios in stars. Specifically, I now consider carbon and magnesium (C/Fe and Mg/Fe at values of 0.58-1.72 $C/Fe_{\odot}$ and 0.54-1.84 $Mg/Fe_{\odot}$, respectively) since they are important players in the overall stellar evolution (Serenelli, 2016). I also discuss the contributions of neon (and briefly, nitrogen); however, it is difficult to know the extent of variability in these two elements in real stars due to the lack of observational abundance determinations. The discussion of neon and nitrogen is based on speculation that these elements could potentially vary by a factor of two relative to solar abundances (0.5 $Ne/Fe_{\odot}$ would be the depleted value, while 2.0 $Ne/Fe_{\odot}$ is enriched), a similar scale to other elements nearby on the periodic table. Neon is more important than nitrogen to the evolution in terms of providing opacity, which is the main effect of different elemental abundances in stars; therefore, we have neglected an in-depth discussion on nitrogen. In this chapter, I discuss how stars of different mass and composition evolve, and how stellar evolution directly influences the location of the HZ around a star. Since the radial position of the HZ is determined primarily by the host star's luminosity and spectral characteristics (which also serve as boundary conditions for planetary atmosphere calculations), it is extremely important to understand as much as we can about the broad range of potential exoplanet host stars that exist.

In chapter 4, I discuss my most recent work, which has focused on development of the stellar evolution code, TYCHO (Young & Arnett, 2005). I have implemented a minimalist coupled working model (Blackman & Owen, 2016) to estimate stellar activity (particularly the X-ray luminosity and magnetic activity, as well as the mass loss and rotation rate) as a function of age. I would like to perform these calculations on each star in my current catalog; this will further characterize the long-term habitability potential of these stars, and will allow us to assess how stellar activity impacts habitability (e.g. atmospheric loss by the stellar wind). For now, I have only performed tests on solar-type stars, in a small grid of models with different initial rotational velocity values, at different overall scaled metallicity values.

Until this update, TYCHO has not had the ability to calculate coronal temperatures and the resulting X-ray luminosities; it was able to calculate rotation and mass loss during the evolution, but I have provided updated prescriptions for those quantities as well. Additionally, if we can test the robustness of the model's predictive power for low-mass stars, we may also extend our calculations down to include our grid of low mass models as well (which has already required a more comprehensive treatment of complex molecular opacities to create with TYCHO). However, M-stars are quite variable in their activity, even among stars of the same age and spectral type (e.g. Shkolnik & Barman (2014)), so predicting activity levels will likely be difficult. M-stars present other issues for habitability as well, including high levels of stellar activity, high energy particle and X-ray fluxes, and close-in HZs with potential for tidal locking. I will briefly discuss the implications for these scenarios. Even though M-dwarf stars are extremely long-lived, they may not necessarily be the best bet to provide a stable environment for life on a nearby planet.

In chapter 5, I will discuss the most recent additions I have made to the catalog, including a substantial grid of low mass models (which represent compositional

variation for M-dwarf stars specifically, with masses ranging from 0.1-0.45 $M_{\odot}$), as well as a small grid of tracks for late-stage evolution (for masses between 0.8-1.2 $M_{\odot}$, since stars of mass lower than about 0.8 $M_{\odot}$ are sufficiently long-lived that late stages of the evolution can be safely neglected). I have also recently performed a semi-quantitative analysis to further understand the contributions of each specific element of interest to the stellar evolution, and how much each surface parameters change over the stellar lifetime. Along with the typical HR-diagram and HZ vs. time plots, I have attempted to graphically convey the percent (relative to solar values) that each elements contributions to evolution. I go on to discuss a recent statistical analysis for the entire catalog of stellar evolution models and HZ predictions. I compare my grid of theoretical evolutionary tracks with actual observations of stars, compiled in the Hypatia catalog (Hinkel et al., 2014), as well as a subset of Kepler exoplanet host stars (Kane et al., 2016). Since stellar age is one of the largest sources of uncertainty in the stellar parameters, especially for stars near the Zero Age Main Sequence (e.g. Valle et al. (2015)), a statistical consideration of the HZ is significant since it provides a probability distribution planets currently in the CHZ_2, regardless of whether we know the precise stellar age.

Finally, I will introduce the method and motivation behind the interactive "Hands-on Habitable Zones" demonstration that I co-designed and built in the fall of 2015 (see Appendix A). I will describe the procedure undertaken to assemble this activity, what we consider as the most important learning objectives, and I will review the how the basic concepts of the demo tie into the themes of my overall dissertation work.

Chapter 2

A CATALOG OF STELLAR EVOLUTION PROFILES

2.1 Introduction: Truitt et al. (2015)

One of the fundamental reasons for planet searches, and indeed one of the central motivations in the field of astronomy, is the eventual discovery of life on a planet outside our solar system. Though stellar evolution is not the only component to consider when working to understand planetary habitability, it is nonetheless one of the most important and physically well-understood factors. It plays a huge role in creating a "habitable" environment by providing energy to orbiting planets. Current astrophysical research into the habitability of exoplanets focuses mostly on the concept of the classical habitable zone (HZ), the range of distances from the star over which liquid water could exist on a planet's surface (Kasting et al., 1993). The location of the HZ is determined on the stellar side primarily by the host star's luminosity and secondarily by its spectral characteristics. These properties serve as boundary conditions for a planetary atmosphere calculation that predicts a planet's surface temperature, and therefore the possibility for stable liquid water.

Over time, our understanding of the HZ has become more sophisticated as models of planetary atmospheres and their interaction with incoming stellar radiation have advanced. There are several components we must consider in order to accurately gauge the surface conditions of a planet, including: planetary atmospheric composition, cloud cover, and whether certain features (e.g. H_2O absorption bands) could be detected in atmospheric spectra (von Paris et al., 2011); the physics of CO_2 cloud condensation and evaporative water-loss; geophysical exchange with an atmosphere;

planet mass, density, and surface temperature; and assumptions about greenhouse effects (Kasting et al., 1993; Selsis et al., 2007; Kopparapu et al., 2014). For this work we use reasonably conservative estimates for the inner and outer boundaries of the HZ, based on HZ limit equations derived from a radiative-convective, 1D atmospheric code that includes updated models of water absorption in planetary atmospheres, discussed in Kopparapu et al. (2014) (see §2.2.3).

It has become commonplace to announce the discovery of a planet when it is found in the HZ of its host star. A test of instantaneous habitability requires overplotting a planetary orbit on the inner and outer boundaries of the HZ corresponding to observed temperature and luminosity of the star. This is not as straightforward as it would appear, since uncertainties in the stellar luminosity (often from distance uncertainties) can cause the HZ to move more than its entire width (Kane, 2014). Nonetheless, for stars with well-measured parameters we can place a planet within the HZ, and we can estimate the number of planets that should be in the HZ in a statistical sense. The *Kepler* mission was launched in 2009 with an explicit goal of finding an Earth-sized planet orbiting within the HZ, and was very successful in discovering these small terrestrial objects (Borucki et al., 2011; Charpinet et al., 2011; Fressin et al., 2012). Subsequent data analysis has predicted that one in five Sun-like stars (Catanzarite & Shao, 2011; Petigura et al., 2013; Gaidos, 2013) and approximately half of all M-dwarf stars (Borucki et al., 2010; Batalha et al., 2013) are likely to host an Earth-sized planet in the HZ.

For astronomers hoping to find planets with detectable biosignatures, this introduces the novel problem of having *too many* candidates. Directly detecting and obtaining spectra for an Earth-like planet around a Sun-like star is typically difficult and would likely require a large-scale space mission. Such a mission may be able to observe no more than about a hundred stars over its lifetime (e.g. Turnbull et al.

(2012)). As a first step, it would be useful to narrow-down the planetary candidates and associated host stars on the basis of whether a planet is *currently* habitable, which we can estimate directly from the measured properties of the star; however, the current habitability of a planet is not the only important consideration for finding Earth-like worlds. If the ultimate goal is the discovery of life, the evolution of stars *and* the associated HZ must be taken into account as well.

The likelihood for detection of life on a habitable planet ultimately stems from a probability distribution constructed of multiple terms falling into three broad classes: the ability of a planet to sustain a biosphere, the likelihood that biosignatures can persist at detectable levels on the planetary surface, and the technique being used to observe the planet. We can begin defining individual terms for each of these categories, which will be expanded upon as our understanding progresses. As examples of the latter classes, some inhabited planets will probably be unidentifiable until we are able to examine them from up close. An obvious example is Europa in our own solar system, which may support a biota under its icy crust. The limited communication of the potentially life-sustaining region with the surface gives Europa a low potential for detectability because biosignatures will escape at low levels at best and will be rapidly destroyed by Jupiter's radiation environment.

More subtle effects may come into play that could even prevent detection of surface biospheres on terrestrial planets. As examples, planets with a highly reducing bulk chemistry could conceivably fix free oxygen faster than even a substantial population of photosynthesizing organisms could produce it, which could deprive us of an opportunity for detection of life. Free oxygen is often suggested as one of the more "useful" or "indicative" biosignatures, although recently that idea has been called into question; it has become more apparent that oxygen present in a planetary atmosphere may not necessarily indicate any sort of biogenic process (Domagal-Goldman

et al., 2014; Wordsworth & Pierrehumbert, 2014; Luger & Barnes, 2015). Such a planet might, on the other hand, be able to sustain high levels of biogenic methane that could not be attributed to geological processes such as serpentinization. This planet would have a higher likelihood of detection for missions that are able to observe methane as well as oxygen, which is why a thorough characterization of the entire planetary system is important.

One of the first things we should consider in attempting to understand a whether a planet may support life, and the likelihood of detection, must be the characteristics of the host star and the location of the surrounding HZ. We have the soundest basis for developing detection strategies for Earth-like life, and such life is clearly favored by Earth-like conditions. Such conditions are, by definition, most likely to be found in the HZ. However, the instantaneous location of the planet and HZ are too limited to assess this aspect of the planet's habitability. The location of the HZ is a function of time; we know that as stars age, the habitable region will move away from the star due to the gradual increase in stellar luminosity (L). The effective temperature (T_{eff}) will also evolve, changing the spectrum impinging upon the planet's atmosphere. Therefore, any orbiting planets detected around a particular star may only have spent a relatively short time in the HZ. It is easy to assume that a planet around a sedate, five billion year old star will be as rich and diverse as Earth. Time dependent models show, however, that more than half of the orbits that are in the HZ at some point during the evolution are actually only habitable during the latter part of the star's life. Our hypothetical five billion year old planet will not be a very fecund place if it just entered the HZ 100 Myr ago. It is estimated that life only produced a detectable change in Earth's atmospheric chemistry 1 – 2 Gyr after Earth's formation (Kasting, 1993; Brocks et al., 1999; Kopp et al., 2005; Anbar et al., 2007; Crowe et al., 2013) even though Earth was in the Sun's HZ from very early times.

Identifying these kinds of systems from readily measurable stellar and orbital parameters would rapidly reduce the number of habitable planetary candidates. An essential parameter that affects stellar and HZ evolution is the *detailed* chemical composition of a star. The rate of stellar evolution and the change in T_{eff} and L are dependent on the abundances of individual elements, especially oxygen and iron (Young et al., 2012). The sensitivity of stellar evolution to composition arises from two effects: the equation of state (EOS) and the radiation opacity (Rogers et al., 1996; Iglesias & Rogers, 1996). The changes in the EOS are relatively minor, but rearranging the proportions of different species at a constant [Fe/H] can result in significant opacity changes of tens of percent (Iglesias & Rogers, 1996). Opacity changes the rate of leakage of radiation, and increased radiation pressure in the stellar envelope drives expansion, resulting in larger radii and lower effective temperatures. A slower rate of energy loss also requires a slower rate of nuclear burning to maintain hydrostatic equilibrium. So we expect stars with enhanced abundance ratios [X/Fe] to be cooler, less luminous, and longer-lived relative to stars with the same [Fe/H].

Measurements of [Fe/H] alone are insufficient to predict the stellar evolution (Young et al., 2012). In practice, it is usually only the iron abundance that is measured for many stars, and other elements are assumed to scale proportionally to the Sun; this means models of stellar evolution for stars of different metallicity are generally created under this assumption. This is a nearly universal practice in stellar modeling, though the abundance ratios in real stars vary substantially. Except for a uniform enhancement of the α elements (O, Ne, Mg, Si, S, Ar, Ca, Ti) in stars of very low metallicities, variations in abundance ratios at a given [Fe/H] are neglected, despite the fact that stellar evolution is sensitive to specific composition.

For solar mass stars near solar [Fe/H], in all cases, enhanced abundance ratios cause larger changes than depleted ratios. C, Na, and Mg have small but noticeable

effects. C has a high abundance but relatively few electron transitions and a low ionization potential. Mg and Na have lower abundances but higher opacity per gram than C, resulting in a similar degree of shift in the tracks. Si has less impact due to its smaller range of variation, and Al, Ca, and Ti have very small effects due to their small abundances; these can be neglected for the purpose of habitability. The largest changes arise from variation in oxygen (Young et al., 2012). Both L and T_{eff} of the enriched compositions are systematically lower at a given age, but stellar evolution models show the most profound effect is on the pace of the evolution. For example, for a 1 $M_{\odot}$ star with solar [Fe/H] the main sequence (MS) turnoff for a model representing the low end of the distribution of oxygen abundance in nearby stars occurs at an age of $\sim$ 9 Gyr. Solar composition has a turn-off age of $\sim$ 10 Gyr, and an oxygen-rich model turns off at $\sim$ 11 Gyr (and at lower L and T_{eff}).

In this paper, we examine how stellar mass, metallicity, and elemental abundance ratios influence the habitability of planetary systems. We present a grid of stellar evolution models for Sun-like stars, with masses of 0.5 - 1.2 $M_{\odot}$, metallicities of Z = 0.1 - 1.5 $Z_{\odot}$, and a spread in oxygen values ranging from O/Fe = 0.44 - 2.28 $O/Fe_{\odot}$. When calculating the time-dependent HZ radii for each of our stellar evolutionary tracks, we have chosen to use a widely cited and well-known set of prescriptions (Kopparapu et al., 2014), though the utility of our catalog is that our models are easily transferrable for use with any particular set of HZ limit equations; this includes scenarios where a so-called "cold start" is not viable (i.e. a frozen planet enters the HZ late in its evolution, yet does not have the capability to thaw for the sake of habitability). Kopparapu et al. (2014) work under the assumption that a cold start is in fact plausible. Following Kasting et al. (1993) we present a scenario where the outer limit of the HZ at the zero age main sequence (ZAMS) is a hard limit that does not vary with the star's evolution so that these two scenarios can be compared.

We examine F, G, and K-type stars in particular because they are the closest in physical properties to our own Sun, which is a good starting point of comparison if we want to look for potential host stars of habitable Earth-like planets. M-stars present other issues for habitability, including high levels of stellar activity with high energy particle and X-ray fluxes, close-in HZs with potential for tidal locking, spin-orbit resonances and tidal heating, and dynamically packed inner systems. We therefore defer calculations of M-stars, which require more comprehensive treatments of complex molecular opacities, to a separate paper.

Ultimately, we are interested in a star that could host a planet that has remained in a continuously habitable zone (CHZ) for at least 2 Gyr. This is approximately the amount of time it took for life on Earth to change the atmospheric composition sufficiently that there would be a detectable biosignature if viewed from another system, utilizing missions recommended in the most recent Decadal Review of Astronomy and Astrophysics (e.g. transmission spectroscopy with JWST or direct detection with a coronagraph, starshade, or interferometer). We define a CHZ for the star's entire MS lifetime, as well as the range of distances that would be continuously habitable for at least 2 Gyr at *some point* in the star's evolution. We describe our choice of parameter space, stellar evolution code, and assumptions for calculating the HZ in §2.2, our interpretation of the results in §2.3, and our conclusions in §2.4.

2.2 Methodology

2.2.1 Parameter Space and Oxygen Abundance Values

In this work we present a grid of stellar models suitable for the prediction of HZ locations. The most important variable for stellar evolution is, of course, mass. Second is total metallicity, Z. Third is the oxygen abundance ratio, O/Fe. The ratios

C/Fe and Mg/Fe also produce a small effect in stellar evolution and have substantially variable abundance ratios (Neves et al., 2009; Mishenina et al., 2008; Takeda, 2007; Young et al., 2014). In this work, ratios without brackets (e.g. O/Fe) indicate the linear absolute abundance ratio in terms of mass fraction, while a bracketed ratio denotes the log of the atom number relative to the solar abundance value for that same element. The latter is the conventional [O/Fe] given by

$$log_{10}\frac{(O/Fe)}{(O/Fe)_{\odot}} = [O/Fe] \tag{2.1}$$

This work quotes linear ratios relative to solar (2.28 $O/Fe_{\odot}$) since the range of abundance ratios is small enough to not require logarithmic notation. We use mass fraction as this is the conventional usage for stellar evolution calculations.

Element	$[X/H]_{standard}{}^{a}$
C	0.173
O	0.051
Na	0.068
Mg	-0.029
Al	-0.124
Si	0.078
Ca	0.027
Ti	0.072

Table 2.1 Abundance adjustments: solar to average sample composition.

a - Standard composition values relative to solar value (Lodders, 2010)

Here we consider the major contributors, mass, metallicity, and oxygen abundance. Variations in Z alone are made with a fixed abundance pattern that is uniformly scaled. The spread in oxygen values we use reflects actual variations in oxygen

abundances that have been directly observed in nearby stars (Ramírez et al., 2007; Bond et al., 2006, 2008; González Hernández et al., 2010; Hinkel et al., 2014). The values of $O/Fe_{\odot}$ are taken from Young et al. (2014), which analyzes the intrinsic spread (not accounted for by observational error) in elemental abundance ratios [X/Fe] for 5 large surveys. We use the [O/Fe] from the median survey, which is consistent with the values used for the calculations in Young et al. (2012). A solar composition from Lodders (2010) was adjusted to the mean abundance ratios of the median sample for the elements observed, with all other elements being maintained at solar values for standard composition. The adjusted values are listed in Table 2.1. Changes in $O/Fe_{\odot}$ at each metallicity are made by changing the absolute abundance of O while holding all other metal abundances constant. The abundances of H and He are adjusted in compensation to ensure the sum of mass fractions = 1.

Determinations of O abundance are notoriously sensitive to non-LTE effects (Grevesse et al., 2007) and line-blending, which may introduce random unphysical errors in the O abundance measurement that are not accounted for in the quoted observational errors. The surveys considered in Young et al. (2014) were chosen in part for using the most reliable of the optical O lines, but we also examine a smaller range of O variation. Instead of choosing a random value, we use the $u_{intrinsic}$ (Young et al., 2014) for a sample of 40 "solar twins" from Ramírez et al. (2009). Qualifying as solar twins requires observable parameters quantitatively close to the Sun. In order for a star to match the Sun closely in physical observables, it is necessary for it to have a composition close to solar. Using $u_{intrinsic}$ for the solar twin sample thus provides a conservative estimate of [O/Fe] variation.

The initial grid encompasses solar-type stars on the MS, covering a mass range from 0.5 - 1.2 $M_{\odot}$ at increments of 0.1 $M_{\odot}$, corresponding to spectral types M0 - F0 at $Z = Z_{\odot}$. Models are calculated for metallicities of 0.1 - 1.5 $Z_{\odot}$ at increments of 0.1

$Z_\odot$. Two models are calculated with values of $O/Fe_\odot$ at each Z value (end members 2.28 and 0.44 $O/Fe_\odot$). The other two O cases (0.67 and 1.48 $O/Fe_\odot$) were done only at solar Z value. The grid is complete for the MS until hydrogen exhaustion in the core for all cases. Post-MS evolution for short lived stars (> 1 $M_\odot$), cool stars (e.g. M-dwarf stars), and contributions from minor elemental constituents (such as C and Mg) will be explored in the next chapter.

2.2.2 TYCHO

The stars in our catalog were simulated using TYCHO (Young & Arnett, 2005). TYCHO is a 1D stellar evolution code with a hydrodynamic formulation of the stellar evolution equations. It uses OPAL opacities (Iglesias & Rogers, 1996; Alexander & Ferguson, 1994; Rogers & Nayfonov, 2002), a combined OPAL and Timmes equation of state (HELMHOLTZ) (Timmes & Arnett, 1999; Rogers & Nayfonov, 2002), gravitational settling (Thoull et al., 1994), general relativistic gravity, time lapse, curvature, automatic rezoning, and an adaptable nuclear reaction network with a sparse solver. A 177-element network terminating at ^{74}Ge is used throughout the evolution. The network uses the latest REACLIB rates (Rauscher & Thielemann, 2000; Angulo et al., 1999; Iliadis et al., 2001; Wiescher et al., 2006), weak rates from Langanke & Martínez-Pinedo (2000), and screening from Graboske et al. (1973). Neutrino cooling from plasma processes and the Urca process is included. Mass loss is included but is trivial for this mass range; heightened early mass loss seen in some young stars (Wood et al., 2005) is not included. It incorporates a description of turbulent convection (Meakin & Arnett, 2007; Arnett et al., 2009, 2010; Arnett & Meakin, 2011), based on 3D, well-resolved simulations of convection between stable layers, analyzed in detail using a Reynolds decomposition into average and fluctuating quantities. It has no free convective parameters to adjust, unlike in mixing-length theory.

TYCHO outputs information on stellar surface quantities (including L and T_{eff}) for each time-step of a star's evolution, which we then use to calculate the inner and outer radii of the HZ as a function of the star's age. The initial composition of the stellar models were adjusted as described in §2.1, and new OPAL opacity tables were generated for the specific abundances for each O/Fe value to match the composition of the stellar model. TYCHO begins calculation with a fully convective model on the Hayashi track. We limit our discussion of the HZ to the span between the Zero Age Main Sequence (ZAMS) and the Terminal Age Main Sequence (TAMS). For this purpose, the ZAMS is defined as the luminosity minimum coinciding with the beginning of complete hydrogen burning in the core. The TAMS is defined as the time of hydrogen exhaustion in the core ($X_H < 1.0 \times 10^{-6}$). The complete tracks are publicly available online.

2.2.3 Calculating Habitable Zone Extents

TYCHO evolutionary tracks are used to estimate the extent of the HZ at each point in the stellar evolution. For these estimates we follow the prescriptions of Kopparapu et al. (2013, 2014), which follow from Selsis et al. (2007) and Kasting et al. (1993). These prescriptions parameterize the orbital radii of the HZ as a function of L and T_{eff} facilitating translation from the evolutionary tracks that we create with TYCHO to the estimates for HZ distances.

Kopparapu et al. (2014) use radiative-convective planetary atmosphere models with input synthetic stellar spectra produced by the PHOENIX code (Allard & Hauschildt, 1995). The predicted distance from a star for both the inner and outer edges of the HZ is parameterized as a function of stellar effective temperature and luminosity, for several kinds of planetary atmospheres. The boundary calculations do not include other sources of heating such as those from tidal effects (which are small

for these stars) or effects from potentially eccentric planetary orbits. The distance d of the HZ boundary is defined by

$$d = \left(\frac{L/L_{\odot}}{S_{eff}} \right)^{1/2} \tag{2.2}$$

where S_{eff} is an effective flux received by the planet based on the radiative transfer calculations for different initial spectra corresponding to different T_{eff} passing through the planetary atmosphere, given by

$$S_{eff} = S_{eff\odot} + aT_* + bT_*^2 + cT_*^3 + dT_*^4 \tag{2.3}$$

where $T_* = T_{eff}$ - 5780 K, $S_{eff\odot}$ is the effective flux for Earth from the Sun at the solar T_{eff} value, and a, b, c, and d are coefficients to a polynomial fit. Each distinct planetary atmosphere model generates a unique set of coefficients.

Five cases are described in Kopparapu et al. (2013): (1) Recent Venus, (2) Runaway Greenhouse, (3) Moist Greenhouse, (4) Maximum Greenhouse, and (5) Early Mars. However, Kopparapu et al. (2014) replaces the Moist Greenhouse case entirely with the Runaway Greenhouse case, since the differences between the two are minimal. We use the updated values for the coefficients (a, b, c, d) and $S_{eff\odot}$ from Kopparapu et al. (2014).

The four remaining cases represent a significant range of HZ approximations when we consider both the stellar flux incident on the planet due to the planet's distance from the host star, along with several different atmospheric properties that may exist on an Earth-like planet. Though the amount of solar radiation the planet receives is the largest factor in determining HZ distances, the wavelength-dependent radiative transfer and radiative losses from atmospheres with different levels of greenhouse gases, water, and clouds must also be considered. HZ boundaries are undoubtedly strongly influenced by the presence of clouds in a planet atmosphere. We would expect

H_2O clouds to move the inner HZ boundary inward (Kasting, 1988; Selsis et al., 2007; Yang et al., 2013) because their contribution to a planet's albedo generally outweighs the contribution to the greenhouse effect. Conversely, CO_2 ice clouds are expected to cause warming in a dense CO_2 atmosphere because they reflect thermal radiation back to the planet's surface more efficiently than they reflect incoming radiation back to space (Forget & Pierrehumbert, 1997).

The Runaway Greenhouse (RGH) and Maximum Greenhouse (MaxGH) cases represent the conservative estimates for the inner and outer radii of the HZ, respectively. The RGH limit is the distance at which a planet's oceans would evaporate entirely. The inner edge of the HZ is determined by the level of water saturation in the planet's atmosphere (a warm environment causes evaporation of H_2O from the planet's surface) and the subsequent rapid loss of hydrogen to space due to heating effects from the proximity of the host star. Conversely, planets that orbit near the outer HZ boundary could develop dense, CO_2-rich atmospheres through outgassing. CO_2 begins to condense out of the atmosphere at a certain distance away from the parent star (due to colder temperatures) which reduces the overall greenhouse effect. CO_2 is also an effective Rayleigh scatterer (2.5 times better than air), and so a dense CO_2 atmosphere is expected to have a high albedo, further offsetting the greenhouse effect (Kasting, 1991). Thus, the conservative outer HZ boundary (MaxGH) is the location where Rayleigh scattering by CO_2 begins to outweigh the greenhouse effect.

Additionally, the Recent Venus (RV) case predicts an inner HZ edge much closer to the star, while the Early Mars (EM) case predicts a more distant outer boundary. These we will refer to as the optimistic cases. The RV case limit from radar observations of Venus by the *Magellan* spacecraft that suggest liquid water has been absent from the surface of Venus for at least 1 Gyr (Solomon & Head, 1991), when the Sun was about 90% as luminous as it is today. This gives a more optimistic empirical

estimate for the inner HZ boundary. Likewise, the (optimistic) Early Mars (EM) outer boundary has been estimated based on the observation that early Mars was warm enough for liquid water to flow on its surface (Pollack et al., 1987; Bibring et al., 2006). Although the issue of a warmer early Mars has raised some debate (Segura et al., 2002, 2008), this gives a good estimate of a more distant outer boundary at which a planet could potentially remain habitable.

The TYCHO evolutionary tracks are used as input to CHAD (Calculating HAbitable Distances), which is a code we developed to calculate the inner and outer HZ boundaries for each of the HZ limits presented in Kopparapu et al. (2014). CHAD is easily upgradable to incorporate improved HZ predictions as they become available in the future. In this paper we will focus on the conservative estimates, but all of the calculations will be made publicly available in machine-readable format along with the evolutionary tracks.

2.3 Discussion of Results

From a stellar point of view, three main factors influence the time evolution of the HZ. These are L and T_{eff}, their rate of change, and the stellar MS lifetime. We confirm that mass and total metallicity influence these factors considerably. Following on Young et al. (2012), the ratio of O/Fe is also significant over the entire range of M and Z. When we consider the evolution of the HZ, it is clear that the instantaneous HZ calculated from observed stellar properties is often not a good indicator of a high likelihood for detection of biosignatures, except for very low mass stars. Detectability ultimately depends on assumptions made about the timescales involved in evolution of life and biogeochemical evolution of biosignatures.

2.3.1 *Stellar Properties and Main Sequence Lifetimes*

TYCHO stellar evolution tracks are used to determine the stellar parameters of interest at each time-step in a star's evolution. The evolution was calculated from the pre-MS to H exhaustion. The pre-MS evolution is rapid, with a similar timescale to planet formation, and can be neglected. This provides us with a MS lifetime and a rate of change for the stellar properties. The Hertzsprung-Russell diagrams (HRD) shown in Figures 2.1 and 2.2 demonstrate the effect of variations in oxygen abundance ratios for each mass in our data set, from 0.5 $M_\odot$ to 0.8 $M_\odot$ in Figure 2.1, and from 0.9 $M_\odot$ to 1.2 $M_\odot$ in Figure 2.2. For both figures, the solid lines represent solar-value for the O/Fe ratio, whereas the dashed lines and dotted lines correspond to depleted and enriched oxygen cases (0.44 $O/Fe_\odot$ and 2.28 $O/Fe_\odot$), respectively. Significant changes are seen when the O abundance ratio varies, even at constant Z. Trends with O/Fe parallel those with the total metallicity; low O/Fe stars are bluer, more luminous, and shorter-lived. Higher O/Fe stars are cooler, less luminous, and longer lived. Thus, the specific O abundance in stars (not just the overall metallicity) plays a significant role in stellar evolution and, consequently, planetary habitability.

Figure 2.3 shows $\log(L/L_\odot)$ vs. time (Gyr) for the compositional end member cases in our library for a 0.5 $M_\odot$ star. Models for 0.1 $Z_\odot$, 1.5 $Z_\odot$, $Z_\odot$, 0.44 $O/Fe_\odot$ and 2.28 $O/Fe_\odot$ (each at $Z = Z_\odot$) are shown. Figures 2.4 and 2.5 show the same for 1 $M_\odot$ and 1.2 $M_\odot$ stars. For all masses we see a significant variation in the MS lifetime, with the lowest metallicity star living just two thirds as long as the highest metallicity model for the 0.5 $M_\odot$ star, and about half as long as the highest metallicity model for the 1 $M_\odot$ star. Of particular importance is the change wrought by varying O/Fe. In this case, an otherwise solar composition star with $O/Fe = 2.28$ $O/Fe_\odot$ actually lives longer than a $Z = 1.5$ $Z_\odot$ star. This illustrates the danger in

only measuring [Fe/H] and assuming that a scaled solar metallicity will accurately predict a star's evolution. For the 0.5 $M_\odot$ star, the high-end cases for O and Z are quite similar in terms of L, however the enriched O case sees a longer MS lifetime by about 6 Gyr. As expected, we see that stars with higher Z (or O/Fe) are less luminous, but considerably longer-lived. Table 2.2 shows MS lifetime estimates for the range encompassed by our catalog, acquired using this method.

A more subtle effect to consider is the rate of change of T_{eff} and L. Low opacity models undergo a larger change in luminosity than do the higher opacity models at the same mass, over a shorter total lifetime. Thus, dL/dt is greater for low metallicity (or O/Fe) models, especially during the second half of a star's MS lifetime. The radial movement of the HZ boundaries is concomitantly faster. At 0.5 $M_\odot$, a 1.5 $Z_\odot$ model increases in $L/L_\odot$ by 0.025 dex, while a 0.1 $Z_\odot$ model is brighter by 0.05 dex at the end of the MS. This translates to the luminosity of the star changing by a factor of 5.4 at 0.1 $Z_\odot$ compared to only 2.9 at 1.5 $Z_\odot$. The absolute change in luminosity is even more sensitive to variations in composition at higher masses, though the percent change is smaller. Tables 2.3 and 2.4 show total change in L in terms of L/L_{ZAMS}, and total change of T_{eff} in units of Kelvin (respectively) from ZAMS to TAMS.

Finally, because of how the slopes of dL/dt (and to a lesser extent dT/dt) change over time, the range of orbits in the HZ at different points in the MS evolution can change substantially. When considering the potential for detectability, we wish to avoid planets that have only recently entered their HZ. Table 2.5 shows the fraction (listed as percentages) of orbital radii which enter the HZ after the midpoint of the MS. It is clear from these results that a third to two thirds of orbits that are in the HZ at some point during the evolution only become habitable in the second half of the star's MS lifetime. This effect is more pronounced at lower mass and depeleted composition.

2.3.2 Location of the Habitable Zone

Figures 2.6 and 2.7 show the HZ from a perspective perpendicular to a hypothetical orbital plane, demonstrating how the HZ can vary between different stars. Figure 2.6 shows a 0.5 $M_{\odot}$ star and a 1.2 $M_{\odot}$ star (end member masses) at the lowest and highest metallicity cases (0.1 $Z_{\odot}$ and 1.5 $Z_{\odot}$, respectively). HZ boundaries are solid for the ZAMS and dashed for the TAMS. The high mass stars exhibit some overlap between the outer edge at ZAMS and the inner edge at TAMS, which might correspond to a "Continuously Habitable Zone" (§2.3.3). The largest overlap is for the 0.1 $Z_{\odot}$ model. Given this HZ prescription, there are no orbits around the low mass stars that remain within the HZ for the entire MS. Figure 2.7 similarly shows the HZ distance evolution from ZAMS to TAMS for the end-member oxygen cases (0.44 and 2.28 $O/Fe_{\odot}$) at solar metallicity value. It is clear that the HZ can change substantially over the MS depending on the host star's detailed chemical composition, and the amount it changes is highly dependent on the initial stellar mass. Tables 2.6 and 2.7 show changes in the location of the HZ radius in ΔAU from ZAMS to TAMS for both the inner boundary (RGH) and the outer boundary (MaxGH), respectively.

Although there is nearly as much variation in the location of the HZ for low and high mass and metallicity, the rate of that change has very different implications for habitability. As demonstrated in Table 2.2, the least massive star's MS lifetime is much longer (ranging from $\sim$ 60 - 99 Gyr) than any reasonable timescale for the development of a detectable biosphere. Most orbits even near the boundaries will remain in the HZ for billions of years. Conversely, a more massive star's entire MS lifetime at low Z is only $\sim$ 2.8 Gyr. A planet that takes $\sim$ 2 Gyr to evolve a detectable biosphere (like Earth) would need to remain in the HZ for nearly the entire MS of the host star. Given the rate of change in the HZ position, few orbits would qualify.

Figure 2.8 shows the inner and outer edges of the HZ for each stellar mass for all compositions at the ZAMS, while Figure 2.9 shows the same information at the TAMS. Higher opacities result in boundaries at lower radii. It is interesting to note that with increasing mass, there seems to be a widening of the overall HZ range, as well as a larger spread in the HZ distances due to compositional variation. Figures 2.8 and 2.9 also show the spread in O variation for five values (0.44, 0.67, 1, 1.48, and 2.28 $O/Fe_{\odot}$) at solar metallicity only. These models are indicated by elongated solid lines. The scaled Z cases and the varied O cases appear to be consistent in that they both show the HZ spreading out with increasing mass. The range in distance of the HZ edges for the oxygen values at $Z_{\odot}$ is smaller than for the entire range of metallicity. This is expected, since the total change in opacity of the stellar material is much larger for a factor of fifteen change in total metallicity than a factor of two change in oxygen abundance. Note that these figures also include the spread in oxygen calculated at *each* metallicity value. The elongated dotted lines represent the end member values for the spread in oxygen abundance (0.44 and 2.28 $O/Fe_{\odot}$) calculated at end member metallicity values (0.1 and 1.5 $Z_{\odot}$). These models extend the range of HZ distance even further than do the models for oxygen abundances at $Z_{\odot}$ alone. The difference in HZ position as a function of composition is larger for higher mass stars because the absolute change in L is larger for higher masses. The position of the outer edge changes more than that of the inner because the behavior of the Maximum Greenhouse scenario is more sensitive to the spectrum of the incoming radiation and therefore T_{eff}.

We produce complete evolutionary tracks for the position of the HZ as a function of time for all models. With an independent age estimate for the star, as well as its mass and its composition, the position of an extrasolar planet can be compared not only to the current HZ, but also its past and future location. Assuming stellar properties are

well measured, the dwell time of an exoplanet in the HZ can be estimated to the level of accuracy of the atmosphere models predicting HZ boundaries. Figure 2.10 shows the location of the inner (solid) and outer (dashed) edges of the HZ as a function of time for three masses (0.5, 1, and 1.2 $M_{\odot}$) and high, standard, and low O/Fe values. The smallest radii correspond to the most enhanced oxygen model.

Again, Table 2.2 provides MS lifetimes for each stellar model of interest. The least massive (0.5 $M_{\odot}$) star has the same pattern of MS lifetimes for each of the three oxygen models that we see with the higher mass stars, though the MS lifetimes are *much* longer for the 0.5 $M_{\odot}$ star. The enriched oxygen model (2.28 $O/Fe_{\odot}$) is estimated to live 99.3 Gyr, while the depleted oxygen model (0.44 $O/Fe_{\odot}$) is estimated to live 83.5 Gyr, making the spread in lifetimes about 15.8 Gyr. Conversely, the highest mass star (1.2 $M_{\odot}$) has the shortest overall MS lifetime for each of the oxygen models, with a spread of only about 1.2 Gyr between the two end-member oxygen cases. However, because the average MS lifetime of the more massive star is shorter, the percent difference in MS lifetime estimates between the end-member oxygen cases is much larger for the 1.2 $M_{\odot}$ star than for the 0.5 $M_{\odot}$ star.

Each of the stellar models represented in Table 2.2 generally have longer lifetimes as Z increases, except for the 0.5 and 0.6 $M_{\odot}$ stars, which show a turnover in MS lifetimes between 1 $Z_{\odot}$ and 1.5 $Z_{\odot}$ (at enriched oxygen). The percent differences between the two values is 4.85% for the 0.5 $M_{\odot}$ star and 1.25% for the 0.6 $M_{\odot}$ star. The reason for the turnover in lifetimes for the lowest mass stars at the highest metallicity/oxygen values is because other effects of high heavy element content become large enough to compete with enhanced opacity. In these cases, the amount of hydrogen in the core is reduced by several percent while the fraction of helium has increased. The increase in He reduces the Thompson scattering opacity of the inner, mostly ionized, region of the star while simultaneously reducing the number of free particles

contributing to pressure support. Coupled with the reduced amount of fuel, the MS lifetime ends up being smaller. At even higher metallicity this trend would extend to higher masses. These factors working in tandem produce the turnover we observe, in that the MS lifetime is actually shorter for the 1.5 $Z_{\odot}$ case than it is for the 1 $Z_{\odot}$ case, both at enriched oxygen.

With more oxygen present in the host star – that is, the host star would have a higher O/Fe ratio than present in the Sun – the HZ will be closer in to the star because the star is less luminous and is at a lower effective temperature, and the stellar lifetime will significantly increase. Likewise, a lower oxygen abundance will produce shorter overall MS lifetimes with HZ distances that are markedly farther away from the host star. The total MS lifetime varies by about 3 Gyr between the end-member oxygen abundances. The rate of change of L and T_{eff} is much faster for a star with a shorter MS lifetime, and therefore the location of the HZ changes much more quickly. The habitable lifetime for a terrestrial planet varies by about 4.5 Gyr. Figure 2.10 also demonstrates that the average lifetime for a solar mass star at solar composition (both metallicity and oxygen value) is about 10 Gyr, as expected.

Figure 2.11 shows a similar trend for the end-member metallicity cases, for the same three masses (0.5, 1, and 1.2 $M_{\odot}$). We find here that Earth would be interior to the HZ at all times for the lowest metallicity value. The variation is somewhat less between the high metallicity case and standard Z value, compared to the high-end oxygen and standard O value; however, they are much larger between the low metallicity case and standard value compared to standard and low oxygen. This is unsurprising, considering that a factor of 2.28 increase in O is large enough to produce an opacity increase of a similar magnitude to an overall 150% uniform scaling of metallicity. Reducing O to 0.44 $O/Fe_{\odot}$ is a much smaller reduction than an overall 90% reduction in all opacity producing elements.

A key consideration is how changing oxygen alone compares to scaling the entire metallicity of a star. For both types of compositional variation, we see the same trends in HZ distance with enhanced or depleted compositions. As overall scaled Z increases, MS lifetime increases while L decreases due to greater opacity within the star, which reduces the rate at which energy can escape. Similarly, as the O abundance increases, MS lifetime increases, L decreases, and the HZ will be located nearer to the host star. This is the same overall effect that metallicity exhibits, and for the same reason – increased stellar opacity. What has not been appreciated before is that at a given [Fe/H] other individual elements can vary enough to significantly affect the stellar evolution. In fact, the higher O case at $Z_{\odot}$ prolongs the MS lifetime a bit more than the high scaled Z case alone.

2.3.3 Continuously Habitable Zones

It is useful to quantify the dwell time of a planet in the HZ as a function of its orbital radius. It is clear that the instantaneous habitability of a planet is an insufficient consideration on its own to determine the likelihood of a planet hosting life, and especially a detectable biosphere; rather, a planet must remain habitable for an appreciable amount of time. The simplest exercise is to find a continuously habitable zone (CHZ), the range of orbital radii that would remain in the HZ for the entire MS. Figure 2.12 shows the CHZ for stars of all masses in our range at solar composition. The CHZ is defined by considering the boundary overlap between ZAMS and TAMS. Low mass stars have no CHZ for the conservative cases. For the optimistic case, we have overlap for the entire mass range, though it is much smaller for low mass stars than for high mass stars. This would seem to indicate that low mass stars would have a low likelihood of detectability, but this is somewhat misleading due to the long MS lifetimes of low mass stars.

This simple version of the CHZ is of limited utility. A more useful measure would be the zone that is continuously habitable for enough time for a surface biosphere to produce a measurable and identifiable change in a planet's atmosphere. On Earth this process took $\sim$ 2 Gyr (Summons et al., 1999; Kasting & Catling, 2003; Holland, 2006). We show results for orbits that remain habitable for at least 2 Gyr (CHZ_2). This assumes that Earth's timescale for biological modification of the atmosphere is representative. This is not meant to suggest that other timescales are impossible, but in selecting down a large pool of candidates there is an advantage in looking for what we know works based on Earth's history. It is important to implement some kind of screening process that allows us to narrow down where any upcoming planet-finding missions should look for potentially habitable planets. It is possible of course that life may exist on non-Earth-like planets that do not fall under our 2 Gyr criteria.

Figure 2.13 shows the CHZ_2 for standard composition. This is determined from the inner edge of the HZ at 2 Gyr after the beginning of the MS and the outer edge 2 Gyr before the TAMS, which represents the location around the star that a planet could remain habitable for at least 2 Gyr. Because of the long lifetimes of low mass stars, there is a higher proportion of the HZ included in the CHZ_2 than for the basic CHZ. Likewise, due to the shorter lifetimes of the more massive stars, it would be statistically less likely to find a planet orbiting this type of star that has been in the CHZ for at least 2 Gyr. We would be less confident that a planet located outside of the CHZ_2 would produce detectable biosignatures than one within the CHZ_2. With the exception of planets orbiting M-stars (because of their extremely long lifetimes), it is a useful exercise to determine the location of the CHZ_2. Table 2.8 shows the fraction of time a planet would spend in the CHZ_2 vs. time it would spend in the HZ over its entire MS lifetime. This information will help to quantify the kinds of stars we should focus on in the continued search for potentially habitable exoplanets.

2.3.4 Cold Starts

In our consideration of the CHZ, we must also address the issue of "cold starts." The previous discussion assumes that as the HZ expands outward due to the effects of stellar evolution, any planets that were initially beyond the boundaries of the HZ could potentially become habitable as soon as the HZ reaches them; indeed, the albedos used in the planetary atmosphere models of Kopparapu et al. (2014) are relatively low, which assumes a planet could become habitable upon entering the HZ. However, it may be unlikely that a completely frozen planet (a "hard snowball") entering the HZ late in the host star's MS lifetime would receive enough energy in the form of stellar radiation to reverse a global glaciation, especially if the planet harbors reflective CO_2 clouds (Caldeira & Kasting, 1992; Kasting et al., 1993).

Figures 2.14, 2.15, and 2.16 offer an alternative scenario to that of Figures 2.10, 2.12, and 2.13, respectively, in which we have assumed a cold start is possible. Here we treat the outer boundary of the HZ at the ZAMS as a hard limit that does not co-evolve with the host star over time, so that only planets in the HZ from the beginning of the MS will be considered habitable; if a planet is able to dwell within the HZ from early times, then a cold start is no longer a problem with which we must necessarily contend. Figure 2.14 shows the evolution of the HZ for the same cases as Figure 2.10, now with cold starts prohibited. Figure 2.15 demonstrates what the CHZ might look like if we fix the outer boundary at the ZAMS value. In this figure, the thin-lined shaded region represents the range of orbits in which a planet would simply be in its host star's HZ from the beginning of the MS, while the thick-lined shaded region represents the range of orbits that would be continuously habitable for the star's entire MS lifetime. Note that for low mass stars there are no continuously habitable orbits, though the long lifetimes of these stars make that less of an issue. In all cases,

the range of orbits that could produce a potentially inhabited planet is restricted compared to the case in which cold starts are allowed.

Similarly, Figure 2.16 shows the CHZ_2 when cold starts are prohibited, where the shaded region is now representative of the range of orbits that would be continuously habitable for at least 2 Gyr (as opposed to the entire MS lifetime), and orbits that also would be in the host star's HZ from the beginning of the MS, which would thus help us rule out any planets that would not enter the HZ until later in the star's MS lifetime. If we attempt to understand a CHZ in this way, we see that the ideal habitable regions do not include the TAMS outer limit, where a planet could potentially start out very cold and only enter the HZ late in its lifetime. Considering the time dependent evolution of the HZ is even more important in this case, since a significant fraction of planets that are observed to be within the nominal HZ now are likely to be cold start cases.

2.4 Conclusions

Given the classical definition of the Habitable Zone, which assumes a surface biosphere that supports liquid water, the properties of the host star are obviously of fundamental importance. However, "habitable" does not automatically mean inhabited, which in turn does not equate with observable biosignatures. Many factors must be considered in calculating the likelihood for detection. The astrophysics should be treated in a more nuanced fashion, and the time evolution of the location of the HZ must also be considered.

Time evolution of the parent star is an important consideration, because the timescale for life to develop to a point where it alters the planetary atmosphere sufficiently for biogenic non-equilibrium species to be detectable may be quite long. On Earth, this process took $\sim$ 2 Gyr. Some attention has been paid to this aspect,

but it is overlooked surprisingly often when announcements are made of planets in the HZ of the associated host star. Additionally, the concept of a CHZ is too simple, since it does not take into account the variable lifetimes of stars. There is no CHZ for a solar composition 0.5 $M_{\odot}$ star (using the conservative HZ boundary estimates), but a set of orbits need only be habitable for a small fraction of the total stellar lifetime (which is on the order of 10^{11} years) to meet the 2 Gyr criterion. We propose a 2 Gyr continuously habitable zone as an aid to estimating the likelihood for detection, which is a necessary, but not completely sufficient, condition. Because of the shape of the luminosity vs. time curve for a star, a third to a half of habitable orbits only become so in the second half of the star's life on the MS. For example, one can certainly imagine planets in these orbits entering the HZ when they are geologically dead, which may be unfavorable to life (see Table 2.8).

In turn, the evolution of a star depends on its elemental composition. This is a basic fact of stellar astrophysics and has been considered in HZ evolution in terms of total metallicity by some groups (e.g. Danchi & Lopez (2013)). However, it is important to distinguish between the metallicity of a star as measured by [Fe/H] and the abundances of individual elements. Metallicity is often used interchangeably with [Fe/H], which expresses the amount of iron alone relative to the Sun's elemental abundance. The standard approach to stellar modeling is typically to scale the metallicity assuming all elements scale in the same proportions found in the Sun, though observations show that this is very often not the case. The HZ distance can be substantially impacted even when only abundance *ratios* are changed. Evaluating habitability via stellar evolution requires models that span a range of variation in abundance ratios, as well as total metallicity. For the same reason, characterizing a system requires measurements of multiple elemental abundances, not just [Fe/H].

We have presented the results of changing O/Fe at levels similar to those seen in nearby stars as well as the total metallicity. Both changes influence the evolution by changing the stellar opacity and therefore have similar effects. For low metallicity or low O/Fe at a given [Fe/H], MS lifetimes are shorter, and the total luminosity change over the MS is larger. This results in a high dL/dt and dT_{eff}/dt, and a correspondingly rapid change in the location of the HZ. What is not widely appreciated is that changes in abundance ratios can have very large effects. For example, variation of O/Fe values from a base solar composition by an amount observed in some planet host candidates can change the stellar lifetime more than increasing the metallicity by 50%. An increase in O increases the total heavy element abundance, but there are two important differences. First, the opacity will be different for different mixes of elements with the same integrated heavy element abundances. Second, as long as model comparisons with individual stars are made based only on the measured [Fe/H], which is the common practice, very large errors may be present.

Since many targets of radial velocity planet searches have high quality spectra that can be used to determine abundances, it should not be difficult to compare to stellar models with more accurate compositions as long as such models exist. We have made the library of stellar evolution models available to the community, along with an interactive interpolation tool. The library will be extended in the future for additional elements and masses, as well as tracks for late-stage evolution.

Composition	0.5 $M_\odot$	0.6 $M_\odot$	0.7 $M_\odot$	0.8 $M_\odot$	0.9 $M_\odot$	1.0 $M_\odot$	1.1 $M_\odot$	1.2 $M_\odot$
0.1 $Z_\odot$, 0.44 $O/Fe_\odot$	60.4	33.6	19.8	12.3	8.0	5.5	3.9	2.8
0.1 $Z_\odot$, $O/Fe_\odot$	64.2	35.9	21.2	13.1	8.6	5.8	4.1	3.0
0.1 $Z_\odot$, 2.28 $O/Fe_\odot$	76.9	43.3	25.6	15.7	10.3	6.9	4.8	3.5
$Z_\odot$, 0.44 $O/Fe_\odot$	83.5	52.8	32.5	20.6	13.5	9.1	6.2	4.5
$Z_\odot$, $O/Fe_\odot$	88.4	57.3	35.8	22.7	14.8	9.9	6.7	4.9
$Z_\odot$, 2.28 $O/Fe_\odot$	99.3	64.4	41.2	26.1	16.9	11.1	7.5	5.7
1.5 $Z_\odot$, 0.44 $O/Fe_\odot$	87.6	57.6	36.5	23.3	15.3	10.3	7.0	5.1
1.5 $Z_\odot$, $O/Fe_\odot$	93.6	60.8	39.0	24.9	16.3	10.9	7.4	5.5
1.5 $Z_\odot$, 2.28 $O/Fe_\odot$	94.6	63.6	41.2	26.2	17.0	11.1	7.9	5.8

Table 2.2 MS lifetimes (Gyr) at standard and end member oxygen values, at solar and end member metallicity values, for all masses.

Composition	0.5 $M_\odot$	0.6 $M_\odot$	0.7 $M_\odot$	0.8 $M_\odot$	0.9 $M_\odot$	1.0 $M_\odot$	1.1 $M_\odot$	1.2 $M_\odot$
0.1 $Z_\odot$, 0.44 $O/Fe_\odot$	5.64	4.62	3.70	2.99	2.48	2.04	1.69	1.43
0.1 $Z_\odot$, $O/Fe_\odot$	5.41	4.41	3.51	2.84	2.35	1.94	1.60	1.37
0.1 $Z_\odot$, 2.28 $O/Fe_\odot$	5.27	4.40	3.50	2.73	2.28	1.87	1.52	1.27
$Z_\odot$, 0.44 $O/Fe_\odot$	3.27	3.21	2.73	2.19	1.79	1.50	1.13	1.00
$Z_\odot$, $O/Fe_\odot$	3.17	3.16	2.76	2.21	1.78	1.46	1.09	1.01
$Z_\odot$, 2.28 $O/Fe_\odot$	3.07	3.00	2.71	2.19	1.74	1.39	1.01	1.02
1.5 $Z_\odot$, 0.44 $O/Fe_\odot$	2.96	2.98	2.64	2.13	1.75	1.47	1.05	0.94
1.5 $Z_\odot$, $O/Fe_\odot$	2.89	2.84	2.57	2.11	1.71	1.41	1.01	0.94
1.5 $Z_\odot$, 2.28 $O/Fe_\odot$	2.81	2.75	2.45	1.99	1.58	1.28	1.05	0.91

Table 2.3 $\Delta(L/L_{ZAMS})$ for each mass and end-member composition.

Composition	0.5 $M_\odot$	0.6 $M_\odot$	0.7 $M_\odot$	0.8 $M_\odot$	0.9 $M_\odot$	1.0 $M_\odot$	1.1 $M_\odot$	1.2 $M_\odot$
0.1 $Z_\odot$, 0.44 O/Fe$_\odot$	719	555	315	136	58	101	217	168
0.1 $Z_\odot$, O/Fe$_\odot$	718	592	344	149	53	29	125	114
0.1 $Z_\odot$, 2.28 O/Fe$_\odot$	652	665	425	171	82	22	-5	41
$Z_\odot$, 0.44 O/Fe$_\odot$	320	502	495	303	118	-15	-137	-243
$Z_\odot$, O/Fe$_\odot$	303	463	511	346	170	30	-100	-215
$Z_\odot$, 2.28 O/Fe$_\odot$	256	349	439	346	202	78	-57	-193
1.5 $Z_\odot$, 0.44 O/Fe$_\odot$	277	417	475	335	170	44	-128	-244
1.5 $Z_\odot$, O/Fe$_\odot$	240	345	430	330	193	76	-74	-198
1.5 $Z_\odot$, 2.28 O/Fe$_\odot$	248	296	344	269	144	50	-126	-237

Table 2.4 ΔT (K) for each mass and end-member composition.

Composition	0.5 $M_\odot$	0.6 $M_\odot$	0.7 $M_\odot$	0.8 $M_\odot$	0.9 $M_\odot$	1.0 $M_\odot$	1.1 $M_\odot$	1.2 $M_\odot$
0.1 $Z_\odot$, 0.44 O/Fe$_\odot$	66.40	62.01	57.41	53.59	49.20	45.29	41.95	38.15
0.1 $Z_\odot$, O/Fe$_\odot$	66.13	61.99	56.57	52.82	48.40	44.36	40.54	37.07
0.1 $Z_\odot$, 2.28 O/Fe$_\odot$	65.88	63.02	55.99	57.98	47.54	43.30	39.59	35.88
$Z_\odot$, 0.44 O/Fe$_\odot$	60.69	60.71	54.54	47.52	43.10	38.27	34.00	33.68
$Z_\odot$, O/Fe$_\odot$	60.16	60.60	55.88	47.58	42.86	37.71	32.91	33.00
$Z_\odot$, 2.28 O/Fe$_\odot$	59.15	63.07	56.88	47.63	42.19	36.46	30.53	33.02
1.5 $Z_\odot$, 0.44 O/Fe$_\odot$	58.35	59.04	54.38	46.52	41.81	36.90	32.52	32.51
1.5 $Z_\odot$, O/Fe$_\odot$	57.63	58.53	54.71	46.58	41.57	36.28	31.45	31.79
1.5 $Z_\odot$, 2.28 O/Fe$_\odot$	56.57	57.56	53.67	44.51	39.85	33.99	33.32	32.07

Table 2.5 Fraction (%) of radii which are in the HZ after the midpoint of the MS.

*Note: values in this table have been corrected, and differ from the published version.

Composition	0.5 $M_\odot$	0.6 $M_\odot$	0.7 $M_\odot$	0.8 $M_\odot$	0.9 $M_\odot$	1.0 $M_\odot$	1.1 $M_\odot$	1.2 $M_\odot$
0.1 $Z_\odot$, 0.44 $O/Fe_\odot$	0.39	0.49	0.59	0.69	0.77	0.82	0.83	0.86
0.1 $Z_\odot$, $O/Fe_\odot$	0.37	0.46	0.55	0.63	0.71	0.77	0.79	0.82
0.1 $Z_\odot$, 2.28 $O/Fe_\odot$	0.34	0.42	0.50	0.57	0.65	0.70	0.72	0.73
$Z_\odot$, 0.44 $O/Fe_\odot$	0.23	0.30	0.35	0.40	0.45	0.49	0.50	0.56
$Z_\odot$, $O/Fe_\odot$	0.22	0.28	0.34	0.38	0.42	0.46	0.46	0.54
$Z_\odot$, 2.28 $O/Fe_\odot$	0.20	0.26	0.31	0.36	0.39	0.409	0.403	0.51
1.5 $Z_\odot$, 0.44 $O/Fe_\odot$	0.21	0.27	0.32	0.37	0.41	0.45	0.44	0.50
1.5 $Z_\odot$, $O/Fe_\odot$	0.19	0.25	0.31	0.35	0.38	0.41	0.41	0.48
1.5 $Z_\odot$, 2.28 $O/Fe_\odot$	0.18	0.24	0.29	0.32	0.35	0.37	0.42	0.46

Table 2.6 ΔAU, each mass and end-member composition at RGH (inner) HZ limit.

Composition	0.5 $M_\odot$	0.6 $M_\odot$	0.7 $M_\odot$	0.8 $M_\odot$	0.9 $M_\odot$	1.0 $M_\odot$	1.1 $M_\odot$	1.2 $M_\odot$
0.1 $Z_\odot$, 0.44 $O/Fe_\odot$	0.68	0.86	1.03	1.20	1.34	1.42	1.47	1.55
0.1 $Z_\odot$, $O/Fe_\odot$	0.65	0.80	0.96	1.11	1.24	1.34	1.37	1.45
0.1 $Z_\odot$, 2.28 $O/Fe_\odot$	0.61	0.74	0.88	1.00	1.13	1.22	1.26	1.28
$Z_\odot$, 0.44 $O/Fe_\odot$	0.42	0.53	0.63	0.71	0.79	0.87	0.88	0.99
$Z_\odot$, $O/Fe_\odot$	0.40	0.51	0.60	0.68	0.74	0.80	0.81	0.95
$Z_\odot$, 2.28 $O/Fe_\odot$	0.37	0.47	0.57	0.63	0.68	0.72	0.71	0.90
1.5 $Z_\odot$, 0.44 $O/Fe_\odot$	0.38	0.49	0.58	0.65	0.72	0.79	0.78	0.89
1.5 $Z_\odot$, $O/Fe_\odot$	0.36	0.46	0.55	0.62	0.68	0.73	0.72	0.85
1.5 $Z_\odot$, 2.28 $O/Fe_\odot$	0.34	0.44	0.52	0.58	0.63	0.67	0.75	0.83

Table 2.7 ΔAU, each mass and end-member composition at MaxGH (outer) limit.

Composition	0.5 $M_\odot$	0.6 $M_\odot$	0.7 $M_\odot$	0.8 $M_\odot$	0.9 $M_\odot$	1.0 $M_\odot$	1.1 $M_\odot$	1.2 $M_\odot$
0.1 $Z_\odot$, 0.44 $O/Fe_\odot$	85.8	81.0	75.2	69.0	61.6	54.3	0.0[a]	0.0
0.1 $Z_\odot$, $O/Fe_\odot$	86.8	82.6	77.5	71.5	64.6	57.3	50.0	0.0
0.1 $Z_\odot$, 2.28 $O/Fe_\odot$	88.7	85.1	81.0	75.9	69.7	63.0	55.8	0.0
$Z_\odot$, 0.44 $O/Fe_\odot$	91.5	89.2	86.2	82.6	78.2	73.0	67.4	59.5
$Z_\odot$, $O/Fe_\odot$	91.8	89.9	87.2	83.9	79.9	75.3	70.7	62.2
$Z_\odot$, 2.28 $O/Fe_\odot$	92.7	90.9	88.8	86.0	82.5	78.2	74.4	65.2
1.5 $Z_\odot$, 0.44 $O/Fe_\odot$	92.0	90.0	87.6	84.5	80.3	75.5	71.2	63.4
1.5 $Z_\odot$, $O/Fe_\odot$	92.7	90.8	88.5	85.6	81.8	77.0	73.1	65.1
1.5 $Z_\odot$, 2.28 $O/Fe_\odot$	92.8	91.3	89.4	86.8	83.3	78.7	70.6	65.7

Table 2.8 Fraction (%) of time spent in CHZ_2 vs. the entire MS Lifetime.

a - No orbits are continually habitable for 2 Gyr as a result of the short MS lifetime.

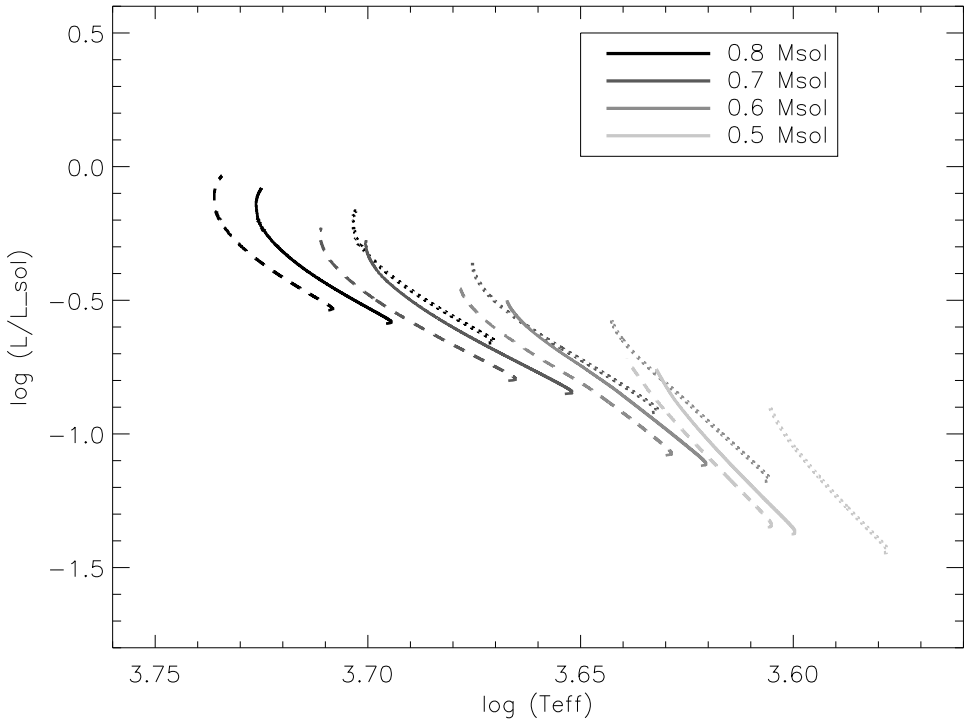

Figure 2.1 HRD, Evolutionary tracks from ZAMS to TAMS for 4 masses, with 0.44 $O/Fe_{\odot}$ (dashed), 1.0 $O/Fe_{\odot}$ (solid), and 2.28 $O/Fe_{\odot}$ (dotted) all at $Z_{\odot}$. The rightward-most dotted line is for the 0.5 $M_{\odot}$ star with enriched oxygen, while the leftward-most dashed line is for the 0.8 $M_{\odot}$ star with depleted oxygen.

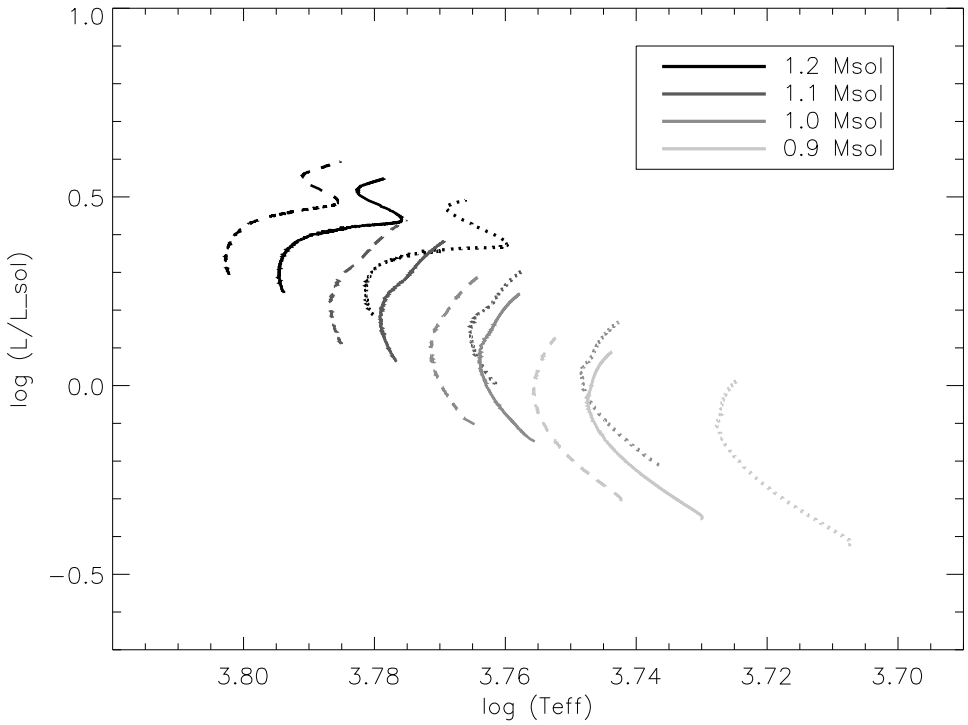

Figure 2.2 HRD, Evolutionary tracks from ZAMS to TAMS for 4 masses, with 0.44 $O/Fe_{\odot}$ (dashed), 1.0 $O/Fe_{\odot}$ (solid), and 2.28 $O/Fe_{\odot}$ (dotted) all at $Z_{\odot}$. The rightward-most dotted line is for the 0.9 $M_{\odot}$ star with enriched oxygen, while the leftward-most dashed line is for the 1.2 $M_{\odot}$ star with depleted oxygen.

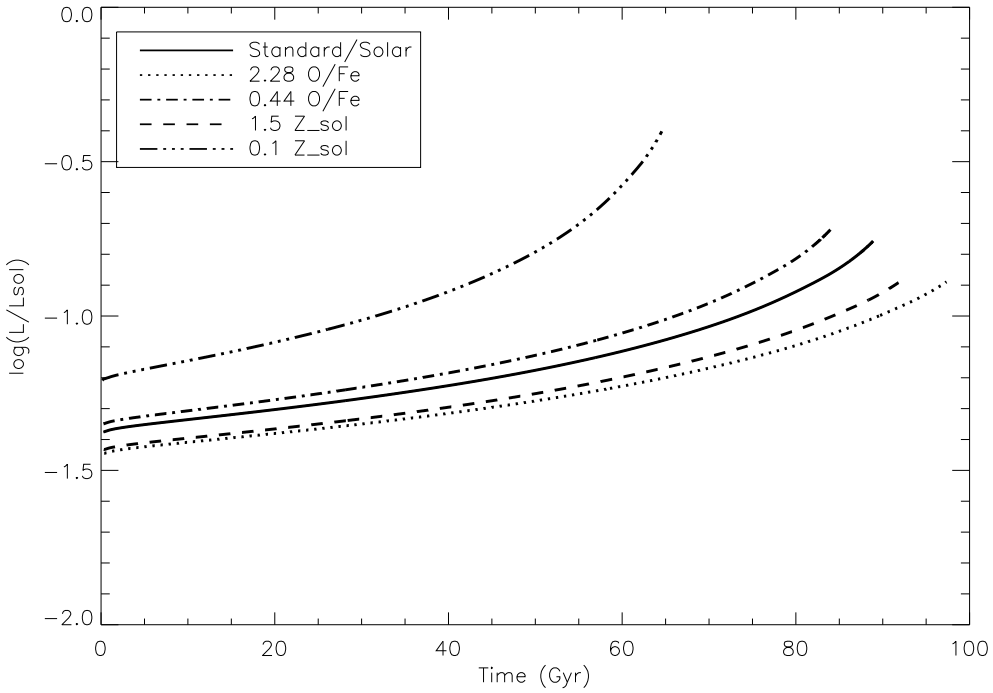

Figure 2.3 Log($L/L_{\odot}$) vs. time (Gyr) for a 0.5 $M_{\odot}$ star at five different compositions. The total MS lifetime varies from 65 Gyr to nearly 100 Gyr. The shortest lifetime corresponds to a star with total Z = 0.1 $Z_{\odot}$. The longest lifetime corresponds not to the highest scaled Z model, but rather to the model with 2.28 O/$Fe_{\odot}$ (at $Z_{\odot}$).

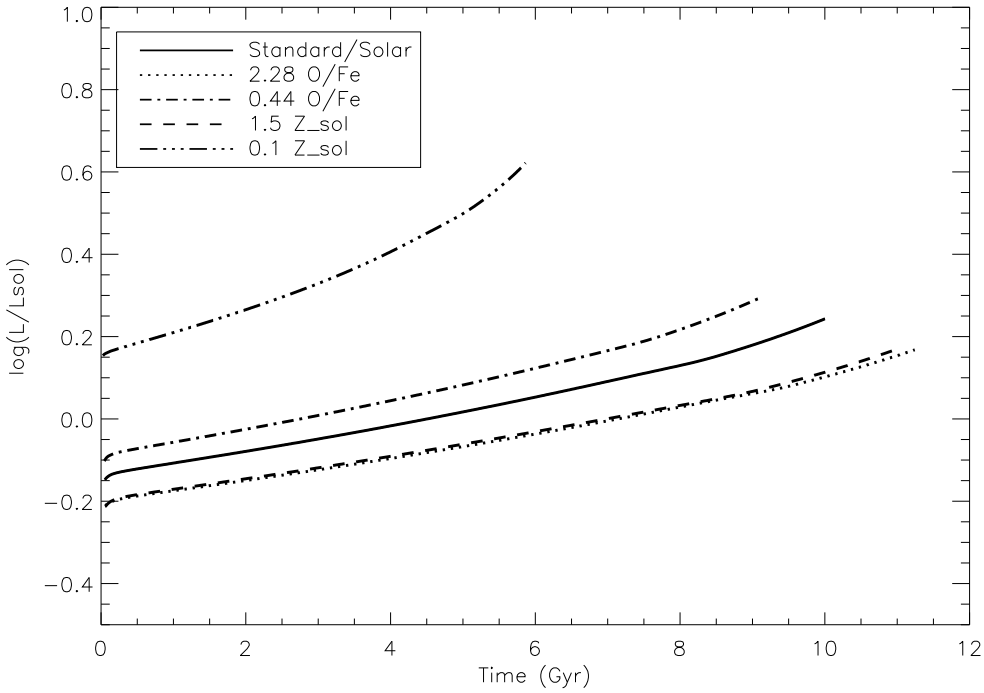

Figure 2.4 Log($L/L_{\odot}$) vs. time (Gyr) for a 1 $M_{\odot}$ star at five different compositions. The total MS lifetime has a much smaller variation, from $\sim$ 6 - 11.5 Gyr. The shortest lifetime corresponds to a star with metallicity of 0.1 $Z_{\odot}$, and the longest lifetime corresponds to the model with 2.28 O/$Fe_{\odot}$ (at $Z_{\odot}$).

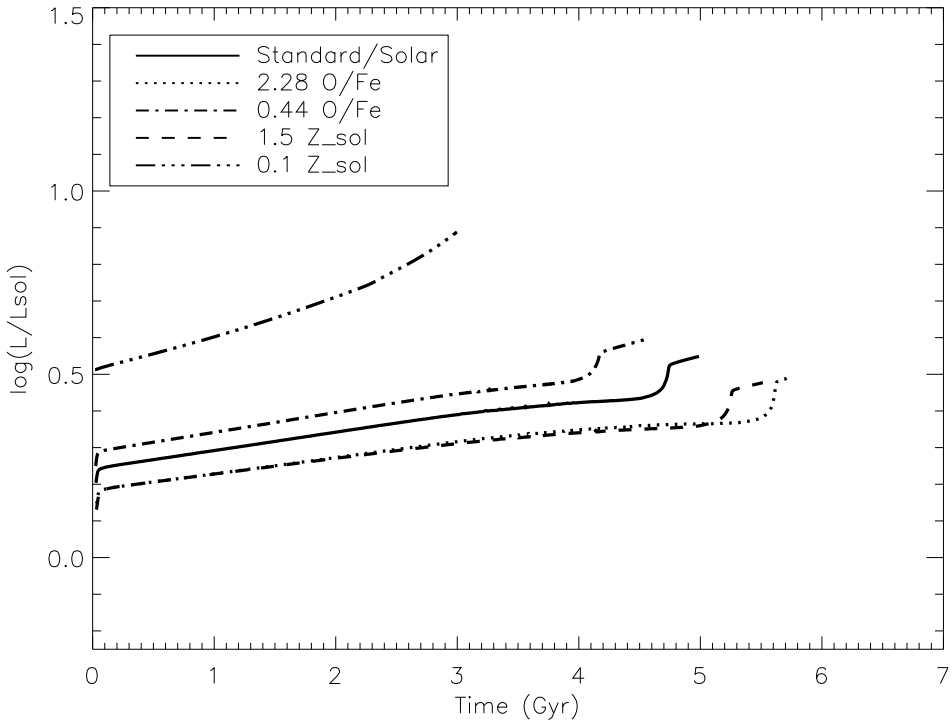

Figure 2.5 Log($L/L_{\odot}$) vs. time (Gyr) for a 1.2 $M_{\odot}$ star at five different compositions. Again, the shortest lifetime corresponds to a star with metallicity of 0.1 $Z_{\odot}$, and the longest lifetime corresponds to the model with 2.28 $O/Fe_{\odot}$ (at $Z_{\odot}$).

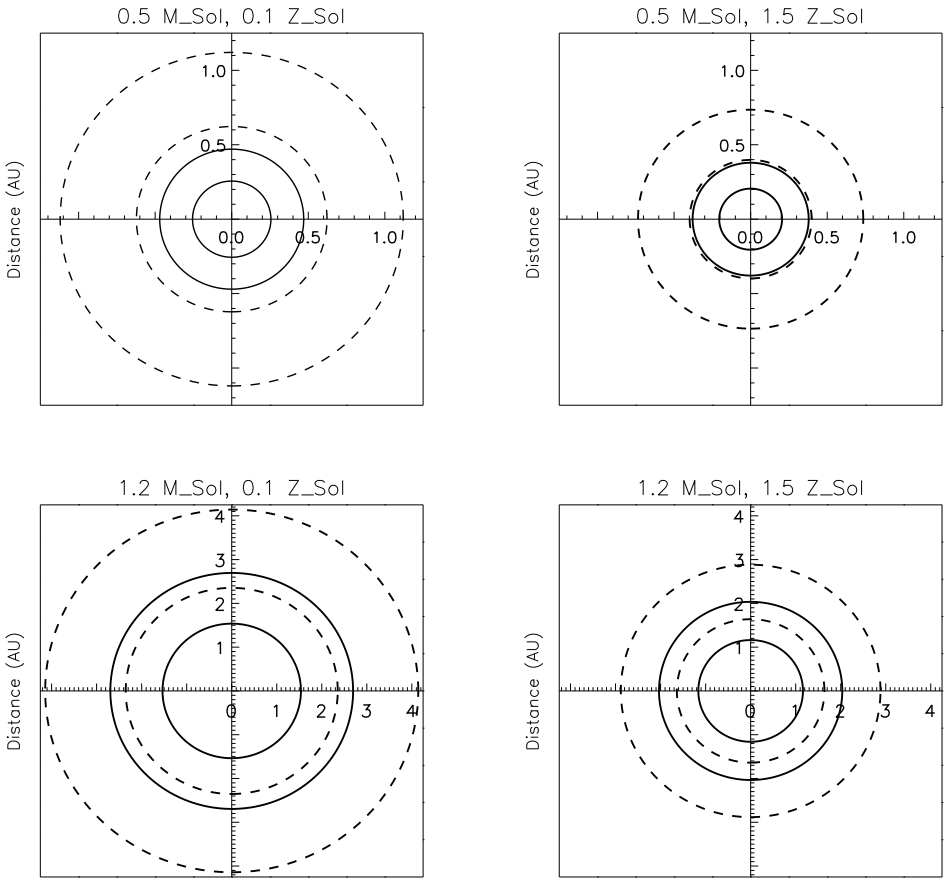

Figure 2.6 HZ Ranges: 0.5 $M_\odot$ (top), 1.2 $M_\odot$ (bottom), for 0.1 $Z_\odot$ (left), 1.5 $Z_\odot$ (right). Shown at ZAMS (solid) and TAMS (dashed). For the conservative HZ limits, inner boundaries are represented by the Runaway Greenhouse case, and outer boundaries are represented by the Maximum Greenhouse case.

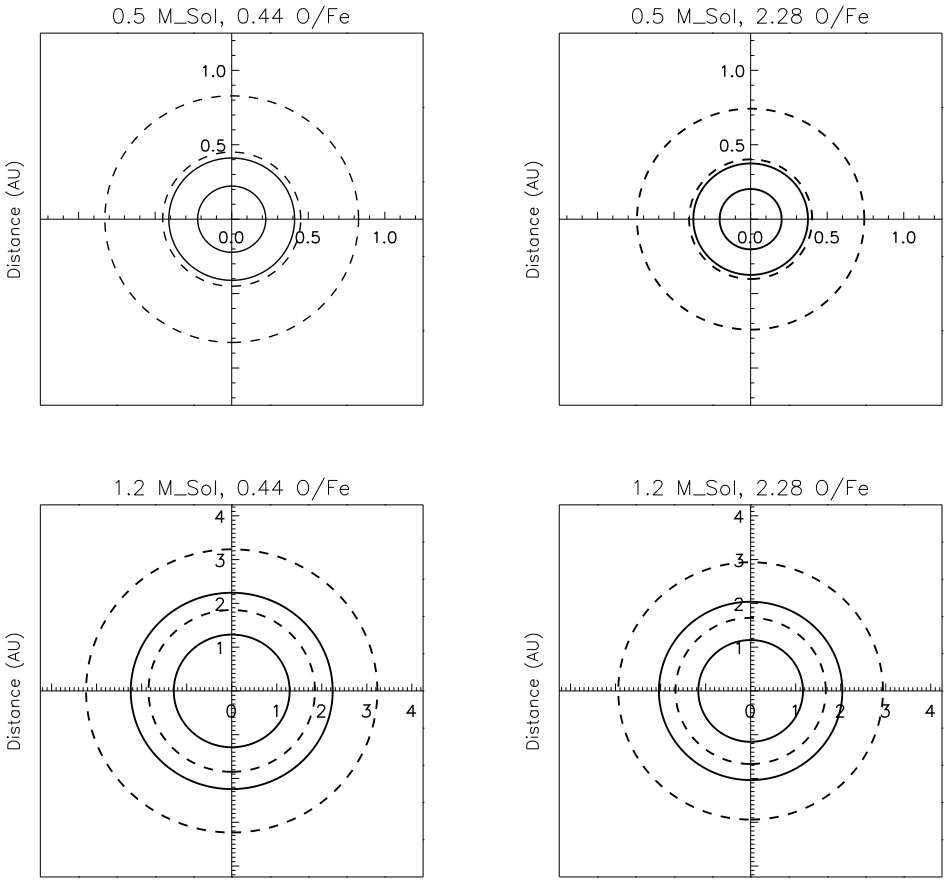

Figure 2.7 HZ Ranges: 0.5 $M_\odot$ (top), 1.2 $M_\odot$ (bottom), for 0.44 $O/Fe_\odot$ (left), 2.28 $O/Fe_\odot$ (right), at $Z_\odot$. HZ shown at ZAMS (solid) and TAMS (dashed). For the conservative HZ limits, inner boundaries represent the Runaway Greenhouse case and outer boundaries represent the Maximum Greenhouse case.

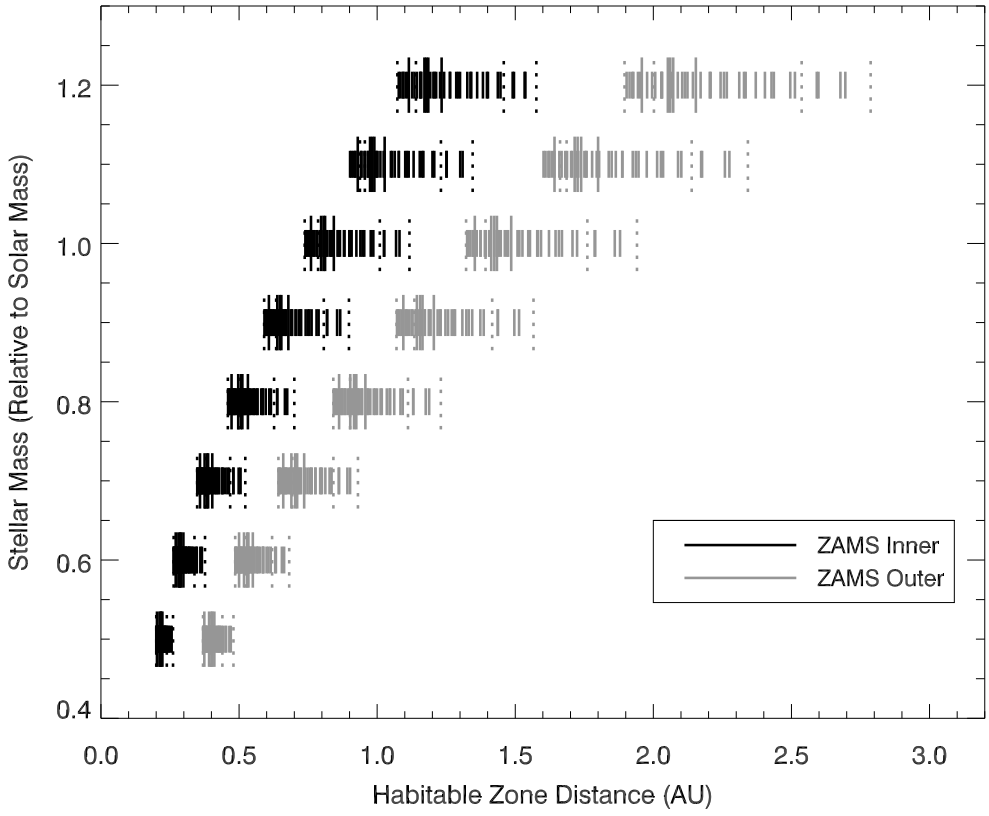

Figure 2.8 Inner and outer HZ edges (RGH and MaxGH) for all masses and compositions at ZAMS. Elongated solid lines represent the 5 oxygen cases at $Z_{\odot}$ for each mass: 2 enriched models (1.48 and 2.28 $O/Fe_{\odot}$), 2 depleted models (0.67 and 0.44 $O/Fe_{\odot}$), and 1 model representing standard (solar O/Fe). The elongated dotted lines represent end-member values for oxygen (0.44 and 2.28 $O/Fe_{\odot}$) calculated at end member Z-values. From left to right are high to low opacity models. Compositional variation has a larger effect for the outer HZ limit, and for higher mass stars.

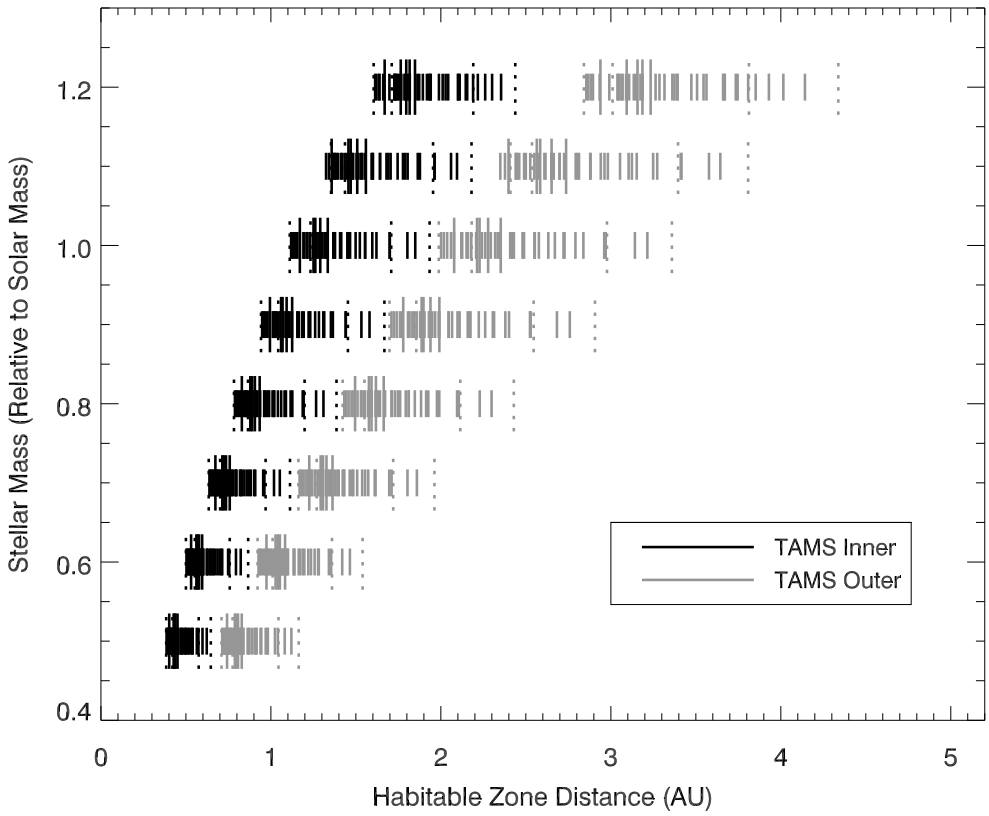

Figure 2.9 Inner and outer HZ edges (RGH and MaxGH) for all masses and compositions at TAMS. Elongated solid lines represent the 5 oxygen cases at $Z_{\odot}$ for each mass: 2 enriched models (1.48 and 2.28 $O/Fe_{\odot}$), 2 depleted models (0.67 and 0.44 $O/Fe_{\odot}$), and 1 model representing standard (solar O/Fe). The elongated dotted lines represent end member values for oxygen (0.44 and 2.28 $O/Fe_{\odot}$) calculated at end-member Z-values. From left to right are high to low opacity models. There is a more exaggerated spreading trend for low mass stars at TAMS than at ZAMS.

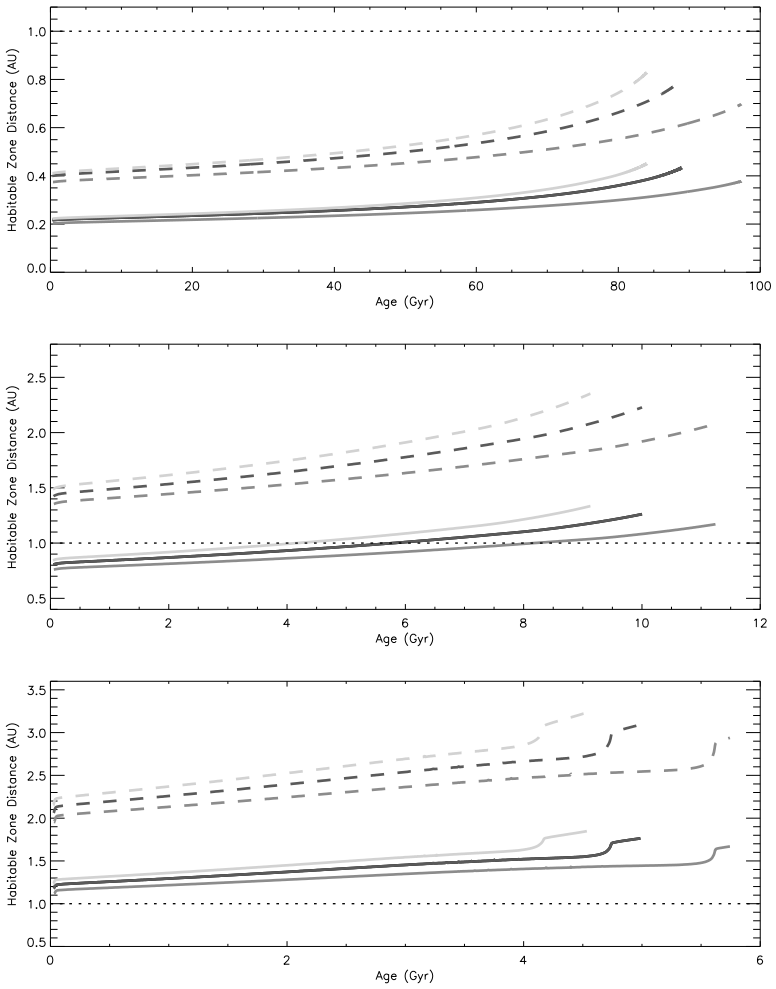

Figure 2.10 Inner (solid) and outer (dashed) edges of the HZ for three values of O/Fe (at $Z_{\odot}$) for three masses: 0.5 $M_{\odot}$ (top), 1 $M_{\odot}$ (center), and 1.2 $M_{\odot}$ (bottom). Each color represents a different $O/Fe_{\odot}$ value: black is solar O/Fe, light gray is 0.44 $O/Fe_{\odot}$, and dark gray is 2.28 $O/Fe_{\odot}$. A 1 AU orbit is indicated by the dotted line. O abundance variations within a star can impact MS lifetime and HZ distance. The inner radius is for Runaway Greenhouse; the outer edge is for Maximum Greenhouse.

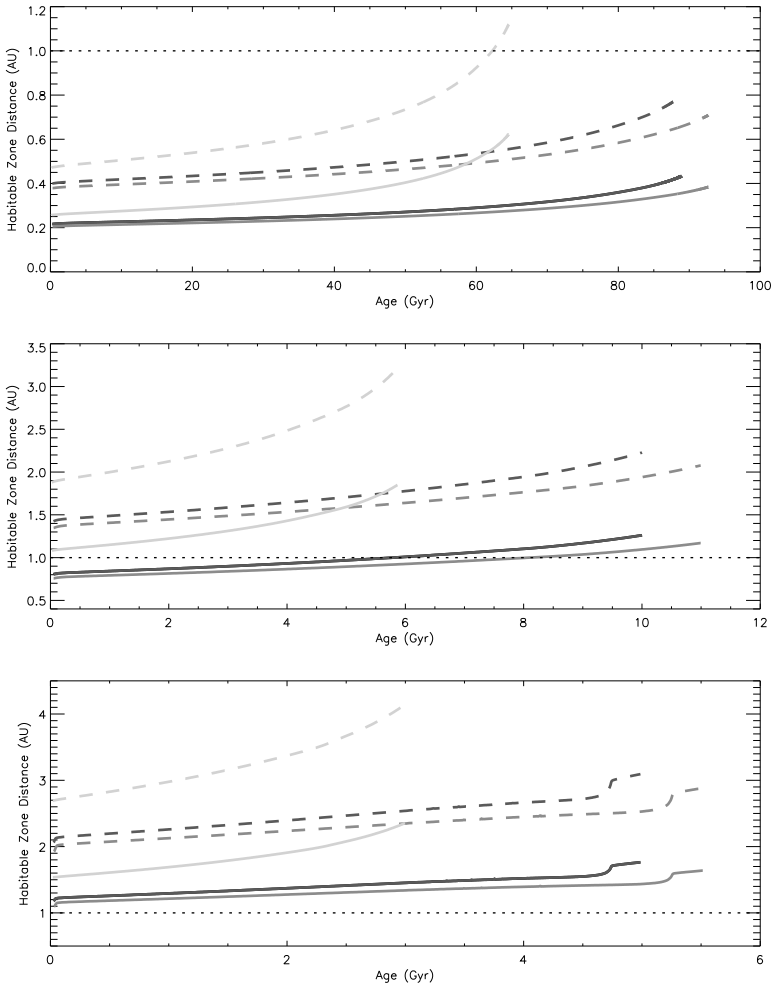

Figure 2.11 Inner (solid) and outer (dashed) edges of the HZ at three Z values for three masses: 0.5 $M_{\odot}$ (top), 1 $M_{\odot}$ (center), and 1.2 $M_{\odot}$ (bottom). Each color represents a different Z value: black is $Z_{\odot}$, light gray is 0.1 $Z_{\odot}$, and dark gray is 1.5 $Z_{\odot}$. A 1 AU orbit is indicated by the dotted line. Metallicity variations within a star can impace MS lifetime and HZ distance. The largest effect is seen at 0.1 $Z_{\odot}$.

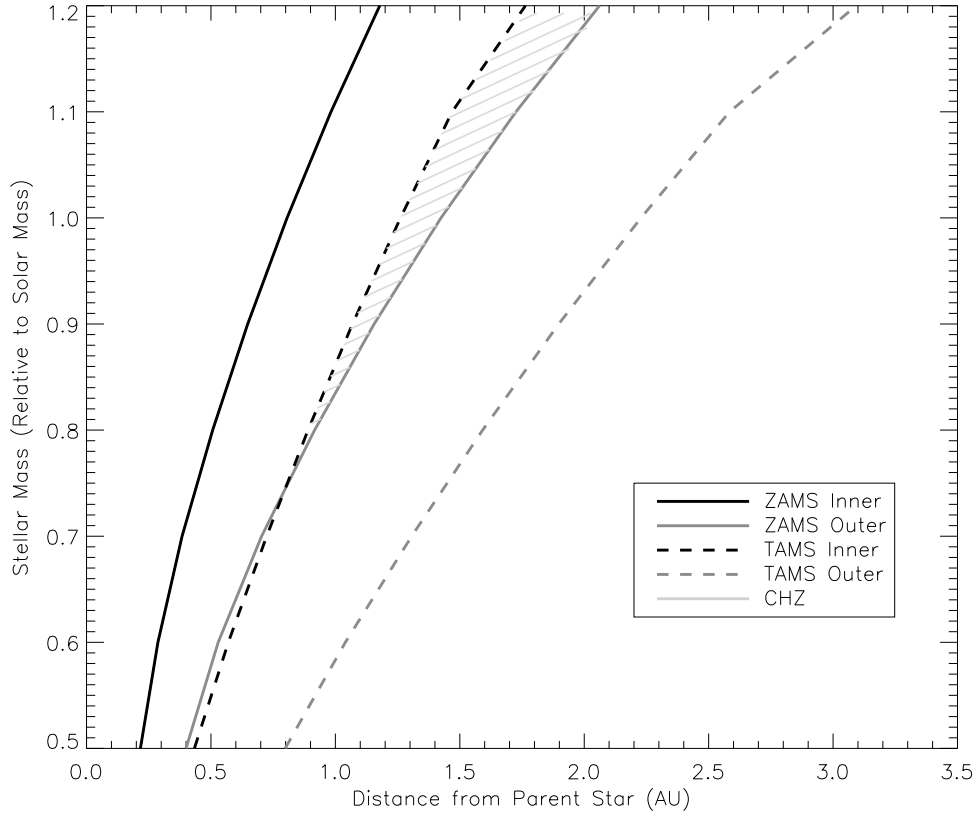

Figure 2.12 Inner (black) and outer (dark gray) boundaries of the HZ at ZAMS (solid) and TAMS (dashed). The light gray shaded region is the CHZ, where an orbit would remain in the HZ for a star's entire MS lifetime. This is for solar-composition stars for each mass. For conservative limits (RGH, MaxGH), low mass stars have no CHZ.

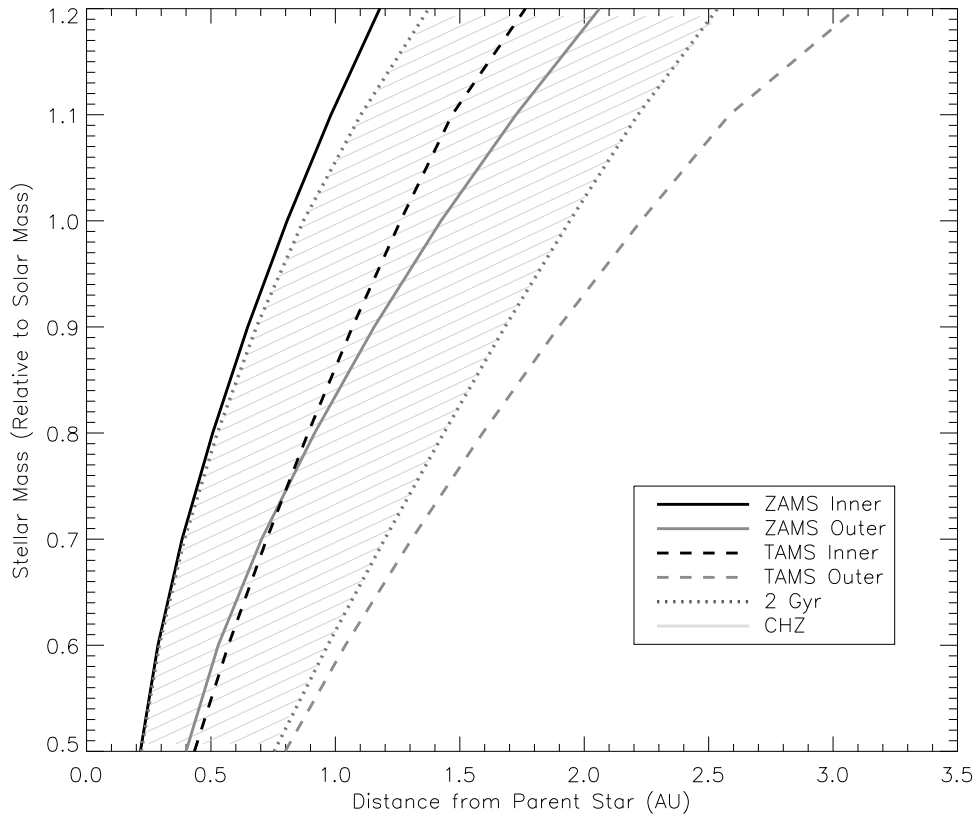

Figure 2.13 Inner (black) and outer (dark gray) boundaries of the HZ at ZAMS (solid) and TAMS (dashed). The inner edge 2 Gyr after ZAMS and the outer edge 2 Gyr before TAMS are indicated by dotted lines. The light gray shaded region is the CHZ_2, in which an orbiting planet would remain in the HZ for at least 2 Gyr. This is for solar-composition stars for each mass. The fraction of the total habitable orbits in the CHZ_2 is higher for long-lived, low mass stars.

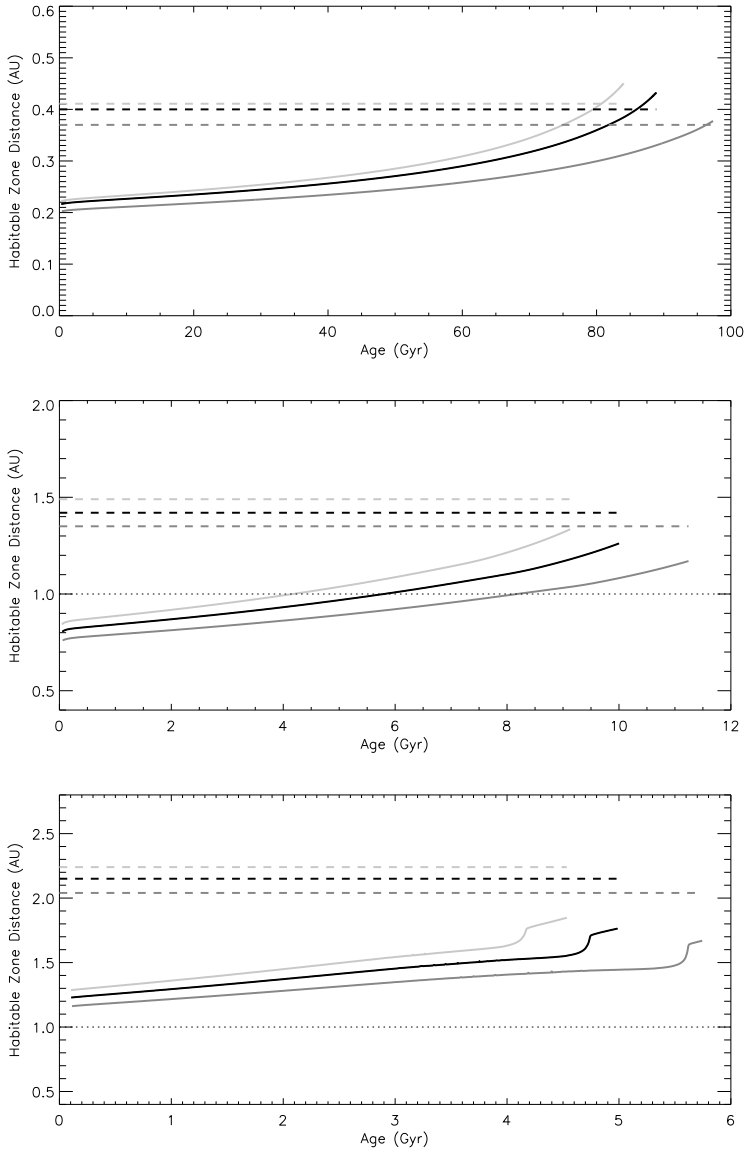

Figure 2.14 Inner (solid) and outer (dashed) edges of the HZ with cold starts prohibited for three values of O/Fe (at $Z_{\odot}$) at three masses: 0.5 $M_{\odot}$ (top), 1 $M_{\odot}$ (center), and 1.2 $M_{\odot}$ (bottom). Black is solar, light gray is depleted (0.44 $O/Fe_{\odot}$), dark gray is enriched (2.28 $O/Fe_{\odot}$). 1 AU is indicated by the dotted line. The inner radius is Runaway Greenhouse and the outer edge is the Max. Greenhouse, at ZAMS value.

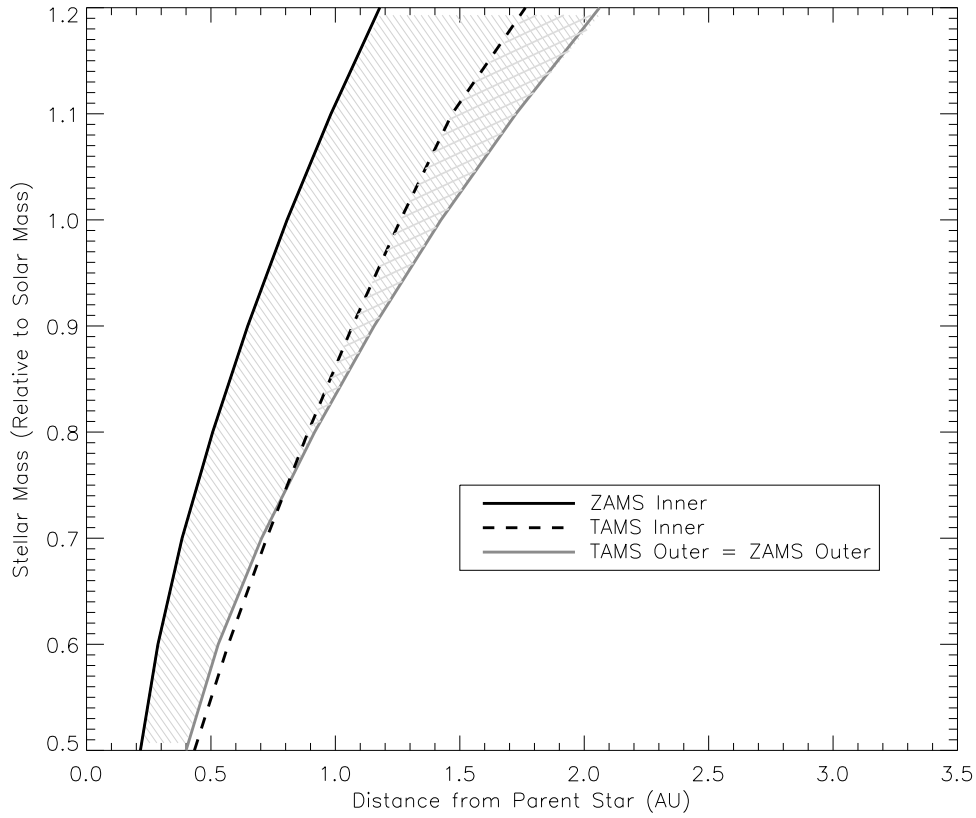

Figure 2.15 Inner (black) and outer (dark gray) boundaries of the HZ at ZAMS (solid) and TAMS (dashed). Here we equate the TAMS outer limit with the ZAMS outer limit in order to address the issue of cold starts. The thin-lined shaded region represents the range of orbits where a planet would be in the HZ at ZAMS, while the thick-lined shaded region represents the range of orbits that would be continuously habitable for the entire MS lifetime (as in Figure 2.12). Approaching the CHZ this way, ideal habitable regions do not include the TAMS outer limit, where a planet might only enter the HZ late in the star's MS lifetime.

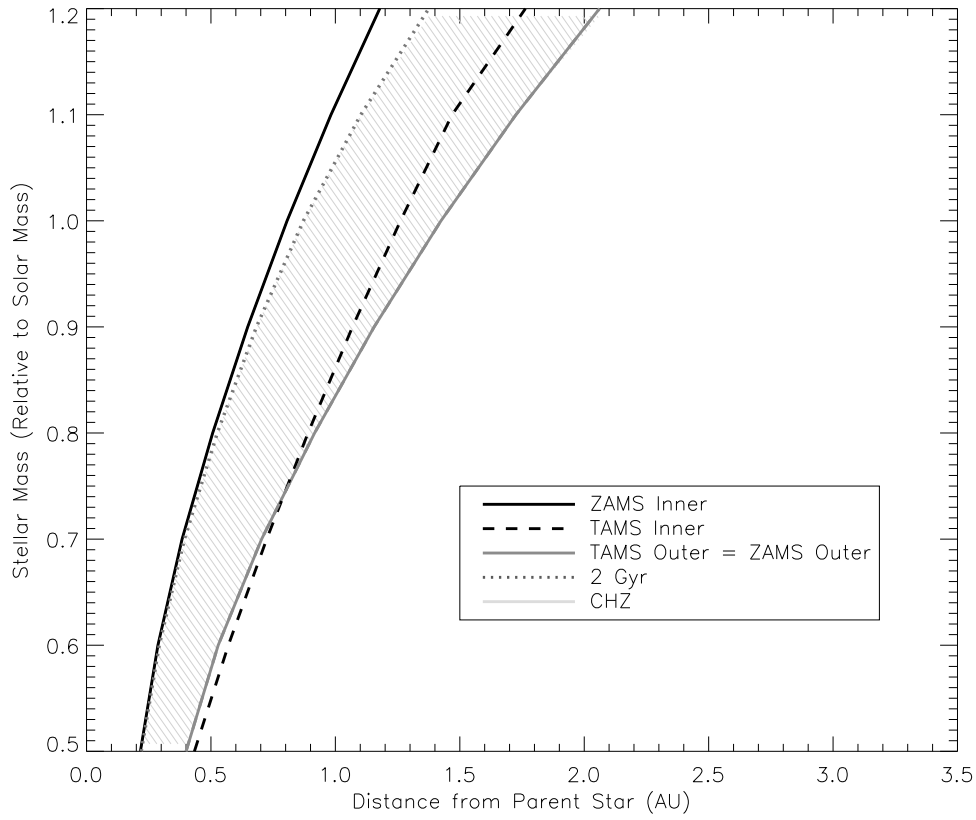

Figure 2.16 Inner (black) and outer (dark gray) boundaries of the HZ at ZAMS (solid) and TAMS (dashed) for solar-composition stars for each mass. This shows the case in which cold starts are prohibited. The TAMS outer limit of the HZ is equated with the ZAMS outer limit. The shaded region represents where a planet would be continuously habitable for at least 2 Gyr and would also be in the HZ at ZAMS.

Chapter 3

EXPANDING THE CATALOG: CARBON, MAGNESIUM, NEON

3.1 Introduction: Truitt & Young (2017)

We are working to understand how stars of different mass and composition evolve, and how stellar evolution directly influences the location of the habitable zone (HZ) around a star. Most of the prevailing research on exoplanet habitability focuses on the notion that the HZ is simply the range of distances from a star over which liquid water could exist on the surface of a terrestrial planet (e.g. Kasting et al. (1993)). Since the radial position of the HZ is determined primarily by the host star's luminosity and spectral characteristics (which also serve as boundary conditions for planetary atmosphere calculations), it is extremely important to understand as much as we can about the broad range of potential exoplanet host stars that exist. Evaluating the potential for liquid water on the surface of a planet requires a deep understanding of the link between stars and the circumstellar environment.

We reiterate the pressing need to thoroughly represent the large variation that exists for potential exoplanet host stars, based both on the specific chemical composition as well as the individual detailed evolutionary history (addressed in our previous paper, Truitt et al. (2015); hereafter T15). Though other groups have done excellent work on the evolution of HZs as a function of a star's overall scaled metallicity (Valle et al., 2014; Oishi & Kamaya, 2016), we argue that it is also important to consider the specific elemental abundance ratios of stars if we want to make any comprehensive assessments about the habitability potential of a particular system. In the current environment, with the almost-constant discovery (e.g. Ziegler et al.

(2017)) and statistical confirmation (e.g. Morton et al. (2016)) of new exoplanets, it is imperative that we as a scientific community have an efficient and consistent way to narrow down the search for potentially habitable exoplanets. If we can define boundary conditions based on certain stellar physical parameters, we will be better equipped to assess whether a planet discovered in a star's HZ is actually a worthwhile candidate to perform follow-up observations for characterization, utilizing the kind of missions recommended in the most recent Decadal Review of Astronomy and Astrophysics: transmission spectroscopy with James Webb Space Telescope (e.g. Barstow & Irwin (2016)), or direct detection with a coronagraph, interferometer, or starshade (e.g. Turnbull et al. (2012)).

Following T15, here we expand our investigation into the effects of variations to the elemental abundance ratios in stars. Specifically, we consider carbon and magnesium, since they are important players in the overall stellar evolution (e.g. Serenelli (2016)). We also discuss the contributions of neon (and briefly, nitrogen); however, we don't know the extent of variability in these two elements in real stars due to the lack of observational abundance determinations. The discussion of Ne and N is based on speculation that these elements could potentially vary by a factor of two relative to solar abundances (i.e. 0.5 Ne/Fe$_\odot$ would be the depleted value, while 2.0 Ne/Fe$_\odot$ is enriched), a similar scale to other elements nearby on the periodic table. Neon is more important than nitrogen to the evolution in providing opacity, the main effect of different elemental abundances. We have made our entire catalog of stellar evolution tracks available as an online database, with an included interactive interpolation tool; it is designed for use by the astrobiology and exoplanet communities to characterize the evolution of stars and HZs for real planetary candidates of interest. In this paper, we describe our choice of parameter space and stellar evolution code in §3.2, our interpretation of the results of the models in §3.3, and our conclusions in §3.4.

3.2 Methodology

3.2.1 Parameter Space & Expanded Model Grid

Here we present an extended grid of stellar models suitable for the prediction of HZ locations. In T15 we discussed the importance of mass, metallicity, and oxygen abundance to the stellar evolution. In this paper, we instead focus on the variation observed in carbon and magnesium abundances, which also produce a measurable effect in the stellar evolution (albeit smaller than the effect observed for variations in the oxygen abundance) and which also exhibit substantially variable abundance ratios in neighboring stars (Neves et al., 2009; Mishenina et al., 2008; Takeda, 2007; Young et al., 2014; Pagano et al., 2015). We also include discussion on the practicality of considering neon's contribution to stellar evolution, though the range of abundance values we quote are not based on observational data.

We again consider the major contributors to stellar evolution: mass, metallicity (Z), and the individual elemental abundance. Variations in Z alone are made with a fixed abundance pattern that is uniformly scaled, while the spread in carbon and magnesium values we use reflects observed variations in abundance ratios in nearby stars (Ramírez et al., 2007; Bond et al., 2006, 2008; González Hernández et al., 2010; Hinkel et al., 2014). One exception is that the range in neon values we use does not result from observed variations in the neon abundances of stars; rather, we vary the neon abundance relative to solar neon to create a range of values that we might reasonably expect to see in stars if we could measure neon more accurately. Changes in $C/Fe_{\odot}$, $Mg/Fe_{\odot}$, and $Ne/Fe_{\odot}$ at each metallicity are made by changing the absolute abundance of each element while holding all other metal abundances constant. The relative abundances of hydrogen and helium are adjusted in compensation to ensure the sum of mass fractions = 1.

Beyond the original grid for oxygen (discussed in T15) that comprised a total of 376 models, we now introduce an additional 240 models for each carbon and magnesium. Also, for the purposes of this work, we've produced a smaller grid of 48 models for neon that includes only end-member cases of interest, resulting in a total addition of 528 new models. The grids for C, Mg, and Ne still encompass stars of mass 0.5 - 1.2 $M_{\odot}$ at each 0.1 $M_{\odot}$ (which includes spectral types from approximately M0 - F0 at solar metallicity), overall scaled metallicity values of 0.1 - 1.5 $Z_{\odot}$ at each 0.1 $Z_{\odot}$, and now abundance values of C, Mg, and Ne ranging from 0.58 - 1.72 C/$Fe_{\odot}$, 0.54 - 1.84 Mg/$Fe_{\odot}$, and 0.5 - 2.0 Ne/$Fe_{\odot}$.

3.2.2 Updates to TYCHO (2015-2016)

The models included in our catalog were simulated using the stellar evolution code TYCHO (Young & Arnett, 2005). As detailed in T15, TYCHO outputs information on stellar surface quantities for each time-step of a star's evolution, which we then use to calculate the inner and outer radii of the HZ as a function of stellar age. New OPAL opacity tables (Iglesias & Rogers, 1996; Rogers & Nayfonov, 2002) were generated at specific abundance values needed for each enriched and depleted C/Fe, Mg/Fe, and Ne/Fe value to match the desired composition of the stellar model. The TYCHO evolutionary tracks are used as input to our HZ calculator (CHAD) which is easily upgradable to incorporate improved HZ predictions as they become available.

We have recently implemented improved low temperature ($\sim$2400 K) opacity tables in TYCHO, and we are now able to more accurately simulate stellar evolutionary tracks, particularly for very low mass stars. The new low temperature opacities are based on Ferguson et al. (2005); Serenelli et al. (2009) and include dust grain opacity. Ultimately, it will be extremely important to include M-stars in our catalog due to the high probability that they may host a habitable world (Borucki et al., 2010,

2011; Batalha et al., 2013). In a future paper we plan to explore the ramifications of variable stellar composition in a grid of M-stars. We have recalculated the original oxygen grid that was discussed in T15; for completeness, at certain stellar parameters of interest, we now provide updated oxygen values alongside the data for carbon, magnesium, and neon.

3.3 Discussion of Results

As we examined at length in T15, the main factors that influence the time evolution of the classical HZ are the host star's luminosity (L) and effective temperature (T_{eff}), their rates of change, and the stellar main sequence (MS) lifetime. TYCHO evolutionary tracks are used to estimate the extent of the HZ at each point in the stellar evolution. For these estimates we follow the prescriptions of Kopparapu et al. (2013, 2014), which proceed from Selsis et al. (2007) and Kasting et al. (1993). These prescriptions parameterize the orbital radii of the HZ as a function of L and T_{eff}, which facilitates the translation from stellar evolution tracks to HZ distance estimations. We reconfirm that mass and scaled metallicity influence these factors considerably. Following from Young et al. (2012) and T15, wherein the focus was variability in the oxygen abundance (ranging from 0.44 to 2.28 $O/Fe_{\odot}$), we now examine the outcome of varying the the abundance ratios of $C/Fe_{\odot}$, $Mg/Fe_{\odot}$, and $Ne/Fe_{\odot}$; these are other elements that are relatively significant to the stellar evolution over the entire range of mass and metallicity represented in our grid.

3.3.1 Stellar Properties and Main Sequence Lifetimes

Table 3.1 shows the MS lifetimes (in Gyr) for standard and end member abundance values for all elements of interest (carbon, updated oxygen values, magnesium, and neon), as well as end member metallicity values, for all masses in our grid. When

considering how a star's specific chemical composition translates to its MS lifetime, we would expect that a star with higher metallicity (or enriched elemental abundances) would live longer than a star of the same mass with lower overall opacity. Surprisingly, this is not what we see for some of the carbon models in our grid. Upon close inspection of the listed table values (particularly for the 1.5 $Z_{\odot}$ cases), an unexpected trend emerges; specifically, it appears that some of the depleted carbon cases (0.58 $C/Fe_{\odot}$) actually have *longer* MS lifetimes than the associated enriched carbon cases (1.72 $C/Fe_{\odot}$). With further examination of the lifetimes given for the other elements, it is clear that the MS lifetimes do not exhibit the same inverted lifetime expectancies for these models as they do for some of the carbon cases.

In order to understand the puzzling behavior of the carbon models, we have examined two possibilities. First, since discrepancies in the expected stellar ages are sufficiently small compared to the overall calculated MS lifetimes, numerical uncertainties in the code that determine where TYCHO terminates the MS may be larger than the variability we measure for the MS lifetimes. TYCHO determines the Terminal Age Main Sequence (TAMS) by stopping the code when the abundance of hydrogen in the innermost model zone drops below 1 part in 10^6. Rezoning in TYCHO is adaptive, so minor differences in the size of the innermost zones and diffusion/convection across those zones can cause small (i.e. $< 1\%$) variation in the output value of the TAMS. Additionally, because of compositional normalization that is applied when creating the opacity tables, the depleted carbon (and magnesium) models start out with slightly more hydrogen to ensure that the total mass fraction = 1, which may allow for some extra MS lifetime if that hydrogen becomes available for burning in the core. For our highest mass stars that develop convective cores the extent of the convective core changes slightly due to the change in electron fraction (the convective core is high enough in temperature to be dominated by electron scattering opacity)

and the energy generation by the CNO cycle with a different amount of catalysts. Additional carbon also shifts the position of the second peak in the opacity versus temperature relationship in the OPAL tables, affecting the position of the base of the convection zone. Each of these are very small effects. It turns out that the variations in lifetime from carbon are also small. Given that the effect is preferentially at higher metallicity and higher mass, the dominant effects are a combination of slightly increased hydrogen mass fraction and central zoning, with enhance convective transport and CNO catalysts playing a role in more massive stars. Overall, the contribution from carbon is insignificant.

Figure 3.1 shows the Hertzsprung-Russell Diagrams (HRDs) for evolutionary tracks from ZAMS (Zero Age Main Sequence) to TAMS for all masses in our grid. The top row is for carbon, where C/Fe = 0.58 $C/Fe_{\odot}$ (dashed), 1.0 $C/Fe_{\odot}$ (solid), and 1.72 $C/Fe_{\odot}$ (dotted), all at $Z = Z_{\odot}$. The middle and bottom rows (respectively) show the similar HRDs for magnesium and neon, where Mg/Fe = 0.54 $Mg/Fe_{\odot}$ and Ne/Fe = 0.5 $Ne/Fe_{\odot}$ (dashed), 1.0 $Mg/Fe_{\odot}$ and 1.0 $Ne/Fe_{\odot}$ (solid), and 1.84 $Mg/Fe_{\odot}$ and 2.0 $Ne/Fe_{\odot}$ (dotted), again at $Z = Z_{\odot}$. The rightward-most dotted lines are for the lowest mass star with enriched elemental abundance values, while the leftward-most dashed line is for the highest mass star with depleted abundance values.

For the higher mass models (the left-hand column of Figure 3.1) we see evidence of the Kelvin-Helmholtz mechanism (KH "jag"), wherein a star nearing the end of its MS lifetime begins to cool and compress due to decreased internal pressure from the end of core hydrogen burning. This compression reheats the core, causing the observed fluctuations in L and T_{eff}. A detailed scrutiny of the figures reveals a slight crossover that occurs in the late MS for both carbon and magnesium, for the depleted (dashed line) cases relative to standard (solid line). The crossover occurs due to the slightly larger core in the high-carbon models; thus, the shift in the KH-jags for these models

on the HR diagram is physical, from variability that exists in the interior structures of the stars. The total abundance of carbon in stars is, generally, a factor of several higher than for that of magnesium (e.g. Lodders (2010)); however, the abundance range of carbon (from 0.58 - 1.72 C/Fe$_\odot$) is smaller than that of magnesium (from 0.54 - 1.84 Mg/Fe$_\odot$), and magnesium contributes more opacity per gram in the stellar interior than carbon does (e.g. Morse (1940)). Thus, magnesium actually makes a bigger difference to the evolution relative to its abundance in stars. Oxygen is not only much more abundant than carbon, but also has a high contribution to the opacity.

Table 3.2 shows $\Delta(L/L_{ZAMS})$ at each mass and end-member composition for all elements. As expected, the change in luminosity over the MS is largest for less enriched compositions except in the case of the higher metallicity, higher mass stars, where the shape of the K-H jag obscures the trend. Table 3.3 similarly shows ΔT_{eff} at each mass and end-member composition for all elements. The lowest mass, lowest opacity models all exhibit the largest change in temperature over the course of their MS lifetimes, even though they don't live quite as long as higher opacity stars at the same mass. Interestingly, even though we see the highest ΔT values for depleted magnesium (0.54 Mg/Fe$_\odot$ at 0.1 Z$_\odot$), the largest change in L actually occurs for the depleted oxygen model (0.44 O/Fe$_\odot$, though also at 0.1 Z$_\odot$).

This work constitutes a sound argument for considering the contributions of neon (and, to some extent, nitrogen) to the stellar evolution. Neon would definitely be an important player in the evolution based on its opacity contributions per unit mass (similar to that of magnesium). It is difficult to assign the appropriate abundance ratio ranges for modeling, as it is challenging to measure neon in stars with much certainty, although work has been done to measure neon abundances from the X-ray spectra of cool stars (Drake & Testa, 2005). For the purposes of this work, we have assigned an artificial range of neon abundances (enriched and depleted by factor of

two from the solar neon abundance, similar to the range of other low Z elements) which we can use to estimate contributions to the stellar evolution. Nitrogen is also not easily measurable in stars, but can probably be safely neglected; it is similar in opacity per gram to carbon, but relatively less abundant in stars, by a factor of about 4 in the Sun (Hansen, Kawaler, & Trimble, 2004). Thus, its contribution to the stellar evolution is likely negligible even though it is more abundant than either magnesium or neon. One exception to this would be if nitrogen is actually ever observed to be widely variable in stars with any future measurements; if the abundance values of nitrogen vary a great deal more between individual stars than other elements, it could be an important consideration.

Now consider the rate of change of the luminosity (Table 3.4) for all masses in our grid at end-member compositions. It is especially useful to look at the change of luminosity per Gyr, because some of the models undergo a larger change in L than do the higher opacity models at the same mass, but potentially over longer or shorter MS lifetimes. This could have different implications for whether the change in luminosity with time is greater or smaller for low opacity models (or if it varies), and whether that occurs during the second half of the star's MS lifetime. With few exceptions, the low opacity models at each mass and elemental composition change more in L per Gyr than their counterparts at higher opacities. Additionally, and as expected, it's clear that the higher mass models experience a significantly larger change in L over the course of their MS lifetimes.

As we understand how the luminosity changes over time (the rate of change, as well as the total change), we see that the range of orbits in the HZ at different points in the MS evolution can vary substantially. Table 3.5 shows the fraction (listed as percentages) of orbital radii that only enter the habitable zone $after$ the midpoint of the MS for each star. The results indicate that up to two thirds of all orbits that

are ever in the HZ only become habitable in the second half of the host star's MS lifetime. The effect is more pronounced at lower mass and depleted composition, at each element of interest. When considering the potential for detectability, it is wise to avoid planets that have only recently entered the HZ of the host star; not only would we potentially circumvent the issue of cold starts (discussed in §3.3), but we also assume that life requires enough time spent in "habitable" conditions before it would yield detectable biosignatures. This is a somewhat narrow assumption that depends on specific habitability considerations; indeed, Silva et al. (2016) introduces an alternative "atmospheric mass HZ for complex life" with an inner edge that is not affected by uncertainties inherent to the calculation of a runaway greenhouse limit.

3.3.2 Location of the Habitable Zone

We produce complete evolutionary tracks for the position of the HZ as a function of time for all stellar models. With an independent age estimate for the star, as well as measurements for mass and specific composition, we can predict the future and past location of a given exoplanet, and whether that planet ever inhabited the parent star's HZ; furthermore, we can assess the timeline for when a planet will enter the HZ, as well as estimate how long the planet has been outside of the HZ if it has already departed. Assuming the aforementioned stellar properties are well measured, the time that an observed exoplanet may exist in the HZ can be estimated to the level of accuracy of the planetary atmosphere models that predict the HZ boundaries.

Generally, we find that a higher abundance of carbon, magnesium, or neon in the host star correlates with a closer-in HZ , because the star is less luminous, at a lower T_{eff}, and the MS lifetime is longer. Likewise, a lower abundance value will typically produce shorter overall MS lifetimes with HZ distances that are farther away from the host star, the same trend that we observed for oxygen abundance ratios in T15.

Figures 3.2, 3.3, and 3.4 show polar plots for carbon, magnesium, and neon, respectively. These figures are meant to demonstrate how the HZ varies between different kinds of stars, and what the differences would look like from a perspective perpendicular to that of a hypothetical planet's orbital plane. These figures each include stars of end-member masses 0.5 $M_{\odot}$ star (top) and a 1.2 $M_{\odot}$ star (bottom), at the lowest and highest composition cases for each element of interest. HZ boundaries are solid for the ZAMS and dashed for the TAMS. The inner and outer HZ boundaries should be clear based on their positions relative to each other. Only the high mass stars exhibit a small degree of overlap between the outer edge at the ZAMS and the inner edge at the TAMS, which might correspond to a "Continuously Habitable Zone" (see §3.3). Given this HZ prescription, it is clear that there are no orbits around the low mass stars that remain within the HZ for the *entire* MS lifetime.

Ultimately, this doesn't matter much in the sense that the lowest mass stars in our sample are sufficiently long-lived that they would still provide a significantly long continuously habitable zone (CHZ). However, we do eventually need to assess the variation of stellar activity with age, particularly for M-dwarf stars, since an extremely long CHZ lifetime would not necessarily be enough to overcome a harsh radiation environment, which are likely to exist around M-stars. We will explore these ideas further in a future paper. From the polar figures we also see that the HZ can change substantially over the MS depending on the host star's specific chemical composition. Tables 3.6 and 3.7 show changes in the location of the HZ radius in AU from ZAMS to TAMS for both the Runaway Greenhouse inner boundary (RGH), and the Maximum Greenhouse outer boundary (MaxGH), respectively, which are the conservative HZ limit cases discussed in Kopparapu et al. (2013, 2014).

The lefthand column of Figure 3.5 shows the inner and outer edges of the HZ for each stellar mass for all compositions at the ZAMS, while the righthand column

shows the same information for the TAMS. The top row is for carbon, the middle row is magnesium, and the bottom row is neon. There are a smaller number of neon lines included since we only modeled the end-member scenarios for the neon cases. We find that for all elements, a higher overall opacity results in the associated HZ boundaries at radii much closer to the host star. As observed with our original grid of oxygen models, we see that with increasing stellar mass, there seems to be a widening of the overall HZ range, as well as a larger spread in the HZ distances due to compositional variation. The spread in specific abundance ratios for each element of interest (at solar metallicity value) are indicated by the elongated solid lines.

The range in distance of the HZ edges for each element at the solar metallicity value is clearly smaller than the range that exists for the variations in overall scaled metallicity. This is expected, since the total change in opacity of the stellar material is much larger for a factor of fifteen change in total Z than a factor of about two change in each elemental abundance. This figure also similarly includes the spread in carbon, magnesium, or neon, calculated at each scaled metallicity value. The elongated dotted lines represent the end-member values for the spread in the carbon, magnesium, and neon abundances (0.58 C/Fe$_\odot$, 1.72 C/Fe$_\odot$, 0.54 Mg/Fe$_\odot$, 1.84 Mg/Fe$_\odot$, 0.5 Ne/Fe$_\odot$ and 2.0 Ne/Fe$_\odot$, respectively) calculated at end-member metallicity values (0.1 and 1.5 Z$_\odot$). These models extend the range of HZ distance even further than do the models for elemental abundances at Z$_\odot$ alone. The observed difference in HZ location as a function of composition is larger for higher mass stars because the absolute change in L is larger. Additionally, the outer HZ edge changes more than that of the inner edge because calculation for the Maximum Greenhouse limit is more sensitive to the spectrum of the incoming radiation and T_{eff}.

A higher specific elemental abundance ratio present in the host star will generally result in a closer HZ, because the star would be less luminous and at a lower effective

temperature. Additionally, a higher-opacity star will be much more efficient in its burning process, and consequently it will live significantly longer on the MS than for a star of equal mass at lower opacity. Figure 3.6 shows the HZ distance as it changes with stellar age, for three stellar mass values (top is 0.5 $M_{\odot}$, middle is 1.0 $M_{\odot}$, bottom is 1.2 $M_{\odot}$), for five different compositions at each element of interest (carbon in left column, magnesium in middle column, neon in right column). Each shaded line represents a different abundance value: black is solar, light gray is for depleted elemental values (0.58 C/Fe, 0.54 Mg/Fe, 0.5 Ne/Fe), and dark gray is for enriched elemental values (1.72 C/Fe, 1.84 Mg/Fe, 2.0 Ne/Fe). For comparison, the lines shaded lightest gray are 0.1 $Z_{\odot}$ (easily identifiable by its truncated lifetime) and 1.5 $Z_{\odot}$ (both at standard value). A 1 AU orbit is also indicated by the dotted line, for reference. It is clear that abundance variations within a star significantly affect MS lifetime and HZ distance. As expected, the shortest lifetime corresponds to a star with total metallicity Z = 0.1 $Z_{\odot}$ and the longest lifetime corresponds to Z = 1.5 $Z_{\odot}$. However, when considering only the variations in the specific elemental abundances, we see that changes in magnesium and neon make the largest difference to the evolution, followed by carbon. The total MS lifetime for a 0.5 $M_{\odot}$ star at end-member neon abundances (at $Z_{\odot}$) varies by about 7 Gyr, which can also be determined by examining Table 3.1. Likewise, the MS varies by about 4 Gyr for magnesium, and only about 1 Gyr for carbon.

3.3.3 Continuously Habitable Zones

It should now be abundantly clear that it is an extremely useful pursuit to quantify how long any given planet would remain in a star's HZ as a function of its orbital distance; however, the instantaneous habitability of a planet alone is insufficient to determine the likelihood that it actually hosts extant life, or whether any life present

would even be detectable. Groups at the Virtual Planet Laboratory at the University of Washington have worked on this problem from the perspective of viewing the Earth as an exoplanet, in order to determine the current technological limits of what "biosignatures" might be measurable in the atmospheres of real exoplanets (e.g. Harman et al. (2015); Krissansen-Totton et al. (2016)). This kind of information plays an integral role in determining how we think about habitability; indeed, with more sophisticated planetary atmosphere models and a broader understanding of what might be directly observable about them (Kasting et al., 2014), we will have a better idea of how to apply the data from our stellar evolution tracks to paint a more complete picture of HZ evolution around different types of stars.

In T15, our initial goal was to estimate a continuously habitable zone (CHZ) for each star in our catalog, which would simply include a range of orbital radii that remain in the HZ for the entire MS. The CHZ is rather straightforwardly defined by considering the boundary overlap between ZAMS and TAMS. The lefthand column of Figure 3.7 shows the CHZ for stars of all masses in our grid, at a composition of solar metallicity and enriched abundance values for each element of interest. The top row is for carbon, the middle is magnesium, and the bottom is neon. It is clear that the low mass stars have no CHZ for the conservative HZ limits (at all elements), which would seem to indicate that low mass stars would have a low statistical likelihood to host a long-term habitable planet; however, that is somewhat misleading due to the extremely long MS lifetimes of low mass stars.

Thus, we have defined a much more useful 2 Gyr CHZ (the CHZ_2), which is the range of orbital radii that would be continuously habitable for at least 2 billion years. We use this time because it is estimated that life on Earth took approximately 2 Gyr to produce a measurable chemical change in the atmosphere (Summons et al., 1999; Kasting & Catling, 2003; Holland, 2006). Of course, the CHZ_2 assumes that Earth's

timescale for the evolution of life with the capability to modify the entire planetary atmosphere is representative of the norm. This is not meant to imply that other suggested timescales are at all unreasonable (e.g. Rushby et al. (2013)), but in order to narrow down the large pool of potentially habitable exoplanets to the ones that would have the highest potential for both long-term habitability *and* detectability, there is an advantage in using Earth's history as a starting point. In addition, we provide a robust consideration of the HZ's co-evolution with the host star, because we have incorporated detailed stellar properties.

The righthand column of Figure 3.7 shows the orbits that remain habitable for at least 2 Gyr (CHZ_2). This is determined from the inner edge of the HZ at 2 Gyr after the beginning of the MS and the outer edge 2 Gyr before the TAMS. Now we see that the significantly longer MS lifetimes of the low mass stars create a higher proportion of the HZ that is included in the CHZ_2 than for the basic CHZ. Based on these results, we would be less likely to find a planet that has been in the CHZ for at least 2 Gyr orbiting a more massive star; at the very least, we would be less confident that a planet located outside of the CHZ_2 would produce detectable biosignatures than one within the CHZ_2. Table 3.8 shows the fraction of time a planet would spend in the CHZ_2 vs. time it would spend in the HZ over its entire MS lifetime. Comparing stars of interest with chemical compositions will inform which ones we should focus on in the continued search for detectable inhabited exoplanets.

As in T15, our consideration of HZ evolution and the CHZ must also address the issue of cold starts. Our discussion until now has assumed that any planets initially beyond the boundaries of the HZ could easily become habitable as soon as the host star's HZ expanded outward to engulf them; indeed, the albedos used in the planetary atmosphere models of Kopparapu et al. (2014) are relatively low, which assumes a planet could fairly easily become habitable upon entering the HZ. However, it may be

unlikely that a completely frozen planet (a "hard snowball") entering the HZ late in the host star's MS lifetime would receive enough energy in the form of stellar radiation to reverse a global glaciation, especially if the planet harbors reflective CO_2 clouds (Caldeira & Kasting, 1992; Kasting et al., 1993).

Figure 3.8 offers an alternative scenario to that of Figure 3.6, wherein we presumed a cold start would be possible and thus allowed the outer HZ limit to expand with time. Instead, we now treat the outer boundary of the HZ at ZAMS as a hard limit that does not co-evolve with the star, so a particular planet would be required to exist in the HZ from the beginning of the host star's MS in order to be considered habitable over the long-term. Obviously, a planet that is in a star's HZ from very early times would not face the problem of a cold start. We defer discussion of the cold start problem as applied to the CHZ to our previous paper.

3.4 Conclusions

As we have discussed at length here and in T15, the stellar evolution depends strongly on composition. It is important to distinguish between the metallicity of a star as measured by [Fe/H] and the specific abundances of individual elements. Though we discuss the concept of overall scaled "metallicity" as the abundance of all heavy elements scaled relative to solar value, the term is often used interchangeably with [Fe/H]. The typical approach to stellar modeling is to measure the iron in a star and assume that every individual element scales in the same proportions as observed in the Sun, though the abundances in actual stars can vary significantly.

We have also provided additional evidence that the HZ distance can be substantially affected even when only abundance ratios are changed. Evaluating habitability potential by modeling the co-evolution of stars and HZs requires models that span a range of variation in abundance ratios, as well as total scaled metallicity. For the

same reason, characterizing a system requires obtaining measurements of multiple specific elemental abundances, not just [Fe/H].

In this paper, we discussed the new models we have created for inclusion in our catalog of stellar evolution profiles. We have considered variation in the abundance ratios for carbon (0.58-1.72 C/Fe$_\odot$), magnesium (0.54-1.84 Mg/Fe$_\odot$), and neon (0.5-2.0 Ne/Fe$_\odot$) and investigated how each of these elements affects the co-evolution of stars and HZs. Though carbon is the most abundant of these, we find that magnesium provides the largest contribution to the opacity and produces the largest changes in MS lifetime, L, and T_{eff}. For this set of elements the effects on lifetimes and luminosities are smaller than typical observational uncertainties. This will change using high-precision distance measurements from Gaia, for a much more accurate determination of luminosities (the largest source of error in stellar age). Gaia will acquire distance measurements of our nearest stellar neighbors to an accuracy of 0.001% and will provide parallaxes and proper motions with accuracy ranging from 10 to 1000 microarcseconds for over one billion stars. For an unreddened K-giant at 6 kpc, it will provide a distance measurement accurate to 15% and the transverse velocity to an accuracy of about 1 km/s. Even stars near the center of the galaxy will have distance measurements to within an accuracy of 20% (e.g. Bailer-Jones (2009)). For nearby stars, the L uncertainty attributable to distance error will be of order 0.3%, and the dominant source of error will be bolometric corrections.

Many targets of radial velocity planet searches have high quality spectra that can be used to determine stellar abundances, and it should be standard practice to compare stellar models with observed compositions. To this end, we have updated the online database of stellar evolution models and predicted HZs to include the 528 new models discussed in this paper. The library will be extended in the future to include a comprehensive grid for very low mass M-dwarf stars and evolved stars.

Composition	0.5 $M_\odot$	0.6 $M_\odot$	0.7 $M_\odot$	0.8 $M_\odot$	0.9 $M_\odot$	1.0 $M_\odot$	1.1 $M_\odot$	1.2 $M_\odot$
0.1 $Z_\odot$, 0.58 C/Fe$_\odot$	69.067	40.446	22.575	13.475	8.618	5.825	4.099	2.960
0.1 $Z_\odot$, C/Fe$_\odot$	70.579	41.228	23.089	13.741	8.778	5.914	4.154	2.996
0.1 $Z_\odot$, 1.72 C/Fe$_\odot$	73.251	43.010	24.037	14.245	9.072	6.094	4.274	3.073
$Z_\odot$, 0.58 C/Fe$_\odot$	109.038	72.578	45.839	26.770	16.185	10.408	6.916	5.060
$Z_\odot$, C/Fe$_\odot$	109.490	72.762	45.853	26.691	16.123	10.363	6.902	5.029
$Z_\odot$, 1.72 C/Fe$_\odot$	110.992	73.605	46.274	26.849	16.141	10.364	6.903	5.091
1.5 $Z_\odot$, 0.58 C/Fe$_\odot$	114.774	77.401	50.089	30.009	18.158	11.651	7.716	5.634
1.5 $Z_\odot$, C/Fe$_\odot$	114.328	76.838	49.495	29.513	17.831	11.459	7.608	5.578
1.5 $Z_\odot$, 1.72 C/Fe$_\odot$	113.697	75.978	48.530	28.672	17.291	11.107	7.391	5.571
0.1 $Z_\odot$, 0.44 O/Fe$_\odot$	65.047	37.352	20.954	12.586	8.095	5.496	3.878	2.823
0.1 $Z_\odot$, O/Fe$_\odot$	70.579	41.228	23.089	13.741	8.778	5.914	4.154	2.996
0.1 $Z_\odot$, 2.28 O/Fe$_\odot$	82.565	50.281	28.579	16.742	10.492	6.974	4.848	3.481
$Z_\odot$, 0.44 O/Fe$_\odot$	102.238	66.968	41.196	23.657	14.494	9.397	6.322	4.580
$Z_\odot$, O/Fe$_\odot$	109.490	72.762	45.853	26.691	16.123	10.363	6.902	5.029
$Z_\odot$, 2.28 O/Fe$_\odot$	120.713	82.074	52.680	31.429	18.586	11.789	7.776	5.826
1.5 $Z_\odot$, 0.44 O/Fe$_\odot$	109.250	72.825	46.198	27.129	16.495	10.687	7.162	5.214
1.5 $Z_\odot$, O/Fe$_\odot$	114.328	76.838	49.495	29.513	17.831	11.459	7.608	5.578
1.5 $Z_\odot$, 2.28 O/Fe$_\odot$	118.072	79.284	51.197	30.807	18.400	11.671	8.197	5.984
0.1 $Z_\odot$, 0.54 Mg/Fe$_\odot$	69.918	40.721	22.791	13.584	8.678	5.855	4.121	2.973
0.1 $Z_\odot$, Mg/Fe$_\odot$	70.579	41.228	23.089	13.741	8.778	5.914	4.154	2.996
0.1 $Z_\odot$, 1.84 Mg/Fe$_\odot$	71.798	42.171	23.638	14.040	8.957	6.029	4.235	3.052
$Z_\odot$, 0.54 Mg/Fe$_\odot$	107.956	71.461	44.730	25.910	15.691	10.105	6.728	4.939
$Z_\odot$, Mg/Fe$_\odot$	109.490	72.762	45.853	26.691	16.123	10.363	6.902	5.029
$Z_\odot$, 1.84 Mg/Fe$_\odot$	112.245	75.150	47.931	28.215	16.934	10.864	7.221	5.265
1.5 $Z_\odot$, 0.54 Mg/Fe$_\odot$	112.890	75.632	48.427	28.702	17.382	11.179	7.427	5.490
1.5 $Z_\odot$, Mg/Fe$_\odot$	114.328	76.838	49.495	29.513	17.831	11.459	7.608	5.578
1.5 $Z_\odot$, 1.84 Mg/Fe$_\odot$	116.918	78.997	51.409	31.181	18.702	11.988	7.948	5.789
0.1 $Z_\odot$, 0.5 Ne/Fe$_\odot$	69.107	40.151	22.476	13.407	8.577	5.792	4.078	2.940
0.1 $Z_\odot$, Ne/Fe$_\odot$	70.579	41.228	23.089	13.741	8.778	5.914	4.154	2.996
0.1 $Z_\odot$, 2.0 Ne/Fe$_\odot$	73.572	43.452	24.364	14.432	9.185	6.171	4.329	3.123
$Z_\odot$, 0.5 Ne/Fe$_\odot$	107.476	71.110	44.497	25.802	15.670	10.111	6.743	4.953
$Z_\odot$, Ne/Fe$_\odot$	109.490	72.762	45.853	26.691	16.123	10.363	6.902	5.029
$Z_\odot$, 2.0 Ne/Fe$_\odot$	114.068	76.425	48.860	28.793	17.194	10.990	7.289	5.314
1.5 $Z_\odot$, 0.5 Ne/Fe$_\odot$	112.578	75.448	48.339	28.694	17.391	11.202	7.453	5.522
1.5 $Z_\odot$, Ne/Fe$_\odot$	114.328	76.838	49.495	29.513	17.831	11.459	7.608	5.578
1.5 $Z_\odot$, 2.0 Ne/Fe$_\odot$	117.587	79.362	51.609	31.251	18.688	11.945	7.904	5.751

Table 3.1 MS lifetime (Gyr), each mass and end-member composition, all elements.

Composition	0.5 $M_\odot$	0.6 $M_\odot$	0.7 $M_\odot$	0.8 $M_\odot$	0.9 $M_\odot$	1.0 $M_\odot$	1.1 $M_\odot$	1.2 $M_\odot$
0.1 $Z_\odot$, 0.58 C/Fe$_\odot$	5.717	6.004	4.363	3.013	2.388	1.955	1.618	1.373
0.1 $Z_\odot$, C/Fe$_\odot$	5.679	5.815	4.368	2.981	2.357	1.918	1.584	1.341
0.1 $Z_\odot$, 1.72 C/Fe$_\odot$	5.655	5.813	4.397	2.944	2.312	1.883	1.549	1.302
$Z_\odot$, 0.58 C/Fe$_\odot$	3.137	3.956	4.175	3.278	1.993	1.516	1.207	1.174
$Z_\odot$, C/Fe$_\odot$	2.995	3.823	4.056	3.185	1.929	1.483	1.209	1.190
$Z_\odot$, 1.72 C/Fe$_\odot$	2.821	3.638	3.882	3.062	1.840	1.433	1.200	1.224
1.5 $Z_\odot$, 0.58 C/Fe$_\odot$	2.623	3.400	3.739	3.141	1.938	1.462	1.170	1.155
1.5 $Z_\odot$, C/Fe$_\odot$	2.495	3.264	3.591	2.994	1.844	1.419	1.174	1.192
1.5 $Z_\odot$, 1.72 C/Fe$_\odot$	2.398	3.098	3.394	2.777	1.702	1.350	1.157	1.241
0.1 $Z_\odot$, 0.44 O/Fe$_\odot$	5.928	5.857	4.335	3.061	2.438	2.004	1.681	1.420
0.1 $Z_\odot$, O/Fe$_\odot$	5.679	5.815	4.368	2.981	2.357	1.918	1.584	1.341
0.1 $Z_\odot$, 2.28 O/Fe$_\odot$	5.224	5.734	4.733	3.097	2.300	1.847	1.512	1.246
$Z_\odot$, 0.44 O/Fe$_\odot$	3.198	4.017	4.139	2.980	1.904	1.511	1.260	1.206
$Z_\odot$, O/Fe$_\odot$	2.995	3.823	4.056	3.185	1.929	1.483	1.209	1.190
$Z_\odot$, 2.28 O/Fe$_\odot$	2.679	3.498	3.829	3.295	1.957	1.425	1.108	1.1998
1.5 $Z_\odot$, 0.44 O/Fe$_\odot$	2.679	3.467	3.740	2.973	1.838	1.451	1.226	1.214
1.5 $Z_\odot$, O/Fe$_\odot$	2.495	3.264	3.591	2.994	1.844	1.419	1.174	1.192
1.5 $Z_\odot$, 2.28 O/Fe$_\odot$	2.293	3.031	3.362	3.254	1.713	1.288	1.257	1.2002
0.1 $Z_\odot$, 0.54 Mg/Fe$_\odot$	5.700	5.799	4.331	2.973	2.343	1.911	1.586	1.344
0.1 $Z_\odot$, Mg/Fe$_\odot$	5.679	5.815	4.368	2.981	2.357	1.918	1.584	1.341
0.1 $Z_\odot$, 1.84 Mg/Fe$_\odot$	5.637	5.834	4.423	3.004	2.367	1.928	1.595	1.354
$Z_\odot$, 0.54 Mg/Fe$_\odot$	3.049	3.872	4.067	3.120	1.903	1.471	1.198	1.191
$Z_\odot$, Mg/Fe$_\odot$	2.995	3.823	4.056	3.185	1.929	1.483	1.209	1.190
$Z_\odot$, 1.84 Mg/Fe$_\odot$	3.426	3.729	4.029	3.297	1.986	1.510	1.230	1.214
1.5 $Z_\odot$, 0.54 Mg/Fe$_\odot$	2.540	3.314	3.613	2.953	1.817	1.405	1.164	1.197
1.5 $Z_\odot$, Mg/Fe$_\odot$	2.495	3.264	3.591	2.994	1.844	1.419	1.174	1.192
1.5 $Z_\odot$, 1.84 Mg/Fe$_\odot$	2.415	3.173	3.553	3.471	1.896	1.443	1.189	1.196
0.1 $Z_\odot$, 0.5 Ne/Fe$_\odot$	5.712	5.779	4.297	2.955	2.332	1.909	1.577	1.333
0.1 $Z_\odot$, Ne/Fe$_\odot$	5.679	5.815	4.368	2.981	2.357	1.918	1.584	1.341
0.1 $Z_\odot$, 2.0 Ne/Fe$_\odot$	5.614	5.877	4.515	3.038	2.387	1.944	1.608	1.369
$Z_\odot$, 0.5 Ne/Fe$_\odot$	3.069	3.884	4.067	3.099	1.903	1.472	1.200	1.197
$Z_\odot$, Ne/Fe$_\odot$	2.995	3.823	4.056	3.185	1.929	1.483	1.209	1.190
$Z_\odot$, 2.0 Ne/Fe$_\odot$	2.867	3.701	4.036	3.353	2.006	1.517	1.232	1.221
1.5 $Z_\odot$, 0.5 Ne/Fe$_\odot$	2.555	3.321	3.613	2.946	1.819	1.409	1.165	1.202
1.5 $Z_\odot$, Ne/Fe$_\odot$	2.495	3.264	3.591	2.994	1.844	1.419	1.174	1.192
1.5 $Z_\odot$, 2.0 Ne/Fe$_\odot$	2.395	3.155	3.542	3.474	1.892	1.439	1.187	1.194

Table 3.2 $\Delta(L/L_{ZAMS})$, each mass and end-member composition, all elements.

Composition	0.5 $M_\odot$	0.6 $M_\odot$	0.7 $M_\odot$	0.8 $M_\odot$	0.9 $M_\odot$	1.0 $M_\odot$	1.1 $M_\odot$	1.2 $M_\odot$
0.1 $Z_\odot$, 0.58 C/Fe$_\odot$	1173	1231	708	277	150	141	240	229
0.1 $Z_\odot$, C/Fe$_\odot$	1175	1119	733	281	146	126	221	216
0.1 $Z_\odot$, 1.72 C/Fe$_\odot$	1183	1151	788	292	144	114	203	210
$Z_\odot$, 0.58 C/Fe$_\odot$	745	840	929	771	270	72	-27	-116
$Z_\odot$, C/Fe$_\odot$	717	825	915	758	257	68	-21	-86
$Z_\odot$, 1.72 C/Fe$_\odot$	688	798	892	744	249	67	-16	-85
1.5 $Z_\odot$, 0.58 C/Fe$_\odot$	630	721	802	732	298	99	0	-86
1.5 $Z_\odot$, C/Fe$_\odot$	613	706	789	704	275	87	9	-59
1.5 $Z_\odot$, 1.72 C/Fe$_\odot$	592	687	766	668	242	78	19	-59
0.1 $Z_\odot$, 0.44 O/Fe$_\odot$	1160	1052	633	253	156	203	316	272
0.1 $Z_\odot$, O/Fe$_\odot$	1175	1119	733	281	146	126	221	216
0.1 $Z_\odot$, 2.28 O/Fe$_\odot$	1161	1175	969	404	170	86	79	118
$Z_\odot$, 0.44 O/Fe$_\odot$	758	868	977	661	192	21	-49	-103
$Z_\odot$, O/Fe$_\odot$	717	825	915	758	257	68	-21	-86
$Z_\odot$, 2.28 O/Fe$_\odot$	643	718	813	776	333	108	14	-98
1.5 $Z_\odot$, 0.44 O/Fe$_\odot$	658	765	854	708	243	65	-17	-72
1.5 $Z_\odot$, O/Fe$_\odot$	613	706	789	704	275	87	9	-59
1.5 $Z_\odot$, 2.28 O/Fe$_\odot$	576	653	728	859	255	82	-25	-80
0.1 $Z_\odot$, 0.54 Mg/Fe$_\odot$	1182	1118	723	277	149	140	236	219
0.1 $Z_\odot$, Mg/Fe$_\odot$	1175	1119	733	281	146	126	221	216
0.1 $Z_\odot$, 1.84 Mg/Fe$_\odot$	1171	1125	754	285	143	110	201	200
$Z_\odot$, 0.54 Mg/Fe$_\odot$	733	840	934	739	245	61	-20	-97
$Z_\odot$, Mg/Fe$_\odot$	717	825	915	758	257	68	-21	-86
$Z_\odot$, 1.84 Mg/Fe$_\odot$	655	802	889	779	287	83	-13	-89
1.5 $Z_\odot$, 0.54 Mg/Fe$_\odot$	619	719	802	697	263	83	1	-62
1.5 $Z_\odot$, Mg/Fe$_\odot$	613	706	789	704	275	87	9	-59
1.5 $Z_\odot$, 1.84 Mg/Fe$_\odot$	604	687	767	906	296	98	17	-53
0.1 $Z_\odot$, 0.5 Ne/Fe$_\odot$	1180	1114	715	277	156	147	250	225
0.1 $Z_\odot$, Ne/Fe$_\odot$	1175	1119	733	281	146	126	221	216
0.1 $Z_\odot$, 2.0 Ne/Fe$_\odot$	1168	1134	787	294	142	94	175	197
$Z_\odot$, 0.5 Ne/Fe$_\odot$	740	848	942	739	247	62	-19	-96
$Z_\odot$, Ne/Fe$_\odot$	717	825	915	758	257	68	-21	-86
$Z_\odot$, 2.0 Ne/Fe$_\odot$	687	783	868	782	292	84	-15	-86
1.5 $Z_\odot$, 0.5 Ne/Fe$_\odot$	628	722	808	702	266	84	1	-63
1.5 $Z_\odot$, Ne/Fe$_\odot$	613	706	789	704	275	87	9	-59
1.5 $Z_\odot$, 2.0 Ne/Fe$_\odot$	592	675	753	891	290	91	8	-57

Table 3.3 ΔT_{eff} (K), each mass and end-member composition, all elements.

Composition	0.5 $M_\odot$	0.6 $M_\odot$	0.7 $M_\odot$	0.8 $M_\odot$	0.9 $M_\odot$	1.0 $M_\odot$	1.1 $M_\odot$	1.2 $M_\odot$
0.1 $Z_\odot$, 0.58 C/Fe$_\odot$	0.083	0.149	0.193	0.224	0.277	0.336	0.395	0.464
0.1 $Z_\odot$, C/Fe$_\odot$	0.081	0.141	0.189	0.217	0.269	0.324	0.381	0.448
0.1 $Z_\odot$, 1.72 C/Fe$_\odot$	0.077	0.135	0.183	0.207	0.255	0.309	0.363	0.424
$Z_\odot$, 0.58 C/Fe$_\odot$	0.029	0.055	0.091	0.122	0.123	0.146	0.174	0.232
$Z_\odot$, C/Fe$_\odot$	0.027	0.053	0.089	0.119	0.120	0.143	0.175	0.237
$Z_\odot$, 1.72 C/Fe$_\odot$	0.025	0.049	0.084	0.114	0.114	0.138	0.174	0.240
1.5 $Z_\odot$, 0.58 C/Fe$_\odot$	0.023	0.044	0.075	0.105	0.107	0.126	0.152	0.205
1.5 $Z_\odot$, C/Fe$_\odot$	0.022	0.043	0.073	0.102	0.103	0.124	0.154	0.214
1.5 $Z_\odot$, 1.72 C/Fe$_\odot$	0.021	0.041	0.070	0.100	0.098	0.122	0.157	0.223
0.1 $Z_\odot$, 0.44 O/Fe$_\odot$	0.091	0.157	0.207	0.243	0.301	0.365	0.434	0.503
0.1 $Z_\odot$, O/Fe$_\odot$	0.081	0.141	0.189	0.217	0.269	0.324	0.381	0.448
0.1 $Z_\odot$, 2.28 O/Fe$_\odot$	0.063	0.114	0.166	0.185	0.219	0.265	0.312	0.358
$Z_\odot$, 0.44 O/Fe$_\odot$	0.031	0.060	0.101	0.126	0.131	0.161	0.199	0.263
$Z_\odot$, O/Fe$_\odot$	0.027	0.053	0.089	0.119	0.120	0.143	0.175	0.237
$Z_\odot$, 2.28 O/Fe$_\odot$	0.022	0.043	0.073	0.105	0.105	0.121	0.142	0.206
1.5 $Z_\odot$, 0.44 O/Fe$_\odot$	0.025	0.048	0.081	0.110	0.111	0.136	0.171	0.233
1.5 $Z_\odot$, O/Fe$_\odot$	0.022	0.043	0.073	0.102	0.103	0.124	0.154	0.214
1.5 $Z_\odot$, 2.28 O/Fe$_\odot$	0.019	0.038	0.066	0.106	0.093	0.110	0.153	0.201
0.1 $Z_\odot$, 0.54 Mg/Fe$_\odot$	0.082	0.142	0.190	0.219	0.270	0.326	0.385	0.452
0.1 $Z_\odot$, Mg/Fe$_\odot$	0.081	0.141	0.189	0.217	0.269	0.324	0.381	0.448
0.1 $Z_\odot$, 1.84 Mg/Fe$_\odot$	0.079	0.138	0.187	0.214	0.264	0.320	0.377	0.444
$Z_\odot$, 0.54 Mg/Fe$_\odot$	0.028	0.054	0.091	0.120	0.121	0.146	0.178	0.241
$Z_\odot$, Mg/Fe$_\odot$	0.027	0.053	0.089	0.119	0.120	0.143	0.175	0.237
$Z_\odot$, 1.84 Mg/Fe$_\odot$	0.031	0.050	0.084	0.117	0.117	0.139	0.170	0.231
1.5 $Z_\odot$, 0.54 Mg/Fe$_\odot$	0.023	0.044	0.075	0.103	0.105	0.126	0.157	0.218
1.5 $Z_\odot$, Mg/Fe$_\odot$	0.022	0.043	0.073	0.102	0.103	0.124	0.154	0.214
1.5 $Z_\odot$, 1.84 Mg/Fe$_\odot$	0.021	0.040	0.069	0.111	0.101	0.120	0.150	0.207
0.1 $Z_\odot$, 0.5 Ne/Fe$_\odot$	0.083	0.144	0.191	0.220	0.272	0.330	0.387	0.453
0.1 $Z_\odot$, Ne/Fe$_\odot$	0.081	0.141	0.189	0.217	0.269	0.324	0.381	0.448
0.1 $Z_\odot$, 2.0 Ne/Fe$_\odot$	0.076	0.135	0.185	0.211	0.260	0.315	0.371	0.439
$Z_\odot$, 0.5 Ne/Fe$_\odot$	0.029	0.055	0.091	0.120	0.121	0.146	0.178	0.242
$Z_\odot$, Ne/Fe$_\odot$	0.027	0.053	0.089	0.119	0.120	0.143	0.175	0.237
$Z_\odot$, 2.0 Ne/Fe$_\odot$	0.025	0.048	0.083	0.116	0.117	0.138	0.169	0.230
1.5 $Z_\odot$, 0.5 Ne/Fe$_\odot$	0.023	0.044	0.075	0.103	0.105	0.126	0.156	0.218
1.5 $Z_\odot$, Ne/Fe$_\odot$	0.022	0.043	0.073	0.102	0.103	0.124	0.154	0.214
1.5 $Z_\odot$, 2.0 Ne/Fe$_\odot$	0.020	0.040	0.069	0.111	0.101	0.120	0.150	0.208

Table 3.4 [d(L/L_{ZAMS})/dt], each mass and end-member composition, all elements.

Composition	0.5 $M_\odot$	0.6 $M_\odot$	0.7 $M_\odot$	0.8 $M_\odot$	0.9 $M_\odot$	1.0 $M_\odot$	1.1 $M_\odot$	1.2 $M_\odot$
0.1 $Z_\odot$, 0.58 C/Fe$_\odot$	66.15	67.75	56.84	53.13	48.76	44.74	40.91	37.52
0.1 $Z_\odot$, C/Fe$_\odot$	66.13	61.99	56.57	52.82	48.40	44.36	40.54	37.07
0.1 $Z_\odot$, 1.72 C/Fe$_\odot$	66.00	62.10	56.25	52.47	47.89	43.78	39.91	36.52
$Z_\odot$, 0.58 C/Fe$_\odot$	60.95	61.20	56.45	48.27	43.62	38.42	33.45	34.02
$Z_\odot$, C/Fe$_\odot$	60.16	60.60	55.88	47.58	42.86	37.71	32.91	33.00
$Z_\odot$, 1.72 C/Fe$_\odot$	59.22	59.76	55.08	46.52	41.69	36.52	31.91	32.57
1.5 $Z_\odot$, 0.58 C/Fe$_\odot$	58.58	59.38	55.74	47.61	42.57	37.23	32.27	32.58
1.5 $Z_\odot$, C/Fe$_\odot$	57.63	58.53	54.71	46.58	41.57	36.28	31.45	31.79
1.5 $Z_\odot$, 1.72 C/Fe$_\odot$	56.37	57.43	53.25	44.98	39.87	34.66	30.13	31.70

Table 3.5 Fraction (%) of radii which enter the HZ after midpoint of MS (carbon).

*Note: values in this table have been corrected, and differ from the published version.

Composition	0.5 $M_\odot$	0.6 $M_\odot$	0.7 $M_\odot$	0.8 $M_\odot$	0.9 $M_\odot$	1.0 $M_\odot$	1.1 $M_\odot$	1.2 $M_\odot$
0.1 $Z_\odot$, 0.58 C/Fe$_\odot$	0.468	0.596	0.673	0.712	0.756	0.791	0.798	0.818
0.1 $Z_\odot$, C/Fe$_\odot$	0.463	0.589	0.666	0.701	0.744	0.775	0.782	0.798
0.1 $Z_\odot$, 1.72 C/Fe$_\odot$	0.455	0.579	0.655	0.686	0.725	0.756	0.761	0.771
$Z_\odot$, 0.58 C/Fe$_\odot$	0.271	0.367	0.452	0.494	0.478	0.487	0.497	0.593
$Z_\odot$, C/Fe$_\odot$	0.261	0.357	0.442	0.484	0.467	0.478	0.495	0.589
$Z_\odot$, 1.72 C/Fe$_\odot$	0.247	0.342	0.426	0.467	0.449	0.463	0.486	0.593
1.5 $Z_\odot$, 0.58 C/Fe$_\odot$	0.231	0.320	0.403	0.449	0.435	0.440	0.451	0.541
1.5 $Z_\odot$, C/Fe$_\odot$	0.222	0.310	0.391	0.436	0.421	0.431	0.449	0.546
1.5 $Z_\odot$, 1.72 C/Fe$_\odot$	0.213	0.297	0.375	0.416	0.400	0.415	0.441	0.560
0.1 $Z_\odot$, 0.54 Mg/Fe$_\odot$	0.465	0.590	0.666	0.703	0.743	0.774	0.783	0.8015
0.1 $Z_\odot$, Mg/Fe$_\odot$	0.463	0.589	0.666	0.701	0.744	0.775	0.782	0.798
0.1 $Z_\odot$, 1.84 Mg/Fe$_\odot$	0.459	0.585	0.663	0.699	0.741	0.775	0.784	0.8017
$Z_\odot$, 0.54 Mg/Fe$_\odot$	0.264	0.362	0.446	0.484	0.468	0.480	0.496	0.596
$Z_\odot$, Mg/Fe$_\odot$	0.261	0.357	0.442	0.484	0.467	0.478	0.495	0.589
$Z_\odot$, 1.84 Mg/Fe$_\odot$	0.272	0.349	0.435	0.482	0.465	0.475	0.492	0.589
1.5 $Z_\odot$, 0.54 Mg/Fe$_\odot$	0.225	0.314	0.395	0.438	0.422	0.433	0.451	0.554
1.5 $Z_\odot$, Mg/Fe$_\odot$	0.222	0.310	0.391	0.436	0.421	0.431	0.449	0.546
1.5 $Z_\odot$, 1.84 Mg/Fe$_\odot$	0.216	0.302	0.384	0.449	0.420	0.428	0.445	0.538
0.1 $Z_\odot$, 0.5 Ne/Fe$_\odot$	0.467	0.592	0.667	0.703	0.743	0.775	0.780	0.798
0.1 $Z_\odot$, Ne/Fe$_\odot$	0.463	0.589	0.666	0.701	0.744	0.775	0.782	0.798
0.1 $Z_\odot$, 2.0 Ne/Fe$_\odot$	0.455	0.582	0.663	0.698	0.740	0.776	0.787	0.805
$Z_\odot$, 0.5 Ne/Fe$_\odot$	0.266	0.363	0.447	0.484	0.468	0.481	0.500	0.598
$Z_\odot$, Ne/Fe$_\odot$	0.261	0.357	0.442	0.484	0.467	0.478	0.495	0.589
$Z_\odot$, 2.0 Ne/Fe$_\odot$	0.251	0.345	0.433	0.483	0.465	0.474	0.491	0.589
1.5 $Z_\odot$, 0.5 Ne/Fe$_\odot$	0.227	0.315	0.396	0.438	0.423	0.434	0.451	0.555
1.5 $Z_\odot$, Ne/Fe$_\odot$	0.222	0.310	0.391	0.436	0.421	0.431	0.449	0.546
1.5 $Z_\odot$, 2.0 Ne/Fe$_\odot$	0.214	0.300	0.382	0.448	0.419	0.427	0.445	0.538

Table 3.6 ΔAU, each mass and end-member composition, inner limit (RGH).

Composition	0.5 $M_\odot$	0.6 $M_\odot$	0.7 $M_\odot$	0.8 $M_\odot$	0.9 $M_\odot$	1.0 $M_\odot$	1.1 $M_\odot$	1.2 $M_\odot$
0.1 $Z_\odot$, 0.58 C/Fe$_\odot$	0.816	1.032	1.166	1.240	1.315	1.372	1.396	1.469
0.1 $Z_\odot$, C/Fe$_\odot$	0.808	1.021	1.153	1.221	1.294	1.345	1.366	1.428
0.1 $Z_\odot$, 1.72 C/Fe$_\odot$	0.796	1.004	1.133	1.194	1.261	1.312	1.326	1.372
$Z_\odot$, 0.58 C/Fe$_\odot$	0.490	0.659	0.801	0.864	0.840	0.858	0.877	1.045
$Z_\odot$, C/Fe$_\odot$	0.473	0.642	0.784	0.847	0.822	0.843	0.873	1.038
$Z_\odot$, 1.72 C/Fe$_\odot$	0.451	0.616	0.757	0.820	0.792	0.818	0.859	1.047
1.5 $Z_\odot$, 0.58 C/Fe$_\odot$	0.423	0.579	0.720	0.792	0.767	0.779	0.796	0.957
1.5 $Z_\odot$, C/Fe$_\odot$	0.406	0.561	0.700	0.770	0.744	0.764	0.794	0.965
1.5 $Z_\odot$, 1.72 C/Fe$_\odot$	0.389	0.539	0.673	0.736	0.708	0.737	0.779	0.991
0.1 $Z_\odot$, 0.54 Mg/Fe$_\odot$	0.811	1.023	1.154	1.224	1.292	1.343	1.369	1.437
0.1 $Z_\odot$, Mg/Fe$_\odot$	0.808	1.021	1.153	1.221	1.294	1.345	1.366	1.428
0.1 $Z_\odot$, 1.84 Mg/Fe$_\odot$	0.802	1.015	1.148	1.218	1.290	1.345	1.367	1.428
$Z_\odot$, 0.54 Mg/Fe$_\odot$	0.480	0.649	0.790	0.848	0.824	0.847	0.875	1.051
$Z_\odot$, Mg/Fe$_\odot$	0.473	0.642	0.784	0.847	0.822	0.843	0.873	1.038
$Z_\odot$, 1.84 Mg/Fe$_\odot$	0.495	0.628	0.773	0.846	0.820	0.838	0.868	1.038
1.5 $Z_\odot$, 0.54 Mg/Fe$_\odot$	0.412	0.569	0.707	0.772	0.746	0.766	0.797	0.978
1.5 $Z_\odot$, Mg/Fe$_\odot$	0.406	0.561	0.700	0.770	0.744	0.764	0.794	0.965
1.5 $Z_\odot$, 1.84 Mg/Fe$_\odot$	0.395	0.548	0.688	0.794	0.743	0.759	0.787	0.951
0.1 $Z_\odot$, 0.5 Ne/Fe$_\odot$	0.814	1.026	1.154	1.223	1.291	1.345	1.366	1.434
0.1 $Z_\odot$, Ne/Fe$_\odot$	0.808	1.021	1.153	1.221	1.294	1.345	1.366	1.428
0.1 $Z_\odot$, 2.0 Ne/Fe$_\odot$	0.796	1.011	1.147	1.216	1.289	1.347	1.370	1.428
$Z_\odot$, 0.5 Ne/Fe$_\odot$	0.482	0.651	0.791	0.846	0.824	0.848	0.875	1.053
$Z_\odot$, Ne/Fe$_\odot$	0.473	0.642	0.784	0.847	0.822	0.843	0.873	1.038
$Z_\odot$, 2.0 Ne/Fe$_\odot$	0.456	0.622	0.771	0.848	0.820	0.838	0.868	1.040
1.5 $Z_\odot$, 0.5 Ne/Fe$_\odot$	0.414	0.571	0.707	0.771	0.747	0.767	0.797	0.981
1.5 $Z_\odot$, Ne/Fe$_\odot$	0.406	0.561	0.700	0.770	0.744	0.764	0.794	0.965
1.5 $Z_\odot$, 2.0 Ne/Fe$_\odot$	0.391	0.544	0.686	0.793	0.741	0.758	0.788	0.952

Table 3.7 ΔAU, each mass and end-member composition, outer limit (MaxGH).

Composition	0.5 $M_\odot$	0.6 $M_\odot$	0.7 $M_\odot$	0.8 $M_\odot$	0.9 $M_\odot$	1.0 $M_\odot$	1.1 $M_\odot$	1.2 $M_\odot$
0.1 $Z_\odot$, 0.58 C/Fe$_\odot$	80.88	78.31	74.16	68.68	63.16	56.83	49.88	0.00[a]
0.1 $Z_\odot$, C/Fe$_\odot$	80.84	78.84	74.52	69.42	63.85	57.31	50.65	0.00
0.1 $Z_\odot$, 1.72 C/Fe$_\odot$	81.12	79.19	75.43	70.11	64.90	58.76	51.95	0.00
$Z_\odot$, 0.58 C/Fe$_\odot$	86.48	85.84	85.19	83.05	79.41	75.60	70.20	61.06
$Z_\odot$, C/Fe$_\odot$	86.90	86.22	85.46	83.25	79.43	75.39	69.82	61.17
$Z_\odot$, 1.72 C/Fe$_\odot$	87.51	86.88	86.15	83.87	79.91	75.31	69.44	60.76
1.5 $Z_\odot$, 0.58 C/Fe$_\odot$	87.38	86.86	86.33	84.88	81.48	77.68	72.62	63.85
1.5 $Z_\odot$, C/Fe$_\odot$	87.81	87.29	86.69	85.08	81.52	77.35	71.91	63.53
1.5 $Z_\odot$, 1.72 C/Fe$_\odot$	88.11	87.87	85.19	85.45	81.82	77.09	71.00	61.94

Table 3.8 Fraction (%) of time spent in CHZ_2 vs. the entire MS (carbon).

a - No orbits are continually habitable for 2 Gyr as a result of the short MS lifetime.

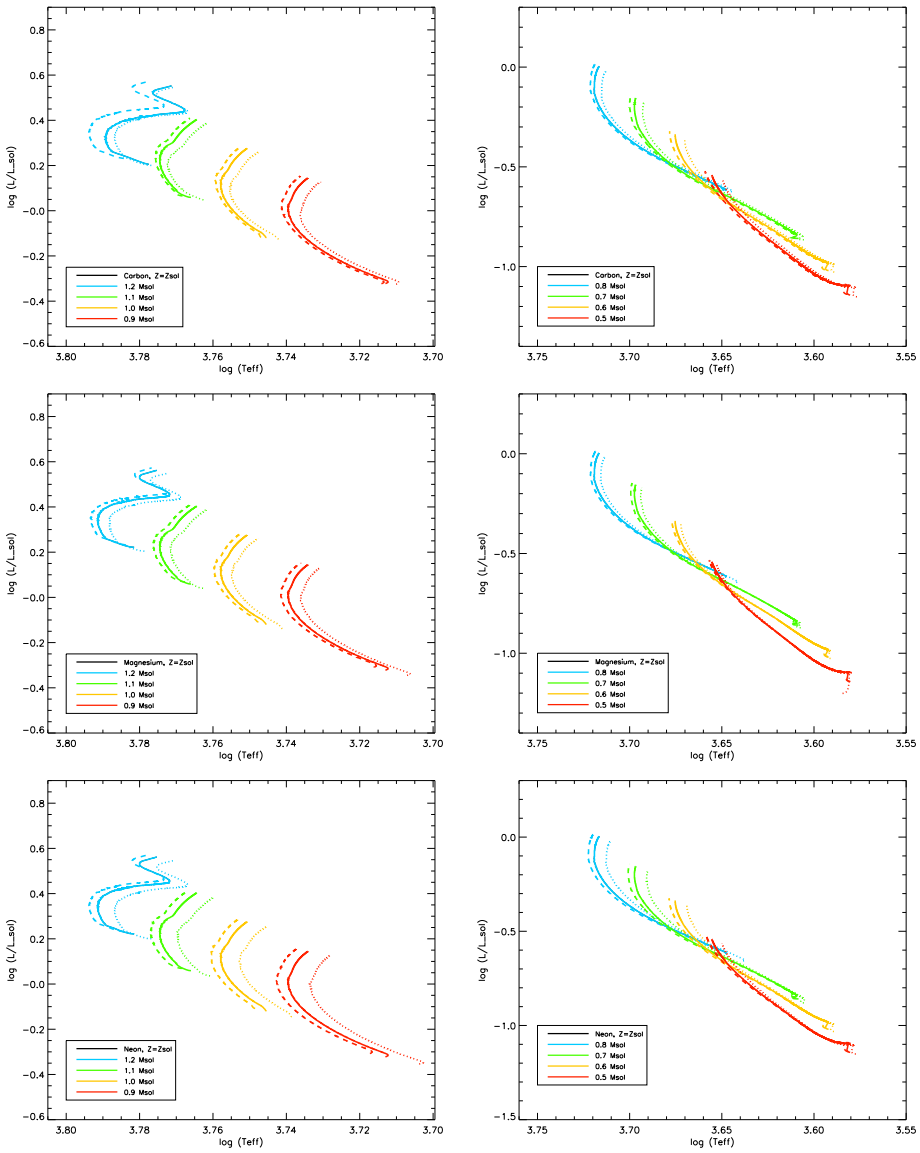

Figure 3.1 HRD, Evolutionary tracks from ZAMS to TAMS. Left column is 0.9 - 1.2 $M_\odot$, right is 0.5 - 0.8 $M_\odot$. Depleted ratios are dashed, solar value is solid, and enriched ratios are dotted. The top row is carbon (0.58 - 1.72 C/$Fe_\odot$), the middle row is magnesium (0.54 - 1.84 Mg/$Fe_\odot$), the bottom row is neon (0.5 - 2.0 Ne/$Fe_\odot$). All abundance values are held at $Z = Z_\odot$. The right-most dotted line in each row is the 0.5 $M_\odot$ star, enriched; the left-most dashed line is the 1.2 $M_\odot$ star, depleted.

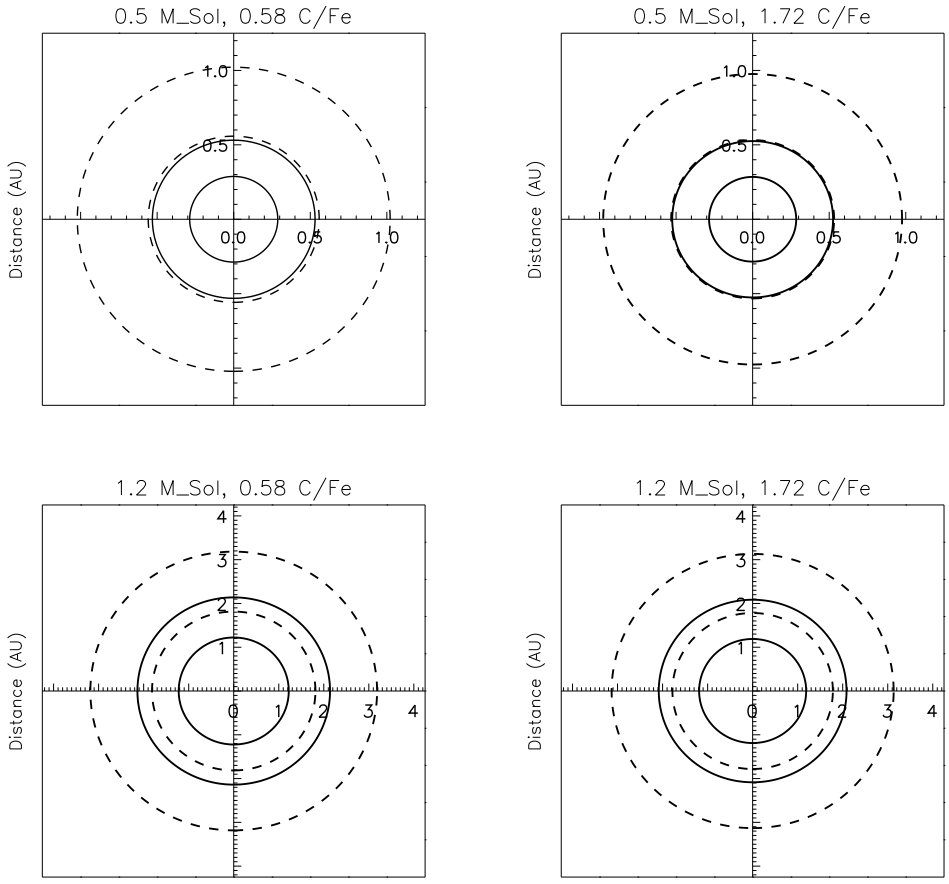

Figure 3.2 HZ Ranges: 0.5 $M_{\odot}$ (top), 1.2 $M_{\odot}$ (bottom), for 0.58 $C/Fe_{\odot}$ (left), 1.72 $C/Fe_{\odot}$ (right), at $Z_{\odot}$. HZ shown at ZAMS (solid) and TAMS (dashed). Inner/outer limits are Runaway/Maximum Greenhouse.

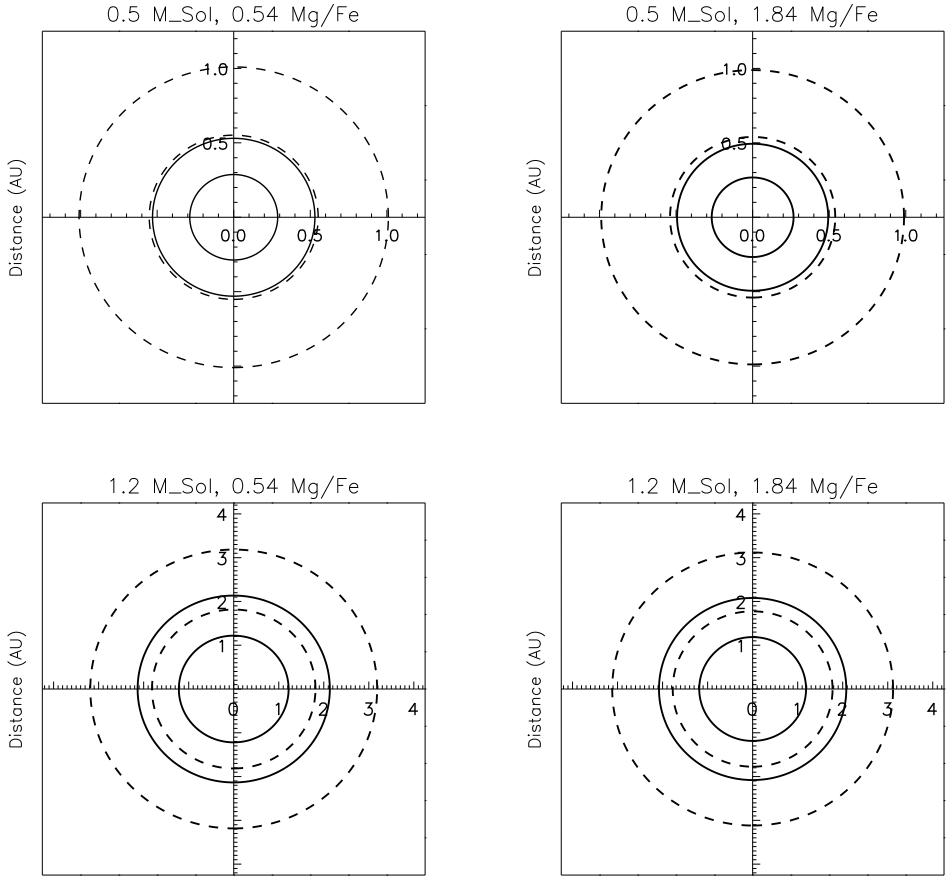

Figure 3.3 HZ Ranges: 0.5 $M_{\odot}$ (top), 1.2 $M_{\odot}$ (bottom), for 0.54 $Mg/Fe_{\odot}$ (left), 1.84 $Mg/Fe_{\odot}$ (right), at $Z_{\odot}$. HZ shown at ZAMS (solid) and TAMS (dashed). Inner/outer limits are Runaway/Maximum Greenhouse.

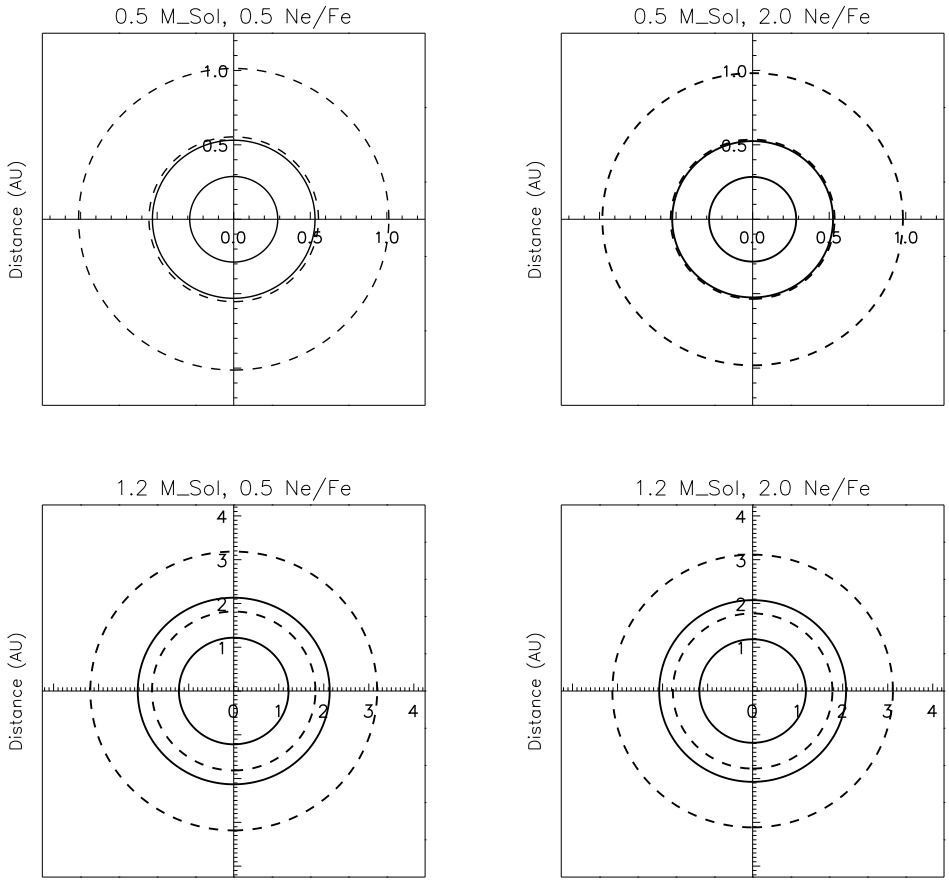

Figure 3.4 HZ Ranges: 0.5 $M_{\odot}$ (top), 1.2 $M_{\odot}$ (bottom), for 0.5 $Ne/Fe_{\odot}$ (left), 2.0 $Ne/Fe_{\odot}$ (right), at $Z_{\odot}$. HZ shown at ZAMS (solid) and TAMS (dashed). Inner/outer limits are Runaway/Maximum Greenhouse.

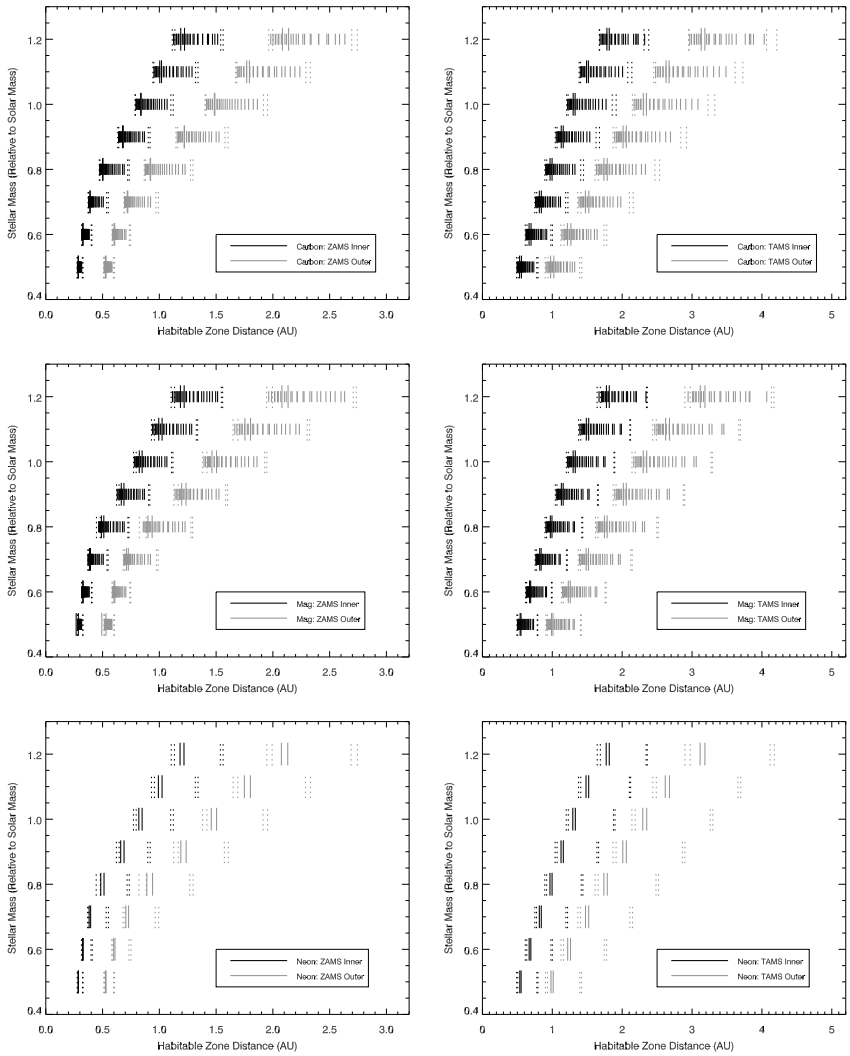

Figure 3.5 Inner and outer HZ boundaries (RGH and MaxGH) for all models at ZAMS (left) and TAMS (right). Elongated solid lines represent depleted and enriched end-member cases at $Z_{\odot}$: top row is C, middle is Mg, and bottom is Ne. The dotted lines represent end member values for each abundance value, now at end member Z values (0.1 and 1.5 $Z_{\odot}$). It is clear that compositional variation has a larger effect for the outer HZ limit, and for higher mass stars. Again, there exists a larger spreading trend for low mass stars at TAMS than at ZAMS.

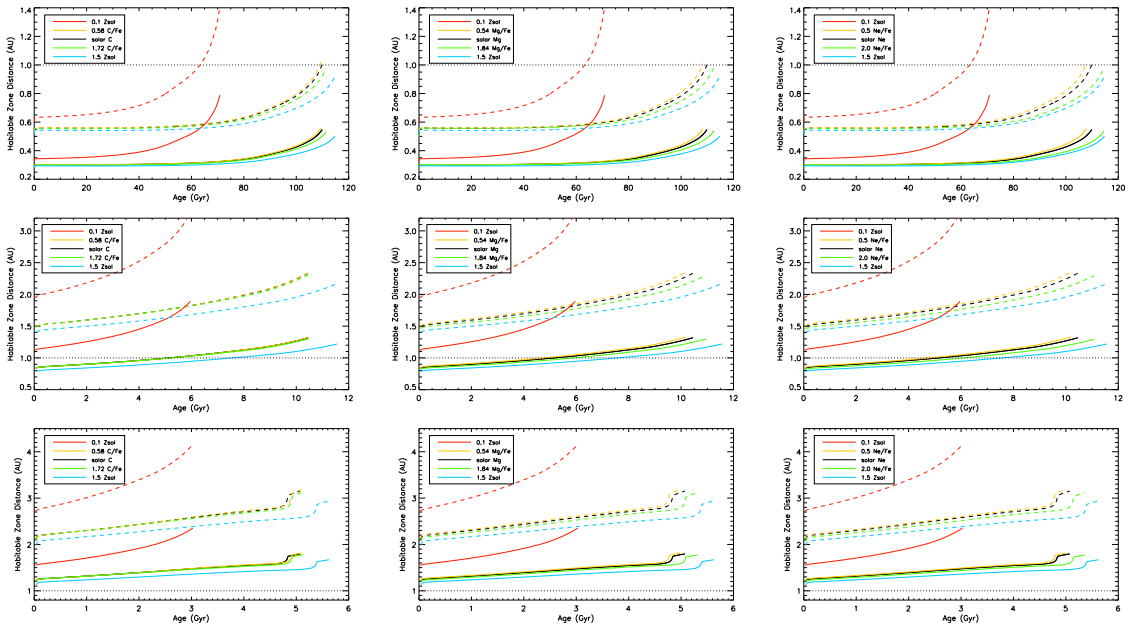

Figure 3.6 Inner (solid) and outer (dashed) edges of the HZ for 0.5 $M_{\odot}$ (top), 1 $M_{\odot}$ (middle), and 1.2 $M_{\odot}$ (bottom), for three elements: C (left), Mg (middle), and Ne (right). Each color represents an abundance value of interest: black is solar, orange is depleted (0.58 C/Fe, 0.54 Mg/Fe, 0.5 Ne/Fe), and green is enriched (1.72 C/Fe, 1.84 Mg/Fe, 2.0 Ne/Fe). Red lines represent 0.1 $Z_{\odot}$ and blue lines represent 1.5 $Z_{\odot}$. 1 AU orbit is indicated by the dotted line in each frame.

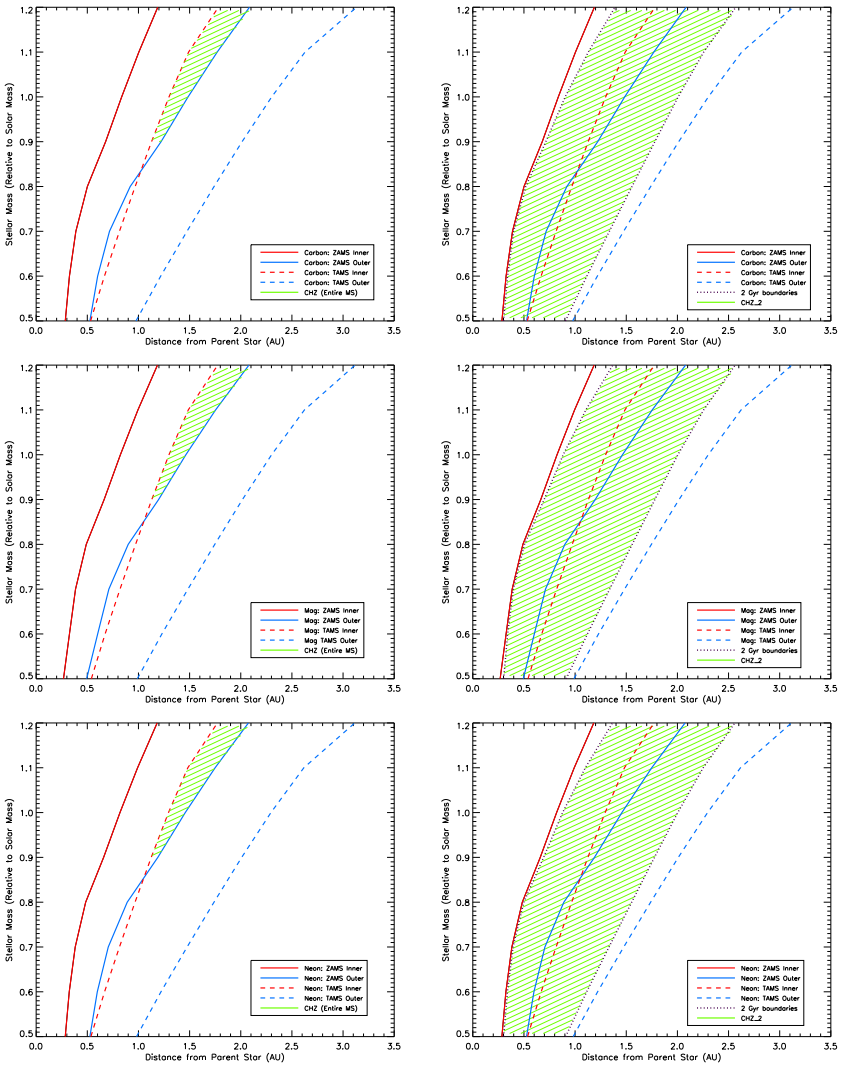

Figure 3.7 Inner (red) and outer (blue) boundaries of the HZ at the ZAMS (solid) and TAMS (dashed). For stars at each mass, at solar metallicity and enriched elemental values (C/top, Mg/middle, Ne/bottom). Left column: green shaded region is CHZ, where an orbit would remain in the HZ for star's entire MS lifetime. Right column: inner edge 2 Gyr after ZAMS and outer edge 2 Gyr before TAMS are indicated by dotted purple lines, and shaded region is the CHZ_2, where an orbiting planet would remain in the HZ for at least 2 Gyr. For conservative limits (RGH and MaxGH), low mass stars have no CHZ, and the fraction of habitable orbits in CHZ_2 is higher.

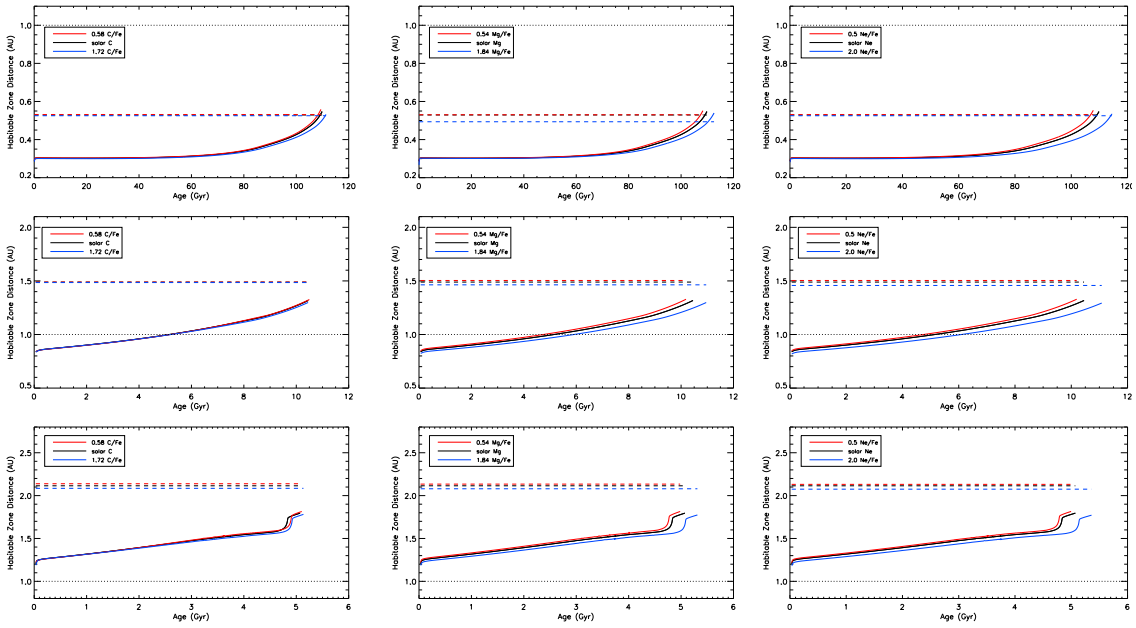

Figure 3.8 Inner (solid) and outer (dashed) edges of the HZ for 0.5 $M_{\odot}$ (top), 1 $M_{\odot}$ (middle), and 1.2 $M_{\odot}$ (bottom), for three elements: C (left), Mg (middle), and Ne (right). Each color represents an abundance value of interest: black is solar, red is depleted values (0.58 C/Fe, 0.54 Mg/Fe, 0.5 Ne/Fe), and blue is enriched values (1.72 C/Fe, 1.84 Mg/Fe, 2.0 Ne/Fe). 1 AU orbit is indicated by the light dotted line in each frame, for reference. The inner radius is Runaway Greenhouse and the outer edge is the Maximum Greenhouse, at ZAMS value.

Chapter 4

EXPANDING THE CATALOG II: STELLAR ACTIVITY

4.1 Introduction

With the ever-increasing discovery of terrestrial exoplanets, low mass and solar-type (GKM) stars have emerged as the primary targets for potentially habitable planetary systems (Newton et al., 2016). However, the habitability potential for some of these stars has been increasingly called into question. Low mass stars tend to exhibit strong stellar activity, including X-ray, UV, and magnetic fluxes, throughout their main sequence (MS) evolution. These stars can have flare activity orders of magnitude higher than anything a solar-type star is capable of producing (Kaltenegger et al., 2009); Sun-like stars also display strong activity at the Zero Age Main Sequence (ZAMS), though this generally decreases over time at a predictable rate. Regardless of the stellar type, a high level of activity interacting with a planet could inhibit the emergence of life and its subsequent evolution, even if that planet were located in the star's "habitable zone" (HZ) for billions of years.

Nonetheless, it is important that we include M-stars in our catalog, since they constitute approximately 75% of all stars in the galaxy (Hawley, 1993; Tarter et al., 2007). Low mass and solar-type stars may be advantageous targets in that they are quite common and relatively long-lived; however, due the possibility of frequent stellar eruptions (particularly near ZAMS for solar-type stars) and generally elevated activity levels, a planet may not be truly "habitable" even if it meets the criteria of the "classical" definition. The planet would necessarily be quite close to its host star, and would therefore experience high-level interactions with the stellar radiation.

When defining the classical HZ, the location is usually based largely on several important stellar surface characteristics, such as the effective temperature (T_{eff}) and luminosity (L) (Kopparapu et al., 2014). In our previous work, we modeled the evolutionary tracks for a large grid of stars, calculating T_{eff} and L at each time step, and used those values to parameterize the habitable orbital distance of a given star (Truitt et al., 2015; Truitt & Young, 2017). Though there are several other stellar characteristics that are important to consider, like the overall scaled metallicity and specific chemical composition, the general result is that more massive stars are brighter and hotter, so the associated HZ is farther out, and smaller, cooler stars yield closer-in HZs. In order to truly assess the habitability potential of a given planetary system, there are a large number of components to consider. The planets themselves present their own set of problems, such as whether there are plate tectonics or other geophysical processes, or whether there is an atmosphere, but we argue that the astrophysical factors are what we should ultimately consider first. It is essential to understand not only the physical surface characteristics and overall lifetime of the star and the corresponding location and lifetime of the HZ, but also how the associated stellar activity changes with time.

As detailed in Truitt et al. (2015); Truitt & Young (2017), we used the stellar evolution code TYCHO (Young & Arnett, 2005) to create our catalog of models, and have thus far neglected to include estimates for the heightened early mass loss that is observed in some young stars (Wood et al., 2005); measurements of stellar mass loss rates are typically used to assess how wind strength varies with activity and age for solar-type stars. Because we now include an updated prescription for rotation, mass loss and stellar activity (i.e. X-ray luminosity) over time, presented in this chapter, the code is significantly more robust and will provide an even more accurate description of the stellar evolution. The aim of this paper is to discuss what specific

changes we have incorporated into TYCHO and what we can estimate for each stellar evolutionary model. This kind of consideration is the logical next step to our earlier estimations of the HZ evolution based on the stellar mass, metallicity, and specific elemental abundance for non-rotating/non-active models. Gallet (2017) (following from Valle et al. (2014); Gallet (2016)) also studied how changes in these parameters, as well as the rotation of the star, can impact the boundaries of the HZ over time. It is important that we now also allow TYCHO to account for these changes over time, and whether a correlation exists between the stellar activity and the evolution of the HZ boundaries with increasing stellar age.

In addition to heat energy and luminosity (often visible light, 7000-4000 Å), stars also emit ultraviolet (Near-UV, 4000-1700 Å; Far-UV, 1700-912 Å; Extreme-UV (EUV), 911-200 Å) and X-ray radiation (∼100-1 Å), and sometimes produce occasional eruptions (i.e. flares or coronal mass ejections), especially in low mass stars and/or solar-type stars early-on in their evolution (France et al., 2013). X-ray emission is pervasive among low mass stars and tells us that these stars maintain active upper atmospheres throughout their lifetimes (Güdel, 2004). It is for this reason that we must also consider the stellar activity as a function of the stellar age when diagnosing a particular system's habitability potential, where "activity" can include variable UV, EUV, and X-ray radiation, magnetic fields, and ionized winds (Güdel et al., 2014). Younger stars are more likely to produce flares up to ten times more powerful than flares observed on our own Sun; conversely, older stars like the Sun only experience these intense flaring events every 100 years or so (Airapetian et al., 2017). However, stellar age is arguably one of the most difficult basic stellar quantities to measure for low mass stars (Mamajek & Hillenbrand, 2008). This is one of the reasons that we must rely on accurate stellar evolutionary models to estimate the change in stellar activity over the course of the MS evolution.

A major implication of stellar activity on planetary habitability is that this energetic radiation may cause considerable amounts of planetary atmosphere erosion (Zendejas et al., 2010). Particularly for low mass M-dwarf stars, much work has been done to attempt to quantify the impact of the stellar activity on the climate and overall habitability of planets around these stars (Shields et al., 2016). Forceful stellar flare events can cause atmospheric loss via photodissociation, and EUV emissions from the star break down molecules into their constituent atoms and ionize atmospheric gases, which ultimately allow those ions to escape to space. We are concerned particularly with those molecules that are generally considered to be important for life as we know it, including water, carbon dioxide, and methane (Segura et al., 2010). The more X-ray and EUV energy there is, the more efficient the ion escape becomes. Airapetian et al. (2017) have modeled the rate of oxygen loss in atmospheres of exoplanets orbiting active M-stars, a step toward expanding the classical definition of habitability into what they call "space weather-affected" (SWA) HZs. For aged stars with lower relative activity levels, the classical HZ will apply; however, the SWA-HZ is relevant when the host star has high X-ray and EUV emissions (i.e. greater than 7-10 times the solar average).

Atmospheric loss can profoundly affect the habitability potential of an exoplanet; the stellar wind's interaction with a planetary atmosphere can alter its overall composition, reduce the atmospheric pressure and thus limit whether a planet can maintain liquid water on the surface, and impact the efficiency of greenhouse warming (Forget, 2013; Dong et al., 2017). Understanding the evolution of a planetary atmosphere and the resulting habitability of the planetary surface requires insight into the radiation and particle environment of the host star, and recognizing that present emission levels are not necessarily indicative of past activity (Lammer et al., 2012). Other factors, including a planet's magnetic field, also play a role in the interaction between the

stellar wind and a planetary atmosphere, since a planet with little to no magnetic field is at a higher risk of atmospheric erosion. There is evidence to suggest that Mars once had a relatively substantial atmosphere, but may have been greatly diminished due to its interaction with the young solar wind (Vidotto et al., 2013).

Considering the impact of UV radiation in a planetary system is slightly delicate; if there is too much UV radiation it could potentially be hazardous to any developing life on the surface of a planet, as it can cause destruction of DNA; however, it is also known to have been a vital mechanism for the production of many important biochemical compounds on the early Earth (Buccino et al., 2006). Some groups (e.g. Guo et al. (2010), following from Buccino et al. (2007)) have considered UV habitable zones (UV-HZs) around stars, and how they relate to the classical, liquid-water HZ. They find that the UV-HZs are essentially identical to the classical HZ for stars with T_{eff} from ∼4600-7100 K (FGK-stars); for host stars with T_{eff} lower than 4600 (KM-stars), the UV-HZs are closer than the classical HZ, which we might interpret as "inadequate" UV radiation in the HZ. For host stars with T_{eff} higher than 7100 K, the UV-HZs are beyond the classical HZ limit, meaning there would be too much UV in the classical HZ, and we might expect DNA to break down at this distance.

The recent discovery of seven terrestrial planets in the TRAPPIST-1 system highlights the importance of understanding the impact of stellar activity in the circumstellar environment. UV flares from M-stars are much more frequent and intense than solar-type flares (O'Malley-James & Kaltenegger, 2017). A high level of activity may not be favorable for the planets that reside in the close-in HZ of the TRAPPIST-1 system; furthermore, high X-ray/EUV activity could cause significant atmospheric loss, as discussed previously. We shouldn't necessarily discount these planets as potentially fruitful places for life, but it is important to consider the many aspects that contribute to the complex interplay between stellar environment and orbiting planets.

Activity in low mass stars is difficult to constrain observationally. Shkolnik & Barman (2014) report a wide range of observed emission levels (1-2 orders of magnitude) of M-stars at every age. However, the HAZMAT project they have developed will be useful for modeling the evolution of planetary atmospheres based on the EUV activity of the host star. Additionally, observations of coronal processes for the Sun and solar-type stars have provided enough data to develop believable models for stellar activity over a wide range of ages and stellar parameters (e.g. Testa et al. (2015)).

Solar and late-type stars emit X-rays at coronal temperatures of several million degrees Kelvin (Vaiana et al., 1981). The most luminous X-ray sources of single low mass stars are from the youngest objects (Telleschi et al., 2005, 2007), while older stars typically exhibit much lower values (Feigelson et al., 2004). Chromospheric activity, and coronal X-ray emission, is thought to be driven by the stellar magnetic dynamo, which is in turn thought to be produced by differential rotation deep in the convective envelope of a star (Parker, 1955; Kraft, 1967; Pace & Pasquini, 2004)). We also know that rotational velocity and activity both decrease over time due to braking by magnetized stellar wind (Skumanich, 1972; Simon et al., 1985), a well-known age-activity relationship observed in solar-type stars (Parker, 1970). This co-evolution of magnetic activity provides an empirical foundation to the theory of magnetic dynamos. Preibisch & Feigelson (2005) studied the age-activity relation in the pre-MS regime; they find that over long timescales, the X-ray luminosity decay law for stars in the 0.5-1.2 $M_{\odot}$ mass range (our original grid) is quite rapid, though the magnetic activity history for M-stars (0.1-0.45 $M_{\odot}$) is significantly different. Only a mild decrease in X-ray luminosity over time is seen in the first 100 Myr, though X-ray emission does decay over long timescales for these stars on the MS. Overall, the activity-age decay is strong across the entire history of solar-type stars but is not linked to rotational deceleration at early ages.

Cooler, M-type stars are generally thought to lose mass throughout their entire lifetimes via magnetized stellar winds (Vidotto, 2016). Even though these winds do not remove large amounts of mass, they do remove angular momentum from the star over time. As the angular momentum transport changes, so do the stellar interior properties. The winds are thus important mechanisms that help to govern the stellar rotation and overall activity levels versus age. Because the magnetized stellar wind is also thought to be driven by the stellar dynamo (e.g. Cranmer & Saar (2011)), the stellar rotation, wind, and activity basically exist as a feedback loop, all decreasing with age (e.g. Wright et al. (2011)). Barnes & Kim (2010) have also demonstrated that open cluster rotation period data can be used for an empirical formulation of angular momentum loss from cool stars on the MS.

Observational evidence (e.g. Güdel (1997b)) has shown that ZAMS solar-type stars can rotate over 10 times faster than the current Sun, which implies that young solar-type stars have strong magnetic dynamos and correspondingly high energy emissions (Ribas et al., 2005). The observed instantaneous rotational velocity of a star can provide us with important clues about its formation and internal structure (Wolff & Simon, 1997). Differences in the surface rotation over time may be used to estimate the evolutionary time scales for internal angular momentum exchange, and even how diffusion and mixing in the stellar interior may change the chemical composition in the surface layers of a star (Pinsonneault et al., 1990).

Understanding how low mass and solar-type stars change over the course of their evolution is one of the central motivations of this work. We know that the Sun has experienced periods of stronger magnetic activity in the past, and its magnetic activity has been slowing for its entire MS evolution (Güdel, 2007). Moreover, from theoretical models and observations of solar analogs, we know that the effective solar luminosity was approximately 30% lower at ZAMS, prompting the "Faint Young Sun" paradox

(e.g. Kasting & Grinspoon (1991)). The standard solar models predict a much cooler early Earth than the actual evidence suggests; Geiss & Bochsler (1991) offers a potential solution to this discrepancy, citing a much higher mass loss rate for the young Sun, on average 10 times higher than present values. This long-standing point of contention and investigation for the evolutionary processes of the Sun, and how it has directly affected habitability on the early Earth (as well as Venus and Mars), demonstrates why it is essential that we understand how stellar activity changes over time for any given stellar system of interest. If we can understand the kind of impact that changes in the solar activity may have had on the early Earth, that knowledge can be translated into understanding the activity versus age relationships for other Sun-like stars that may host potentially habitable Earth-like exoplanets.

4.2 Methodology

4.2.1 A Minimalist Coupled Model to Estimate Stellar Activity

The connection between rotation, magnetic fields, and stellar activity has been fairly well-established observationally, but a time-dependent theoretical model that is able to accurately explain and describe those observational trends, as well as the simultaneous evolution of X-ray luminosity, rotation, magnetic fields, and mass loss has unfortunately been mostly absent. Additionally, since a star's magnetic field is the energy source for both the X-ray emission and the stellar wind, it would not be truly representative of the real physics involved if the model were to separately consider the evolution of L_x and rotation; a coupled solution would therefore provide the most robust description of X-ray activity and rotational evolution of a star. To that end, Blackman & Owen (2016) (hereafter BO16) present a model to estimate the time evolution of the stellar quantities of interest; however, they focus on solar-type

stars younger than the Sun, so this update to the code will eventually need to be further developed and tested if we want to be able to accurately estimate the changes in stellar activity over the entire MS lifetime, for both solar-type and M-dwarf stars.

The time-dependent solutions we have obtained do generally agree with observed trends discussed in BO16 including the approximate scaling of the mass loss rate with X-ray luminosity (for their minimalist model, they set them equal), where

$$l_x \equiv \frac{L_x}{L_{x_\odot}} \sim -\frac{dm}{dt} \tag{4.1}$$

and

$$\frac{dm}{dt} \equiv \frac{(dM/dt)}{(dM_\odot\ /dt)} \tag{4.2}$$

where $_\odot$ denotes solar values, L_x is X-ray luminosity, and M is mass. For the average solar X-ray luminosity and magnetic properties, they reference Aschwanden (2004), where $L_{x_\odot} = 6{\times}10^{-7} L_\odot$, and where $L_\odot = 4{\times}10^{33}$ erg/s. The average solar coronal X-ray temperature is given as $T_{x_\odot} = 1.5{\times}10^6$ K. Though the model has obvious limitations, in that it is based on a minimalist theoretical framework, it is still quite useful as we try to predict the age-activity relationships for solar-type stars in our original grid, especially given the previous lack of any sort of method to calculate these important stellar properties.

4.2.2 Updates to TYCHO (2016-2017)

As discussed in chapters 2 and 3, TYCHO is a 1D stellar evolution code with a hydrodynamic formulation of the stellar evolution equations. We previously utilized a 177-element network terminating at ^{74}Ge throughout the evolution, though we have recently increased the network to 522 components (elements and isotopes) which offers a more robust consideration of the overall stellar evolution.

We have also recently implemented the BO16 model into TYCHO in order to estimate the evolution of stellar activity as a function of age for a small grid of solar-type stars at early ages. We discuss the different components of stellar activity, how each of them changes with time, and how our models compare with observations and expected trends. We have only tested this model in TYCHO with solar mass stars, but we want to do further testing to see whether this would produce believable output regarding low mass stars, since those are the types of stars that are prone to much higher levels of stellar activity throughout their lifetimes. TYCHO now produces relatively accurate estimates compared to literature values for X-ray luminosity, coronal temperatures, convective turnover time, etc. in the early evolution; however, in the future, we may want to consider a supplemental formula for calculations of the evolution beyond solar age.

We have followed the prescriptions outlined in BO16 to allow TYCHO to perform calculations for the following: the radial stellar wind flux; the radial magnetic field; the coronal temperature and its relation to the X-ray luminosity and flux; the associated mass loss estimates; and the time-evolution of the angular momentum (i.e. the rate at which a given star will "spin-down"). All of these calculations working in tandem provide an estimate for how the X-ray luminosity activity changes with age. For further testing, we have also compared our new results from implementing the BO16 formulations with other theoretical models for loss of mass and angular momentum, as well as X-ray activity with time, including Güdel (1997b); Landin et al. (2010); Reiners & Mohanty (2012); we also compare our results with Johnstone & Güdel (2015), who have derived a general scaling law between coronal temperature and the X-ray activity based on observations of X-ray emission for low mass MS stars. Finally, we test the utility of our updated code by comparing with actual observations of the X-ray luminosity and rotational velocities of nearby stars (G-type stars within

30 pc) which we have taken from the SIMBAD database (Wenger et al., 2000).

From BO16, the *normalized* surface radial magnetic field magnitude is

$$b_r = g_L(t) \times \frac{B_{r\star}(t)}{B_{r_\odot}} = g_L(t) \left(\frac{s}{s_\odot} \right)^{1/6} \left(\frac{1 + s_\odot \ Ro_\odot}{1 + sRo} \right)^{1/2} \tag{4.3}$$

where

$$g_L(t) = (1.4 - 0.4t)^{\frac{\lambda - 1}{4}} \tag{4.4}$$

for t in units of solar age and and $0 \leq \lambda \leq 0.33$, and where $s = 8.3$ is a fixed shear value which we take from BO16, Ro is the Rossby number given by $Ro = 2\pi/(\Omega\tau_c)$ where τ_c is the local convective turnover time and $Ro_\odot = 2$, and $B_{r\star}(t)$ is the surface radial magnetic field with $B_{r_\odot} = 2$ G. We get $\tau_c = 1.6 H_p / v_{\rm conv}$ by using the existing TYCHO stellar structure calculations, and we compute Ro using $\Omega_{\rm surf}$, which is a surface angular velocity that accounts for the magnetic spin-down over time.

BO16 also derive the normalized X-ray luminosity (Eq. 4.1) as a function of the magnetic field strength,

$$l_x = b_r^{\frac{4}{1-\lambda}} \tag{4.5}$$

and how it relates to the normalized coronal temperature $\tilde{T}_0 = T_0/(3 \times 10^6 \text{ K})$ and the mass loss rate through

$$l_x \simeq Exp \left[ln(T_0) + 7.8 \frac{m_\star}{r_\star \tilde{T}_0} \left(\frac{\tilde{T}_0}{\tilde{T}_{0_\odot}} - 1 \right) \right] \simeq \dot{m} \tag{4.6}$$

where $\tilde{T}_{0_\odot} = 0.5$ and $m_\star$ and $r_\star$ are the mass and radius, respectively, normalized to solar values and taken from TYCHO output. We use our calculated $\tilde{T}_0$ value to solve for the coronal pressure, given by

$$p_0 = \frac{m_\star}{r_\star^2} 1.6 \tilde{\Theta} \tilde{T}_0^{\frac{29}{12}} + \frac{m_\star}{r_\star^2} 0.75 \tilde{T}_0^{\frac{13}{6}} e^{3.9 \frac{m_\star}{r_\star}(1 - \frac{1}{\tilde{T}_0})} + \frac{m_\star}{r_\star^2} 2.34 \tilde{T}_0^{\frac{7}{6}} e^{3.9 \frac{m_\star}{r_\star}(1 - \frac{1}{\tilde{T}_0})} \tag{4.7}$$

where the solid angle "covering fraction" $\tilde{\Theta}$ has its upper limit defined as 0.1.

We calculate the sound speed for the base of the corona, a_0, using

$$a_0 = \left(\frac{2 k_B T_0}{m_H} \right)^{1/2} \tag{4.8}$$

where k_B is the Boltzmann constant and m_H is the mass of hydrogen. We then compute the radial Alfven speed,

$$u_A = \frac{B_{r\star}}{\sqrt{4\pi\rho}} \tag{4.9}$$

where $\rho = \sqrt{p_0 / a_0^2}$, and we finally get the change in angular velocity over time due to stellar spin-down from magnetic wind-driven angular momentum loss,

$$\frac{d\Omega}{dt} = -\frac{q\,\Omega_{\rm surf}\,B_{r\star}^2\,R^2}{0.059\,M\,u_A} \tag{4.10}$$

where q is an inertial parameter that we set to 0.8 to account for drag on the outer spin of the star from angular momentum transport within the star. At each timestep Δt, we change the surface angular velocity by an amount

$$\Omega_{\rm surf,new} = \Omega_{\rm surf} + \frac{d\Omega}{dt} \times \Delta t \tag{4.11}$$

We compare our initial TYCHO calculations with values from Landin et al. (2010); they discuss the theoretical estimates for the local (τ_c) and global (τ_g) convective turnover times for rotating pre-MS solar-type stars, which in turn are compared with previous values from the literature (Kim & Demarque, 1996). Additionally, they investigate the dependence of the convective turnover time on things like the rotation, which can be used to calculate the Rossby number (R_0), which is related to the magnetic activity strength and shows an observational correlation with stellar activity for MS stars.

Figure 4.1 shows a comparison of our new TYCHO calculations with a theoretical model introduced in Landin et al. (2010), for the entire MS evolution. The upper

left is a comparison for τ_c, the upper right is τ_g, the bottom left is for the Rossby "dynamo" number ($1/Ro^2$), and the bottom right is for the convective velocity. We find that we are able to satisfactorily replicate these figures from their original paper. We created the model that we use to compare with each of the theoretical lines by not only setting the mass and composition for the model to be solar, but we also checked that we were starting with an initial (pre-MS) Ω-value such that we would reach the current Sun's angular velocity value ($\sim 3\times10^{-6}$ s^{-1}) at solar age.

We have simulated a small grid of models to represent the variation we might expect in rotational velocity for solar-type stars. We have created a grid of 9 rotating models, all for solar mass, at three different initial Ω-values, representing angular velocity values at solar age that range between $\sim$ 0.8-1.4 times the current solar angular velocity. At each of the three angular velocity values, we perform calculations to create models for 0.5, 1, and 1.5 times the overall scaled solar metallicity value ($Z_\odot$). Figure 4.2 is an HR-diagram for the models in our parameter space, demonstrating the spread in luminosity and temperature that we observe in this grid. Red lines represent initial angular velocity values that correspond to $\Omega/\Omega_\odot = 1$ at solar age; orange lines represent initial Ω-values that correspond to $\Omega/\Omega_\odot \sim 0.8$; blue lines represent $\Omega/\Omega_\odot \sim 1.4$. Dashed lines are for 0.5 $Z_\odot$, solid lines are for 1.0 $Z_\odot$, and dashed-dotted lines are for 1.5 $Z_\odot$. It is clear that both parameters contribute to the overall evolution, though the scaled metallicity has a somewhat larger effect.

4.3 Discussion of Results

We find that the new additions to the code represent observed trends of stellar activity fairly well; specifically, if we consider the magnetic activity over time (Figure 4.3), the X-ray luminosity, which correlates to mass loss, over time (Figure 4.4), or the angular velocity (Ω) over time (Figure 4.5), our model fits relatively well with

the theoretically expected behavior. It makes sense that we see the same trend between B_r and Ω, since theory says the dynamo will be linear with the magnetic field (Vidotto, 2014), which also implies that the X-ray luminosity scales with the magnetic energy density, $L_x \propto B^2$ (Gregory, 2016) (Figure 4.6). However, it is clear from Equation 4.7 that l_x depends more strongly on b_r in BO16.

While Figures 4.3 and 4.4 only show comparisons between TYCHO results and BO16, Figure 4.5 includes considerations for changes in Ω over time from two other studies (Landin et al., 2010; Reiners & Mohanty, 2012). The model from Landin et al. (2010) (orange line) emerges from a consideration of differential rotation and convective movement, as well as magnetic effects throughout the stellar structure. Reiners & Mohanty (2012) (blue line) derived a corrected magnetic braking law based on the relationship between stellar rotation and the magnetic field strength, not only the magnetic flux; however, this model differs from the other two prescriptions in that the angular momentum is significantly higher than solar value at solar age. BO16 indicated by black line, and the result of this work (TYCHO) is indicated by the red line. It is clear that our model is consistent with Landin et al. (2010) and BO16.

Also of note, Johnstone & Güdel (2015) (JG15) demonstrate a strong correlation between coronal temperature and X-ray surface flux for MS stars with masses between $\sim$ 0.2 and $\sim$1.1 $M_\odot$, given by T_0=0.11 $F_x^{0.26}$. They find that coronal temperature actually tends to scale much more closely with X-ray flux than with X-ray luminosity (L_X) or X-ray to bolometric luminosity ratio ($R_x = L_x/L_{bol}$). Figure 4.7 shows the empirically-derived line from JG15 (black) for coronal temperature (T_0) versus the X-ray flux (F_x), with our model in red. As expected, we show nearly-matching coronal temperatures for both models at solar value (yellow dot). TYCHO has not previously been formatted to calculate the coronal temperature of stars, so this update is a significant step toward a more complete description of stellar evolution.

In order to test the utility of the updated code, it is important that we compare TYCHO results with observational data, particularly for solar-type stars near solar age. There is a well-established precedent for comparing the observations of X-ray luminosity with the stellar rotation rate (Pallavicini et al., 1981). We look at stars near solar L_{bol} (with X-ray luminosity measurements) from the ROSAT database, using rotational velocity ($\mathrm{v}\, sin(i)$) measurements from the SIMBAD database for stars of interest. Using this data, we match the rotational velocity of any one of our model stars with the observed value of a particular star, and we find whether the l_x we calculate for that model is representative of real stars.

We can directly compare our results with observational X-ray luminosity data from ROSAT. Our l_x values relate to the R_x values from ROSAT by:

$$l_x = \frac{R_x \times L_{bol\star}}{(6 \times 10^{-7}) L_{bol_\odot}} \tag{4.12}$$

Our sample consists of G-type stars near solar age (selected by their bolometric luminosity) within 30 pc of the Sun, compiled by Hinkel et al. (2017) for the CATSUP database. We convert the given R_x measurements to l_x to match our calculation from TYCHO. In Figure 4.8, we compare X-ray luminosity vs. rotational velocity observations with our TYCHO models. We over-plot tracks for three different initial angular velocity values (red produces $\Omega/\Omega_\odot \sim 1$ (solar), orange produces $\Omega/\Omega_\odot \sim 0.8$, and blue produces $\Omega/\Omega_\odot \sim 1.4$) onto the ROSAT stars (black circles). An additional observational best-fit line is given by Güdel (1997b) (dashed black line), and we also include model results from BO16 (solid black line), which all appear to be roughly consistent with the ROSAT data.

Figure 4.9 again shows rotational velocity plotted against X-ray luminosity values, zoomed in so we can further appreciate the spread in values that our grid provides. Though the nine models in our grid are all for solar mass stars, they show a significant

variability in their location in this parameter space. This demonstrates why it is not only important to consider the initial mass and composition of a star, but also the evolutionary history of the stellar activity. In this figure, orange represents the "slow rotator" model, the case with the lowest initial angular velocity (note that stellar evolution proceeds from right to left). The orange star has a smaller maximum speed than the other models (red, faster; blue, fastest); since all of the models follow the same trend of "spinning-down" with time, at a given stellar age the orange star will have the lowest speed. With a smaller starting rotation, the orange star also appears to have a higher speed for a given luminosity, or conversely a smaller luminosity for a given speed. Since l_x increases over time while angular velocity decreases, the faster blue star will have a larger X-ray luminosity value when it reaches a speed that the slower orange star reached earlier in its evolution. Therefore at a given rotational velocity value, orange has the smallest l_x, while blue has the largest.

Finally, Figure 4.10 again plots X-ray luminosity (l_x) against the rotational velocity (v $sin(i)$). What we aim to show here is that TYCHO's calculations are robust, and we do have the ability to provide accurate predictions of stellar activity values, at least for solar-type stars. Shown by the large squares are angular velocity (Ω) values at solar age for three models at solar mass and $Z_\odot$. Red is for $\Omega/\Omega_\odot \sim 1$, orange is $\Omega/\Omega_\odot \sim 0.8$, and blue is $\Omega/\Omega_\odot \sim 1.4$. The smaller squares are a subset of data points taken from the ROSAT dataset, selected for stars with rotational velocities equal to those of our three rotating solar models. The circles are the average of the observed values, with the standard deviation given by the error bars. Although our models are systematically low relative to the observed l_x values, they are all within 1σ. Even with the observed spread in the X-ray luminosity, our models fit reasonably well with the measured activity levels of solar-analog stars.

4.4 Conclusions

We have discussed the recent updates we have made to the stellar evolution code TYCHO, in order to estimate the evolution of stellar activity as a function of age for a small grid of solar-type stars at early ages. We find that changing both the overall scaled metallicity values as well as the initial angular velocity of the star can significantly impact the stellar evolution. Though this implementation of the BO16 minimalist coupled evolution model has only been tested for solar mass stars, we have discussed how the different components of stellar activity (i.e. mass loss, rotation, X-ray luminosity, and magnetic activity) change with time, and how our new grid of rotating models compare with observations and expected theoretical trends.

We have compared our new results with the original BO16 paper from which we derive the prescriptions for updated mass loss and rotation considerations; we also have compared our results to several other theoretical models (detailed above) and a dataset of observational X-ray luminosity values. We confirm that our calculations fit with observed trends of activity evolution throughout time (e.g. we observe a rotational spin-down due to wind-driven magnetic braking processes) and we also demonstrate that TYCHO has the ability to match both X-ray luminosity and rotational velocity values of solar-type stars at roughly solar age.

One shortcoming of this approach is built-in to the nature of the stellar activity prescriptions we use from BO16, in that by definition, it is a minimalist model and many assumptions must be made. Indeed, this model may only have predictive power for a very specific subset of stars that are like our own Sun (though we do show that at least some consideration of initial Ω-value and chemical composition can be made). Ultimately, we would like to do further testing against observational data to see whether TYCHO will possibly be able to produce believable values for lower-mass

stars, since those stars are prone to higher levels of stellar activity throughout their lifetimes. In order for any real conclusions to be made about a given planetary system's habitability, it is important that we are able to accurately model the changes in stellar activity over time; the circumstellar environment is an important factor in determining whether a planet could be considered habitable. We hope to provide a robust model for the expected activity over time for a variety of stars, and investigate how different levels of activity would impact the location of the HZ.

We have made use of the ROSAT Data Archive of the Max-Planck-Institut für Extraterrestrische Physik (MPE) at Garching, Germany.

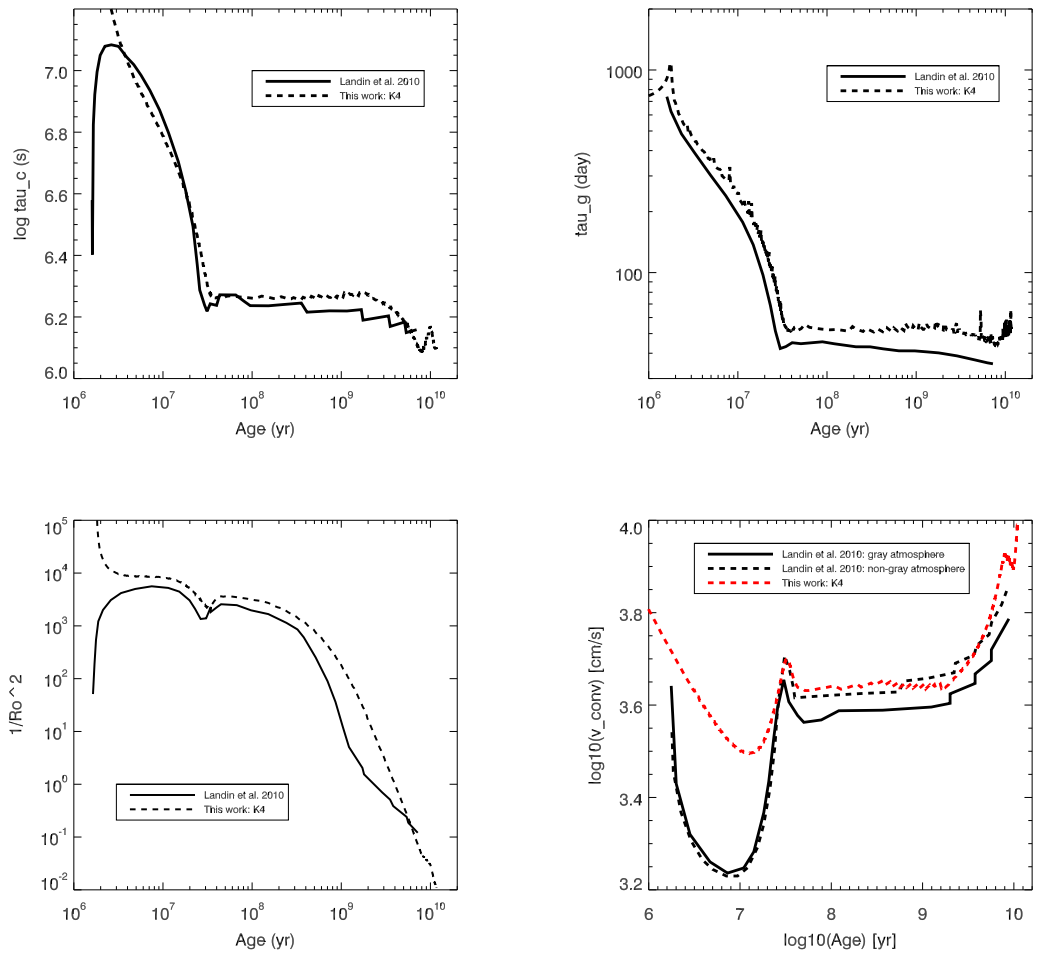

Figure 4.1 Comparison of new TYCHO calculations with figures from Landin et al. (2010), for each property of interest over time; upper left is τ_c, upper right is τ_g, bottom left is the Rossby "dynamo" number, bottom right is convective velocity.

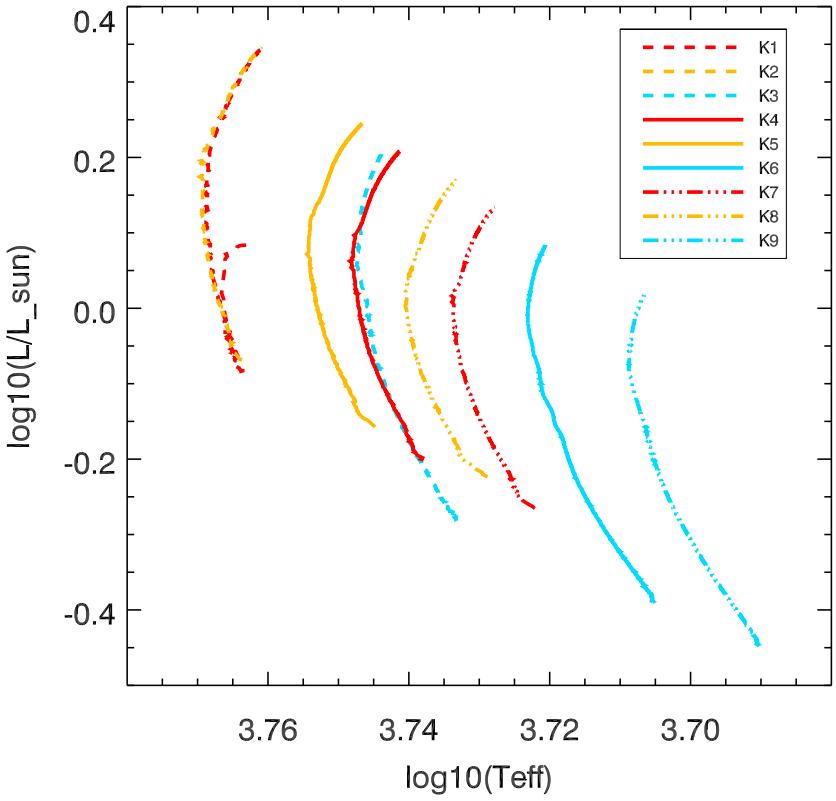

Figure 4.2 HR-diagram for all 9 models in our parameter space. Red lines represent initial angular velocity values that correspond to $\Omega/\Omega_{\odot} \sim 1$ at solar age; orange lines represent $\Omega/\Omega_{\odot} \sim 0.8$; blue lines represent $\Omega/\Omega_{\odot} \sim 1.4$. Dashed lines are for 0.5 $Z_{\odot}$, solid lines are for 1.0 $Z_{\odot}$, and dashed-dotted lines are for 1.5 $Z_{\odot}$.

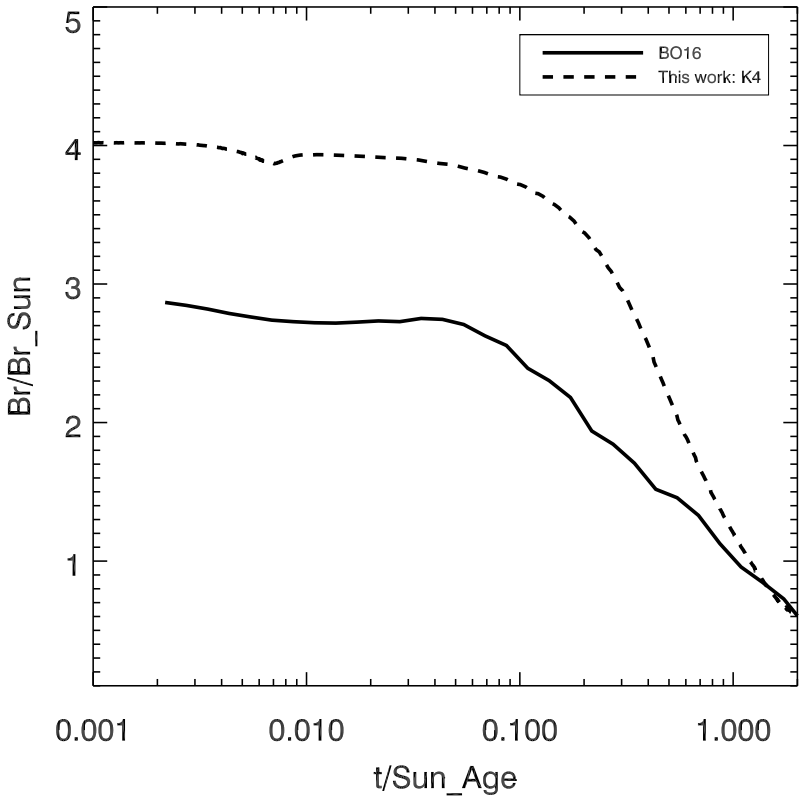

Figure 4.3 Comparison between our work with TYCHO (dashed) and the original BO16 model (solid), for the radial magnetic field value over time; we find that our estimates from TYCHO are a bit high in the early evolution, but the magnetic activity drops off over time and coincides with the BO16 value near solar.

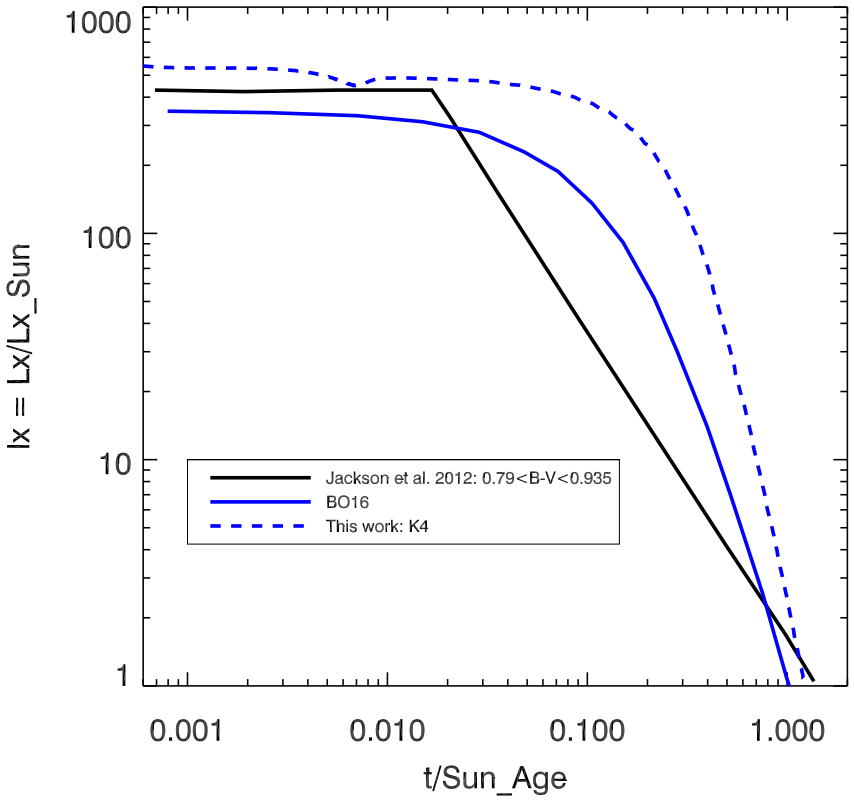

Figure 4.4 Comparison between our work with TYCHO (blue dashed), the original BO16 model (blue solid), and a best-fit line of observational data points from Jackson et al. (2012). This is for l_x vs. time. We find that our values from TYCHO fit the expected trends well (i.e. coronal activity and X-ray emissions are observed to decrease with time), though our precise values do not match until around solar age.

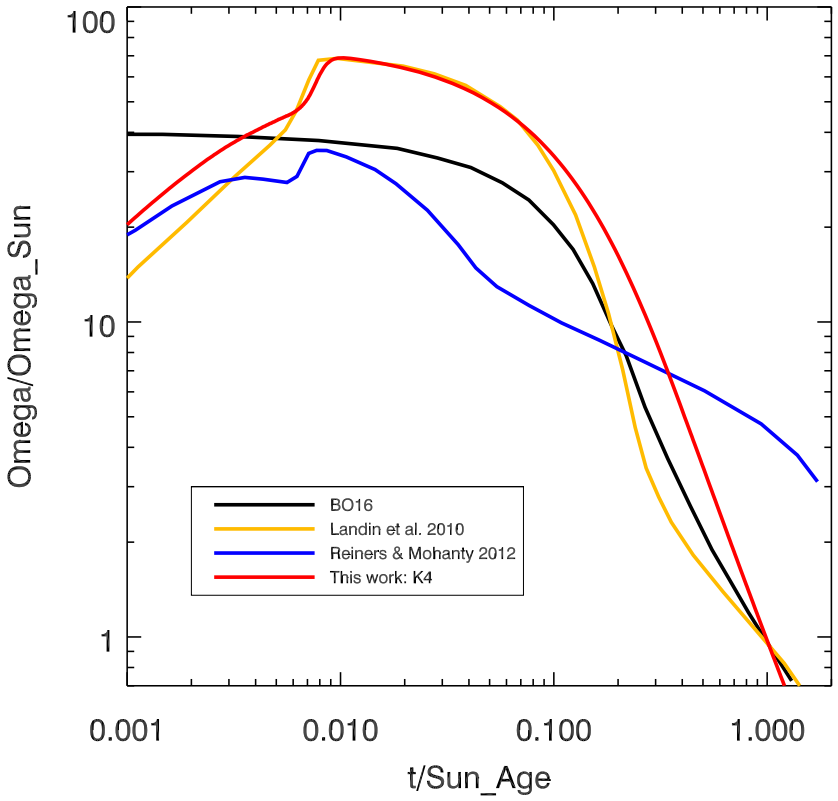

Figure 4.5 Four considerations for modeling angular velocity (Ω) over time, represented by Landin et al. (2010) (orange), Reiners & Mohanty (2012) (blue), and Blackman & Owen (2016) (black). The result of this work (TYCHO) is indicated by the red line, and fits closely with the expected trend that Ω decreases with age.

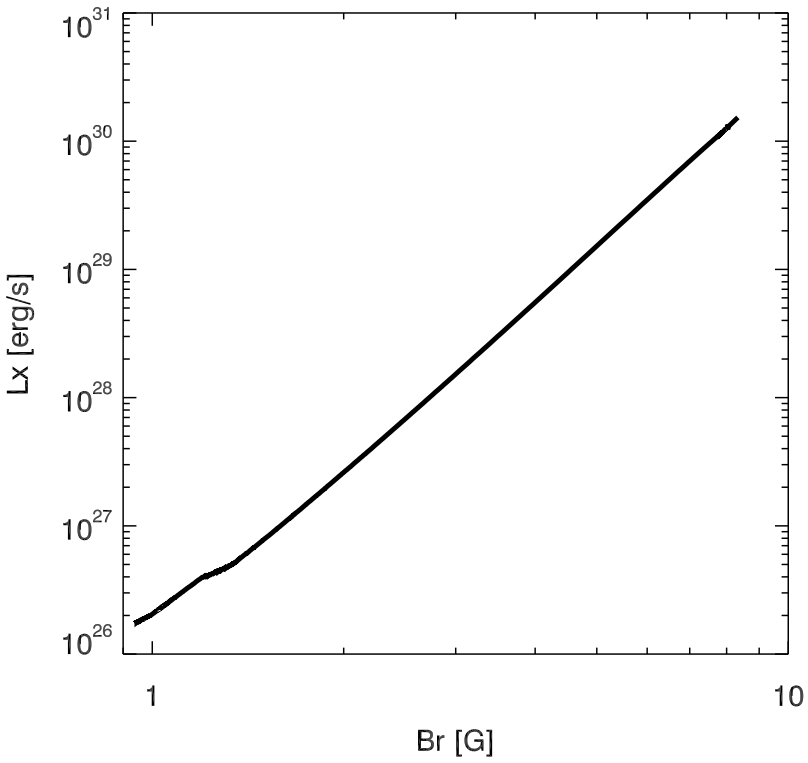

Figure 4.6 We show that our L_x values are proportional to the radial magnetic field (a proxy for the overall magnetic energy density) as ${B_r}^4$, which is higher than the empirical value of ${B_r}^2$ (Gregory, 2016), though our values follow from BO16.

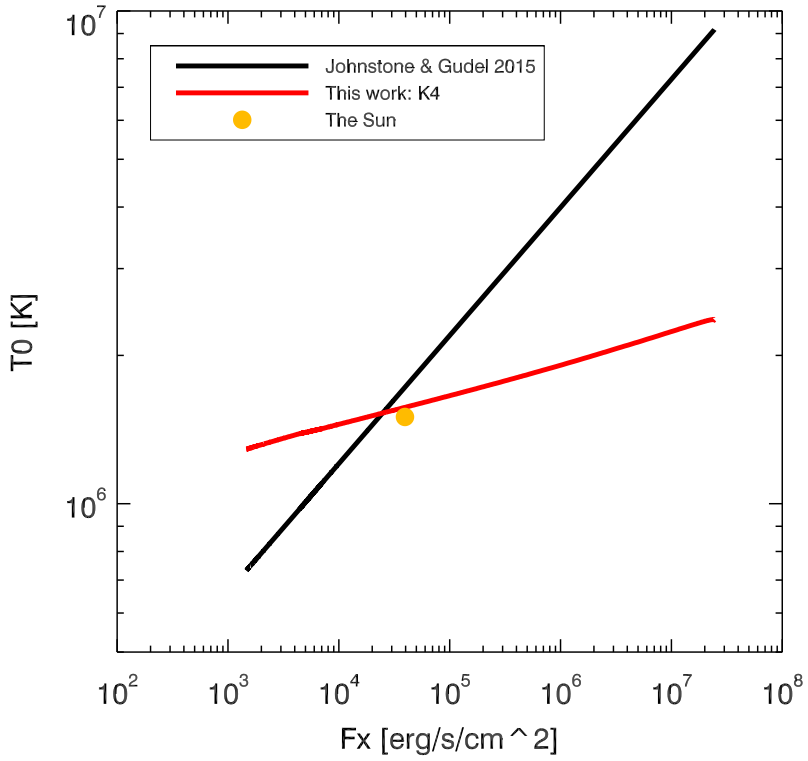

Figure 4.7 Coronal temperature (T_0) versus X-ray flux (F_x) for JG15 (black) and our results from TYCHO (red). It is clear that the BO16 prescriptions we use are based on normalizations to the Sun; we show close values with JG15 at solar (yellow dot).

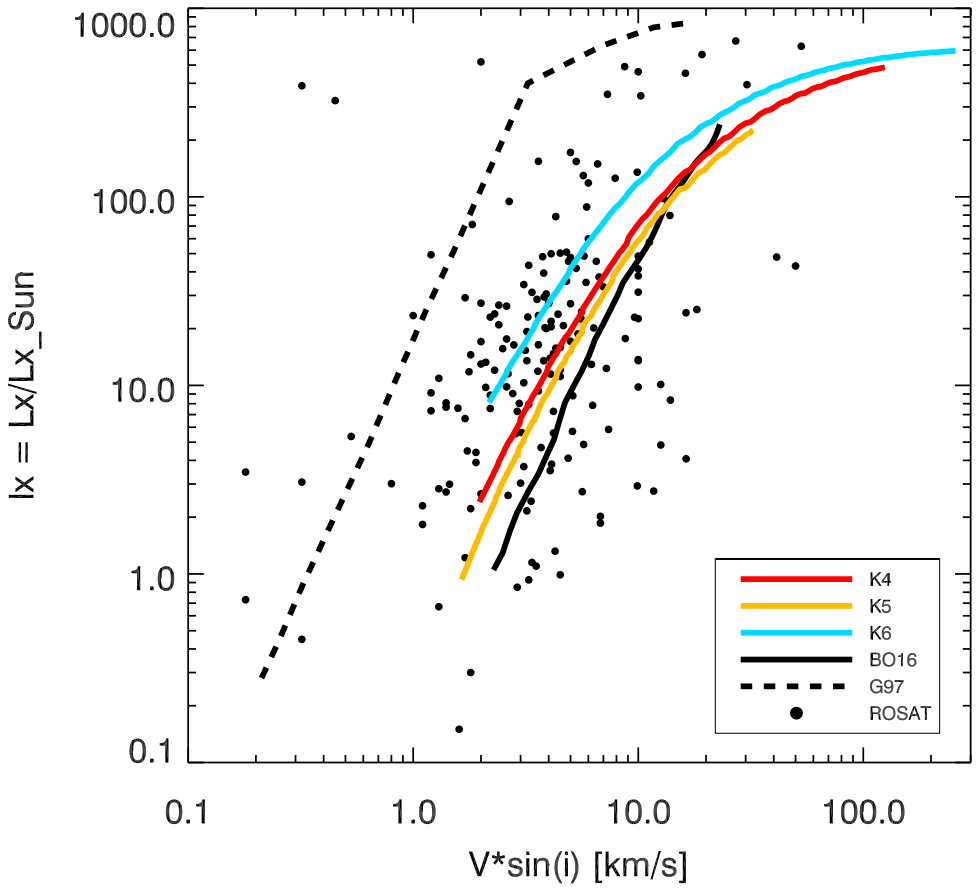

Figure 4.8 Here we compare rotational velocity vs. X-ray luminosity observations with our TYCHO models. We over-plot tracks with three different initial angular velocity values (red produces $\Omega/\Omega_{\odot} \sim 1$ (solar), orange produces $\Omega/\Omega_{\odot} \sim 0.8$, and blue produces $\Omega/\Omega_{\odot} \sim 1.4$) onto the data for ROSAT stars (black circles). Comparisons with Güdel (1997b) (dashed black) and BO16 (solid black) are included.

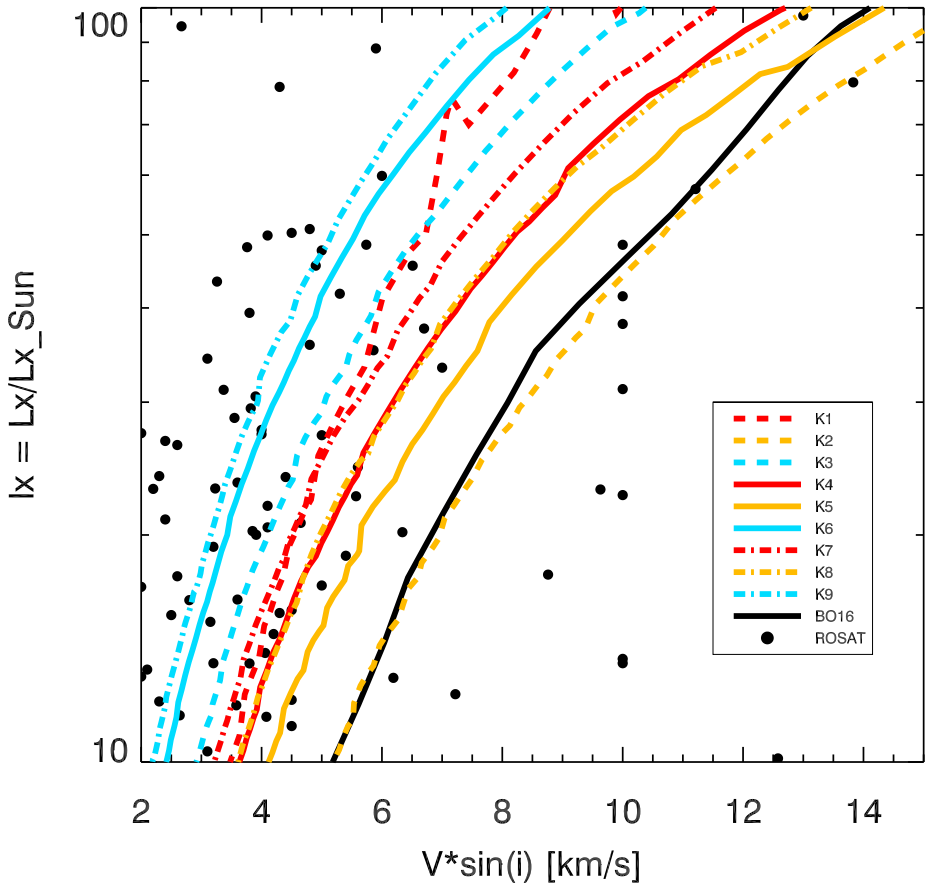

Figure 4.9 Here we compare rotational velocity against X-ray luminosity values. Now that we are zoomed in relative to Figure 4.8, we can appreciate the spread in values of our grid. Even though the nine models in our grid are all for $M_{\odot}$, they show a significant variability in location on this parameter space, based on their overall scaled metallicity values, as well as their initial angular velocity values. Dashed lines are for 0.5 $Z_{\odot}$, solid lines are for 1.0 $Z_{\odot}$, and dashed-dotted lines are for 1.5 $Z_{\odot}$.

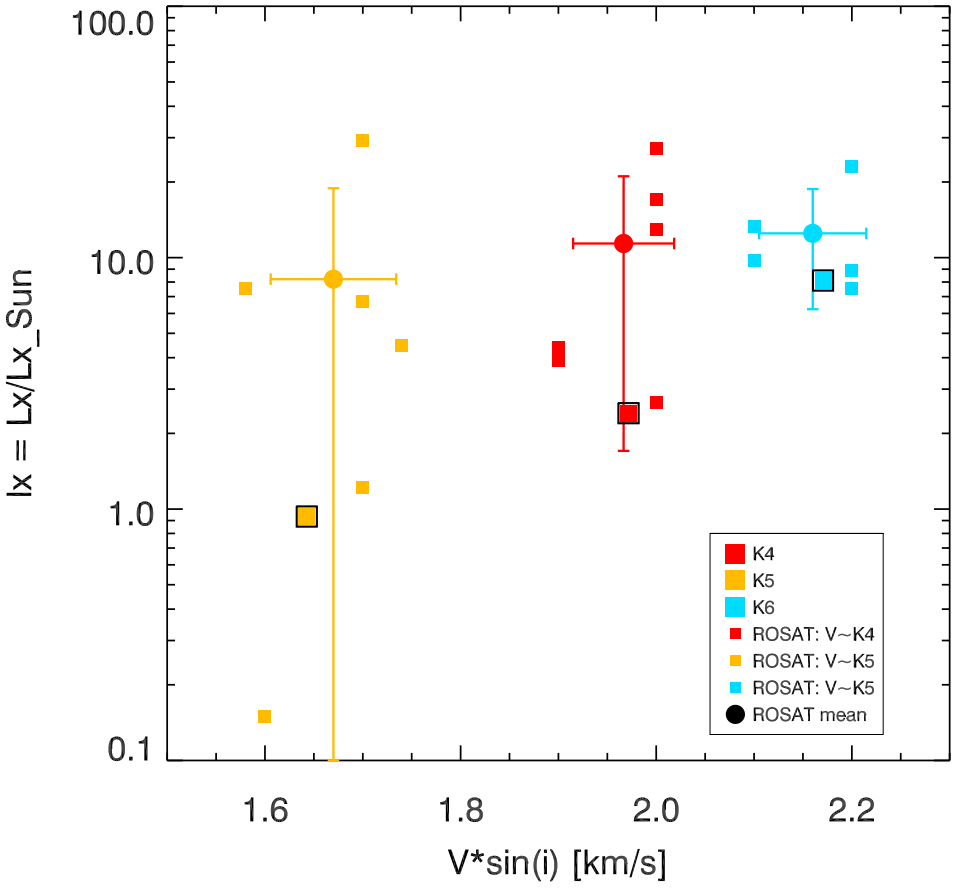

Figure 4.10 Rotational velocity vs. X-ray luminosity. We demonstrate TYCHO can provide relatively accurate predictions of stellar activity values, for solar-type stars. Large squares represent Ω-values at solar age for three TYCHO models at solar mass and $Z_\odot$. Red is $\Omega/\Omega_\odot = 1$, orange is $\Omega/\Omega_\odot \sim 0.8$, and blue is $\Omega/\Omega_\odot \sim 1.4$. The smaller squares are a subset of data points taken from the ROSAT dataset, selected for stars with rotational velocities equal to those of our three rotating solar models. The circles are the average of the observed values, with the standard deviation given by the error bars. Our models are systematically low, but fall within 1σ.

Chapter 5

EXPANDING THE CATALOG III

5.1 A Grid of Low Mass Models & Late-Stage Evolutionary Tracks

In addition to the grid of solar-type stars, consisting of a total of 904 models (detailed in Truitt et al. (2015); Truitt & Young (2017)), we have also created a grid of models for low mass stars, essentially recreating the "original" grid of stars with variations in the overall scaled metallicity (Z) as well as variations in the oxygen, carbon, and magnesium abundances. Again, the scaled Z values range from 0.1-1.5 $Z_{\odot}$, oxygen ranges from 0.44-2.28 $O/Fe_{\odot}$, carbon from 0.58-1.72 $C/Fe_{\odot}$, and magnesium from 0.54-1.84 $Mg/Fe_{\odot}$. We do not include the artificial range of neon abundance values that was discussed in chapter 3; its contribution to the opacity is similar to that of magnesium, so we decided to omit neon from the low mass grid. Instead of 0.5-1.2 $M_{\odot}$ (at Δ 0.1 $M_{\odot}$), the masses now range from 0.1-0.45 $M_{\odot}$ (at Δ 0.05 $M_{\odot}$). Thus we have a total of 856 models in our grid of M-dwarf stars.

We again used the stellar evolution code TYCHO to create this grid of models; TYCHO has always been capable of simulating the stellar evolution down to the hydrogen burning limit, but until recently it was not optimized for very cool, low mass objects like M-dwarf stars. We have implemented improved low temperature opacity tables for stars with very low relative effective temperatures ($\sim$2400 K), which has allowed us to extend our catalog down to include stars of spectral class M8 (approximately). As has been discussed throughout this work, the stellar T_{eff} is an important consideration in the HZ limit calculations, and TYCHO now produces more accurate estimates of low temperature objects.

Ultimately, every track in our entire catalog will be accessible via our online database, but at present there are a few of the low mass models missing (less than 5% of the entire catalog) while we double check that each low mass model has evolved to a sufficiently late stage. This will enable estimates for the habitability potential of planetary systems, with host stars represented by the range of stars in our grid. Some of the models were terminated while still on the MS; although, since these stars are extremely long-lived, it is not an issue if the model has already evolved beyond at least one Hubble time. For example, Figure 5.1 shows the HR diagram for the end-member Z and O/Fe values of interest, for all masses (0.1-0.45 $M_{\odot}$). Each color represents a different mass, and we have blended the tracks such that, rather than a line for each individual case, they demonstrate the full spread of L and T_{eff} that result from the differences in the composition. The tracks that are clearly truncated relative to the fully evolved stars are still representative of over 100 Gyr.

Our eventual goal is to be able to estimate the stellar activity vs. age for each star in this grid. Though, as discussed in chapter 4, we have implemented a new subroutine into TYCHO to allow for coupled calculations of X-ray luminosity, rotation, and mass loss with time, though the model we use has been optimized for estimates of activity for young, solar-type stars. We want to extend our calculations down to include this grid of stars as well if we can perform tests against observations that fall within acceptable error limits, since M-stars require a much more rigorous consideration of their activity levels with time, and how those stellar properties would impact the habitability of any planets orbiting those stars.

We have also included a mini-grid of evolutionary tracks for very evolved stars. We omit 0.5-0.7 $M_{\odot}$ mass values, because they are sufficiently long-lived that modeling evolutionary behavior beyond the MS can be safely neglected. For the remaining mass values 0.8-1.2 $M_{\odot}$ (5 values) we use 5 different compositional values: solar ($Z_{\odot}$), 0.1

$Z_\odot$, 1.5 $Z_\odot$, and then 0.44 $O/Fe_\odot$ and 2.28 $O/Fe_\odot$ (calculated at $Z_\odot$). Thus, the mini-grid is comprised of 25 tracks.

These models may have some interesting implications toward understanding habitability (i.e. considering planetary habitability around a red giant star), but they are mostly intended to broaden the scientific impact of this work overall. This grid of very evolved stars (i.e. into planetary nebula phase) is useful to the wider astronomy community in that it provides accurate stellar evolutionary tracks, particularly to better understand the impact of variable composition in a star, to very late times.

5.2 Element Comparison & Fractional Evolution

It is also important to simultaneously compare how much each element contributes to the overall stellar evolution, by examining the differences in luminosity, effective temperature, and stellar age. Figure 5.2 shows the HR diagram for all elements of interest. As discussed in detail in chapters 2 and 3, oxygen makes the most difference to the evolution of the stellar surface properties, indicated by the purple lines. Neon makes the next largest amount of difference (yellow lines), followed by magnesium (green), and finally carbon makes the least difference (blue). Solar mass/composition is plotted as a solid black line. The dashed lines for each color indicate depleted elemental abundance values, whereas the dotted lines indicate enriched values.

As an additional consideration, we wanted to examine the percent change in L and T_{eff} (relative to solar) for each elemental case based on the total fractional MS lifetime. From TYCHO, we use the HR tracks to find stellar age, L and T_{eff} values. We obtain the "fractional time" by dividing the age at each time-step of the evolution by the individual model's total lifetime. We interpolate age, L, and T_{eff} for fractional times of 0.0-1.0 (i.e. ZAMS to TAMS) in steps of $\Delta 0.1$, and divide the results by the values for solar at each corresponding fractional time. This gives

us a way to normalize changes in L or T_{eff}, since the MS lifetime for each star can vary significantly based on composition. Figure 5.3 shows L (left), T_{eff} (middle), and age (right) vs. the fractional MS lifetime. In L and T_{eff} the solid red line (Z=0.1 $Z_\odot$) is too high to appear on the plot, and for age (t), the line is too low. Table 5.1 provides the "fractional evolution" values for end-member elemental cases of interest, at ZAMS and TAMS. This summarizes how much each element contributes to the overall evolution of each surface property of interest.

Composition	L [Z]	L [T]	T_{eff} [Z]	T_{eff} [T]	age [Z]	age [T]
0.1 $Z_\odot$	1.99	2.34	1.17	1.18	0.57	0.57
0.44 O/Fe$_\odot$	1.12	1.13	1.03	1.02	0.91	0.91
0.50 Ne/Fe$_\odot$	1.03	1.02	1.01	1.01	0.98	0.98
0.54 Mg/Fe$_\odot$	1.03	1.02	1.01	1.00	0.97	0.97
0.58 C/Fe$_\odot$	0.99	1.01	1.00	1.00	1.00	1.00
1.0 $Z_\odot$	1.00	1.00	1.00	1.00	1.00	1.00
1.72 C/Fe$_\odot$	0.99	0.97	0.99	0.99	1.00	1.00
1.84 Mg/Fe$_\odot$	0.95	0.97	0.99	0.99	1.05	1.05
2.00 Ne/Fe$_\odot$	0.94	0.96	0.98	0.99	1.06	1.06
2.28 O/Fe$_\odot$	0.86	0.85	0.96	0.97	1.14	1.14
1.5 $Z_\odot$	0.86	0.84	0.97	0.97	1.11	1.11

Table 5.1 Fractional evolution for L, T_{eff}, and age, for all elements of interest at ZAMS [Z] and TAMS [T]. Table values represent the percent change in the stellar surface parameters over the fractional MS evolution, relative to solar values.

Figure 5.4 shows the inner (solid) and outer (dashed) HZ limits for all elements, at solar mass. This synthesizes the previous discussion on each element's contribution to the evolution of the surface properties, and the HZ location and lifetime. It is clear that O makes the most difference (both because the spread in the O abundance is the largest, as well as its large contribution to opacity per mass), followed by Ne and Mg, and finally C. Recall that our range in Mg is 0.54-1.84 Mg/Fe$_\odot$, while the (artificial) range of Ne is 0.5-2.0 Ne/Fe$_\odot$ – so the larger spread is in Ne, but Mg

contributes more strongly to the opacity; we see that for depleted cases, Mg and Ne are basically identical (orange), though for the inner HZ boundary, where Ne has a slightly larger value, it creates a slightly closer-in and longer-lived HZ. C contributes least to the stellar evolution due to its low opacity per gram, demonstrated by the yellow (0.58 C/Fe$_\odot$) and green (1.72 C/Fe$_\odot$) lines that are extremely close to solar value (black). We find compositional variation impacts both the HZ distance as well as the MS lifetime of a star; oxygen remains the most important individual element to consider, though the other elements discussed are still of marginal significance.

5.3 A Statistical Consideration of the Catalog

Even though our catalog is meant to help characterize potential exoplanetary host stars of interest, it is unlikely that we will always be able to accurately estimate the age of the system. Indeed, one of our previous stipulations that we defined in order to contextualize the 2 Gyr continuously habitable zone (CHZ$_2$) was that we would theoretically be able to measure a particular star's age. Stellar age is relatively easy to calculate for stellar clusters (using the main sequence turn-off), but it is quite difficult to accurately measure the age of an individual star.

Something that we have not previously considered is the very likely situation in which we dont know the precise stellar age, and how we would then estimate the likelihood that at any given time a star would have a planet in the 2 Gyr CHZ. Additionally, we are interested in how we can use existing observational data (i.e. the data assembled in the Hypatia catalog (Hinkel et al., 2014) and the Kepler exoplanet host star database) for a more robust comparison to our grid of theoretical models and evolutionary tracks. Here we briefly discuss a statistical analysis of our catalog and new ways to think about how we should define "continuous" habitability.

5.3.1 Comparing to Observations: Hypatia and Kepler

For the statistical analysis, we started with data from the Hypatia catalog for 3,861 stars with iron abundance measurements that fall within the defined limits of our catalog ($0.1 \leq \text{Fe} \leq 1.5\ \text{Z}_{\odot}$), where we are using the iron abundance as a proxy for overall metallicity (though as we discuss in detail in chapters 2 and 3, this is not an entirely sufficient consideration). Hypatia includes measurements for any element of interest, and it would be important to consider the specific elemental abundance ratios (particularly for oxygen); unfortunately, the Kepler host star dataset only provides measurements for "metallicity" [Fe/H], and thus our closest method for comparison is to use our catalog's overall scaled metallicity value range. We were able to extract a total of 382 host stars from the Kepler exoplanet database that have metallicity measurements between 0.1 and 1.5 $\text{Z}_{\odot}$.

We used bins from 0.1-1.5 and centered on those values, with widths of 0.1 (so the first bin is from 0.05 to 0.15, the second bin is 0.15 to 0.25, etc.). Since the measured abundance values in Hypatia have low precision, they tend to fall exactly on the value in between bins, like 0.15 or 0.25. For each bin division we took all the values at that number and put half of them in the lower bin and the other half in the higher bin. For example, if there were 40 stars with abundance of 0.35, we put 20 of them in the 0.3 bin and 20 in the 0.4 bin. We used the IDL routine KSTWO to compute a Kolmogorov-Smirnov (KS) comparison test (Massey, 1951), which outputs the corresponding initial test D-value, D_{KS}. The KS test compares the cumulative distributions (go through each x-value and cumulatively add up the fraction of data points that are less than or equal to that value), with D_{KS} being the greatest vertical distance between the two dataset distributions. The comparison of the differences between the Kepler and Hypatia datasets is shown in Figure 5.5.

To test for the significance of the D-values, we used the fact that Hypatia has provided us with 3,861 relevant values and Kepler has provided us with 382 relevant values (where relevant simply means the stars meet the criteria for the range we set for our grid of models); we wanted to know what the D-value would be if it was Hypatia being compared with itself (because ultimately the test is to see whether the two datasets exhibit the same distribution). So, we did 10,000 trials, where we selected a random subset of 382 Hypatia values, and did the KS test between the random 382-value subset and the full Hypatia dataset. This represents our ideal D-values, since we know for sure that the subset comes directly from the full dataset. Then, with these 10,000 D-values, we computed the mean and standard deviation and compare that to our original Hypatia-Kepler D-values. Finally, we calculate σ = (D_{KS} - $\langle D_{KS,trial} \rangle$)/$\sigma_{D_{KS,trial}}$; thus, the Hypatia and Kepler data are representative of non-matching distributions at a level of 0.95σ (see Table 5.2).

	KS-Test (D-values)	AD-Test (A^2-values)
Initial values	0.0656673	1.11140
10,000 trials, avg	0.0518119	1.15103
10,000 trials, sig	0.0145691	0.826723
Final distribution	0.951011σ	-0.0479336σ

Table 5.2 Comparing the Distributions of the Hypatia and Kepler Datasets.

We then applied the Anderson-Darling test (Scholz & Stephens, 1987), given by

$$A^2 = \frac{n+m-1}{(n+m)^2}\left(\Sigma_j \frac{h_j((n+m)F_j - nH_j)^2}{H_j(n+m-H_j) - (n+m)h_j/4} + \frac{1}{m}\Sigma_j \frac{h_j((n+m)G_j - nH_j)^2}{H_j(n+m-H_j) - (n+m)h_j/4}\right) \tag{5.1}$$

where j runs over the Fe values (low-to-high); F is the Hypatia set; n is the number of values in F; G is the Kepler set; m is the number of values in G; F_j represents the

number of Hypatia values less than j plus 1/2 of those equal to j; G_j is the same but with Kepler; H_j is the same but with both datasets combined; and h_j is the number of values equal to j from the combined datasets. So, we compute this value, and again do 10,000 more trials comparing a Hypatia subset to itself. A^2 represents non-matching distributions at a level of -0.0479336σ. For the normal standard deviation definition, these values can be translated to mean that the KS-test gives a 34% chance that these two datasets are representative of the same distribution, and the AD-test gives a 96% chance. While these two results differ significantly, neither of them can confidently rule out the possibility that the Kepler and Hypatia datasets are representative of the same distribution. We conclude from these tests that the Hypatia catalog is a fairly good representation of the Fe distribution of the Kepler planet-hosts, and thus we can move forward in comparing these two datasets with our catalog of stellar models.

5.3.2 Habitable Zone Probabilities

Again, it is important to consider habitability in a statistical sense, especially if we don't know the precise age of the stellar system. This is something we did not consider previously; even though we did introduce the discussion about the utility of a 2 Gyr continuously habitable zone (CHZ_2), interpreting whether a planet is in that CHZ requires knowing how far along the star is in its MS evolution. We had assumed we would be able to quantify the stellar age, but that might not always be possible. We have also taken one additional step here, which is to cut off the lifetimes of all stars at the 12 Gyr mark; some of the stars in the catalog are incredibly long-lived (i.e. M-stars can live longer than 100 Gyr), so it does not help much to classify them using the 2 Gyr criteria without imposing an upper limit on lifetime.

Figure 5.6 shows contour plots where the probability of a given orbital distance remaining continuously habitable for at least 2 Gyr is indicated by the color bar at

the top. For the higher scaled Z cases (left), the HZ distance is significantly closer-in and has a higher likelihood of providing a continuously habitable orbit at some point during the MS evolution. On the right is the probability for each mass to provide 2 Gyr continuously habitable orbits. Note, there is no 12 Gyr age cut applied to the figure on the left, because at 1 $M_\odot$ no models live longer than 12 Gyr. Also, it is clear that low mass stars are much more likely to provide long-term continuously HZs, even if you were to observe a planet around this star at any random point in the star's MS lifetime. Alternatively, the probability for finding a 2 Gyr CHZ for a more massive star decreases significantly, even though there are distances where the HZ limits at ZAMS and TAMS overlap. We have also included relevant planetary data from the NASA exoplanet archive, over-plotted on the contour plot that demonstrates the probability of finding a 2 Gyr CHZ for each mass in our range, shown in Figure 5.7.

To compute the 2 Gyr HZ statistical probabilities, we first create radius bins from 0-10 in steps of 0.01. We step through each star's evolution in the TYCHO output (HR) file; at each stellar age, we measure whether the radius falls within the calculated HZ limits, and if it remains for at least 2 Gyr, then we add the current time-step to that bin. For each model, we end up with the amount of time that each orbital radius is in the HZ for at least 2 Gyr, and we also know the total lifetime of each model. We thus calculate the HZ probability plots for two cases: (1) holding mass constant at M = 1 $M_\odot$, with a spread in metallicity Z = 0.1-1.5 $Z_\odot$; and (2) holding metallicity constant at $Z_\odot$, with a spread in mass M = 0.5-1.2 $M_\odot$. To combine the various models in a case, we add up the total time in all models spent in each radius bin, and divide the results by the total time of all models added up; see Figure 5.8 for case 1 (left) and case 2 (right).

Finally, we incorporated the Hypatia Fe distribution into a combined plot by taking the fraction of the Hypatia stars in each of our Z-value bins (0.1-1.5 with 0.1 bin

size) normalized to 1. While combining the metallicity models (as described above for case 1), we multiplied the radial 2 Gyr HZ fractions by the corresponding normalized Hypatia bin value, again dividing by total time of all the models. This results in a 2 Gyr HZ probability curve, weighted by the Hypatia metallicity distribution (Figure 5.9) rather than the distribution achieved by weighting each Z-value equally (notice the slight difference from the left panel of Figure 5.8).

We have created HZ probability plots for M = 0.5-1.2 $M_{\odot}$ and Z = 0.1-1.5 $Z_{\odot}$. We combined the processes described above for case 1, and we do it for each mass from 0.5 to 1.2. We take the resulting combined curves and apply them to the contour process described in the previous paragraph (Figure 5.10, top left). We apply the weighted Hypatia distribution (Figure 5.10, top right), also with the 12 Gyr cut-off imposed. Additionally, we over-plot Kepler planets (similar to Figure 5.7) with the the non-Hypatia contours on the bottom left, and Hypatia contours with planets on the bottom right. Note that the probability distributions for our catalog (i.e. equally weighting metallicity values between 0.1-1.5 $Z_{\odot}$) vs. the probability distribution for the Hypatia catalog (using observations to weight the distribution) are quite similar to each other. The major difference is that for the Hypatia contours, the probability of finding a planet in a 2 Gyr CHZ is slightly greater up to 1 $M_{\odot}$. Finally, since we've compared the Kepler exoplanet host star distribution with the distribution observed in Hypatia, it's reasonable to expect that host stars of the included planets could be well-represented by the stellar evolutionary tracks in our catalog.

5.4 Summary and Synthesis

As an important and useful aid in the general assessment of habitability potential for a given star, I have created a flowchart (Figure 5.12) that synthesizes our results so that they can be easily and directly utilized by the scientific community. The

mass and metallicity ranges that are referenced in the flowchart represent the range of models that are included in the catalog of stellar evolutionary tracks.

In order to gauge the relative habitability potential for different cases (low Z, high Z, and unknown Z) I calculated the fraction of the total MS lifetime (during the first 12 Gyr) that a planet would spend in the HZ for at least 2 Gyr, averaged in 8 mass and distance bins, represented by the white grid spaces in Figure 5.11. For each distance bin and each mass, I averaged the confidence fraction across the bin, given by the statistical probability values (color bar at the top) and divided by the total width of the bin, resulting in the overall average lifetime fractions for each mass-distance region in the plot. The distance bins have a width of 0.6 AU, and the mass bins are split into low mass (0.5-0.8 $M_{\odot}$) and high mass (0.9-1.2 $M_{\odot}$), for simplicity. The upper left panel of Figure 5.11 is for the low metallicity case (0.1-0.8 $Z_{\odot}$), the upper right panel is for the high metallicity case (0.8-1.5 $Z_{\odot}$), and the bottom panel represents the Hypatia Catalog statistical distribution (i.e. if we don't know the metallicity of the star). The numbers in each grid are the average values I used for ranking potential host stars of interest in the flowchart (see Figure 5.12).

Higher numbers in Figure 5.11 indicate more promising locations for the long-term habitability of orbiting exoplanets, based on the statistical probability from the mass and metallicity considerations discussed throughout this work. Values from 0-0.1 are indicated by red boxes on the flowchart, 0.1-0.2 is orange, 0.2-0.3 is light green, and greater than 0.3 are the dark green boxes. For this consideration, I have used only the overall scaled metallicity (Z-)values relative to solar, since this makes the most difference to the stellar evolution, after mass. Though the individual specific elemental abundances that I have considered at length in this work (oxygen, carbon, magnesium, and neon) are certainly important to consider, including them here would only serve to confuse the flowchart. Changing the oxygen abundance alone, for example, would

provide similar effects that we see with the overall scaled metallicity; effects from the other elements would be small enough to be negligible for the purposes of using the flowchart for a broad-stroke assessment of host star habitability potential.

According to the flowchart, if it is unknown whether a particular star has any planets, or the distances of those planets is not well-constrained, one would be better off looking at higher mass stars in general, not only because of their larger HZs, but also because they are relatively shorter-lived than the very low mass stars, so the chances that the HZ has evolved farther out is higher than for the slow-evolving low mass stars. Also, as discussed in chapters 2 and 3, the probability of a planet entering the HZ after the midpoint of the star's MS lifetime is much lower for higher mass stars, which is advantageous if we want to generally avoid planets that have only recently entered the HZ. Even though lower mass stars are statistically more likely to remain continuously habitable for very long times, they should not necessarily be considered as the best host star candidates by default (see Figure 5.12 and note red boxes associated with low mass stars).

Additionally, it is important to note that the flowchart does not yet take stellar activity into account, because we have not finished the extensive testing in TYCHO that will be necessary to confidently estimate activity over the stellar evolution, except for the Sun (i.e. we can not yet say what kind of changes in stellar activity we will see for 0.5 $M_{\odot}$, or 1.2 $M_{\odot}$). However, activity will need to be a fundamental component to consider as we attempt to assess the habitability of any particular stellar system; as I discussed in chapter 4, low mass stars are known to be quite active throughout their lifetimes (generally more than solar-type stars), which could result in the low mass stars on the flowchart to become less promising than they are currently listed.

As an exercise in the utility of the flowchart, I will compare two Kepler host stars with known Earth-sized planets: Kepler 442b and Kepler 453b (Table 5.3).

	Kepler 442b	Kepler 453b
Semi-major Axis	0.4 AU	0.8 AU
Stellar Mass	0.6 $M_\odot$	0.9 $M_\odot$
Metallicity (Z)	0.43 $Z_\odot$	1.2 $Z_\odot$

Table 5.3 Data for Two Kepler Exoplanet Host Stars.

Using the flowchart in Figure 5.12 with this data, we begin in the upper left corner: the chart asks whether the star of interest hosts any exoplanets with known distances. Both of our sample stars do, and so we follow the YES path. Next, we are asked if we know the metallicity of the host stars – we do for both, and again we follow the YES path. Now, we first consider Kepler 442b, and take the Low Z path (as 0.43 $Z_\odot$ falls between 0.1-0.8 $Z_\odot$). The planet's orbital distance is given as 0.4 AU, so we look at the box that ranges from 0.2-0.8 AU; this has two branches for each the low and high mass cases. This particular star is considered low mass in our sample (falls between 0.5-0.8 $M_\odot$) and we find a dark green box, indicating that this system is "promising" based on the models in our catalog and the statistical probabilities for continuous habitability that I have discussed in this chapter.

Next, we consider Kepler 453b, which takes us along the High Z path (1.2 $Z_\odot$ falls between 0.8-1.5 $Z_\odot$). We now have a distance value of 0.8 AU, which brings us to an interesting juncture: since 0.8 is a dividing value between two bins, we could go to either to 0.2-0.8 AU box, or the 0.8-1.4 AU box. If we choose the 0.8-1.4 bin, and follow along to the next box for mass (note: 0.9 $M_\odot$ is considered "high mass" here) we find that we have again reached a dark green "promising" box; however, if we choose the 0.2-0.8 bin, then we find a result of red, or not very promising. In this case, we should likely consider the star that falls solely into a green box more promising than the one that lies in the division between green and red. This illustrates

a potential shortcoming of this kind of assessment; however, the main utility of this flowchart is not to provide a completely accurate description of all the ways in which one star is a better target than another (this should instead be done using the more detailed results presented throughout this work), but rather to give a quick, simple indication that one star may be a much more promising candidate than another.

Overall, a statistical approach to understanding the habitability potential of host star candidates is an important consideration. Since our catalog of stellar evolutionary models represent the spread in values observed in the mass and metallicity of real host star candidates, we can now better use the database of tracks (and the flowchart that attempts to synthesize all of our results) to help assess the long-term habitability potential of a given planetary system. This kind of assessment also gives us more analytical power, since we don't need to know every single parameter of interest in order to gauge the habitability of a stellar system; specifically, since stellar age is difficult to measure accurately, we can still estimate the likelihood for any planets in the system to remain habitable for at least 2 Gyr. Additionally, with the flowchart, we now provide a quick and efficient method for observers to directly compare the estimated habitability potential for exoplanet host stars of interest.

This research has made use of the NASA Exoplanet Archive, which is operated by the California Institute of Technology, under contract with the National Aeronautics and Space Administration under the Exoplanet Exploration Program.

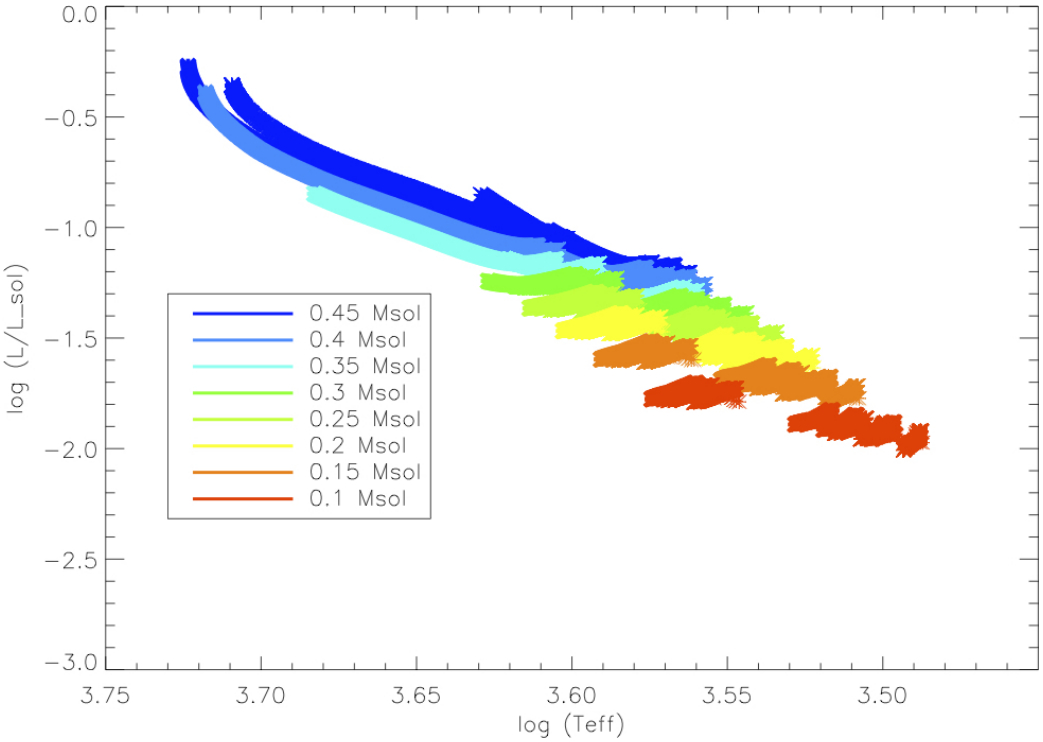

Figure 5.1 HR diagram for the end-member abundance values of oxygen and scaled metallicity, for all mass values in our grid of low mass stars, 0.1-0.45 $M_{\odot}$. The bands of each color represent all compositional models for each corresponding mass value. For the lowest mass (red) it is easiest to see the spread in T_{eff} (less spread in L) that results from variations in metallicity and elemental abundance ratios.

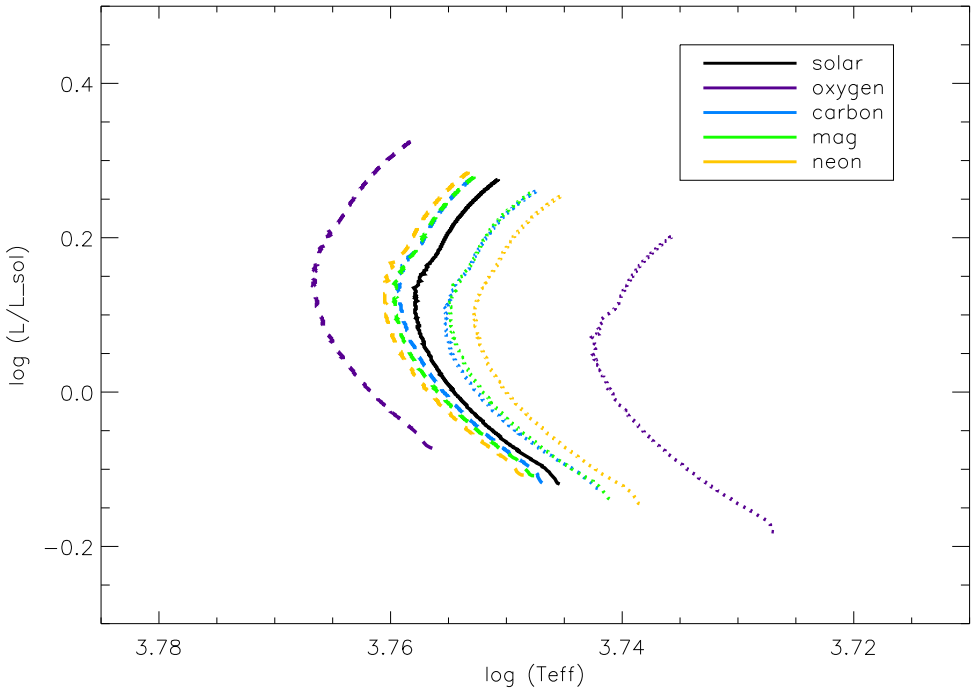

Figure 5.2 HR diagram for end-member cases (at solar Z), demonstrating variation in stellar surface properties over the evolution. End-member values of abundance ratios are as follows: 0.44-2.28 $O/Fe_{\odot}$; 0.58-1.72 $C/Fe_{\odot}$; 0.54-1.84 $Mg/Fe_{\odot}$; the representative range for neon, 0.5-2.0 $Ne/Fe_{\odot}$. Dashed lines are for depleted values, dotted lines are for enhanced values, black line is solar value.

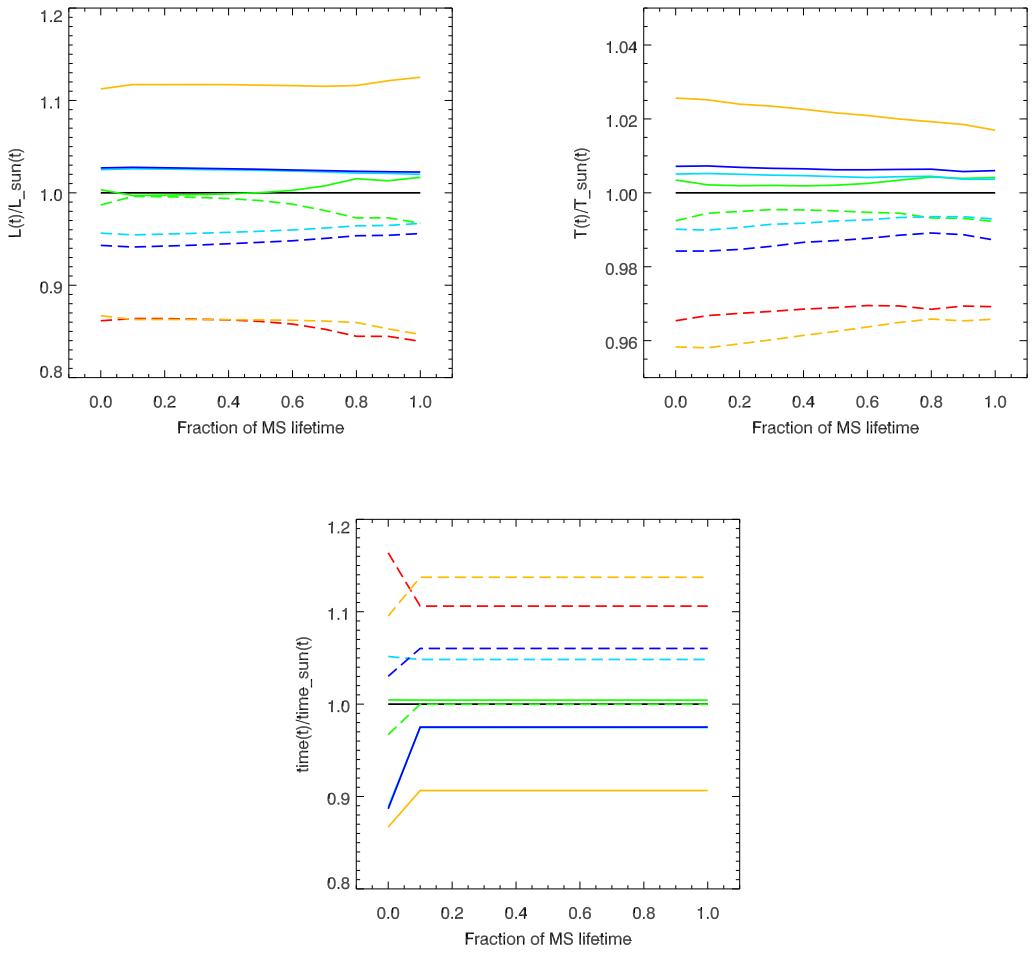

Figure 5.3 Fraction of the MS lifetime for different element end-member cases of interest. Left is luminosity, middle is temperature, right is time (age). The black line in each is solar; red is 1.5 $Z_{\odot}$ (0.1 $Z_{\odot}$ plots out of range); orange is oxygen; green is carbon; light blue is magnesium; and blue is neon. Solid lines indicate low abundance ratio values, and dashed lines are high abundance ratio values.

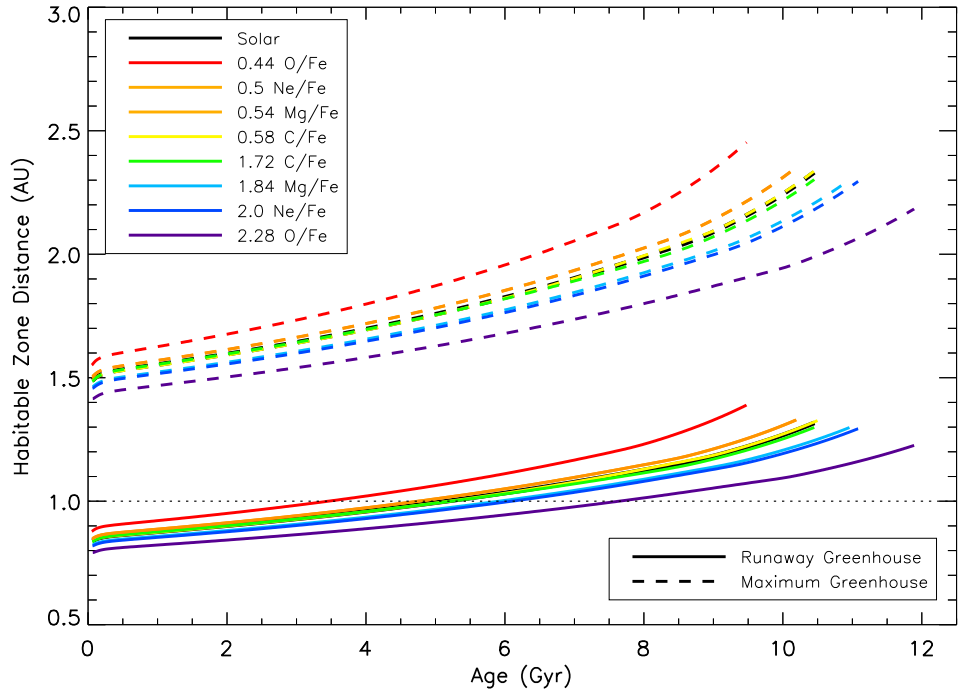

Figure 5.4 Inner (solid) and outer (dashed) edges of the HZ for solar mass, at each end-member element value of interest. Red and purple represent 0.44 and 2.28 O/Fe$_{\odot}$, respectively; orange represents both 0.5 Ne/Fe$_{\odot}$ and 0.54 Mg/Fe$_{\odot}$ (essentially indistinguishable) while the enriched values (1.84 Mg/Fe$_{\odot}$ and 2.0 Ne/Fe$_{\odot}$) are represented by light blue and dark blue, respectively. Finally, yellow and green represent 0.58 and 1.72 C/Fe$_{\odot}$, respectively, which are close enough to solar value (black) that the line is almost obscured. A 1 AU orbit is indicated by the dotted line.

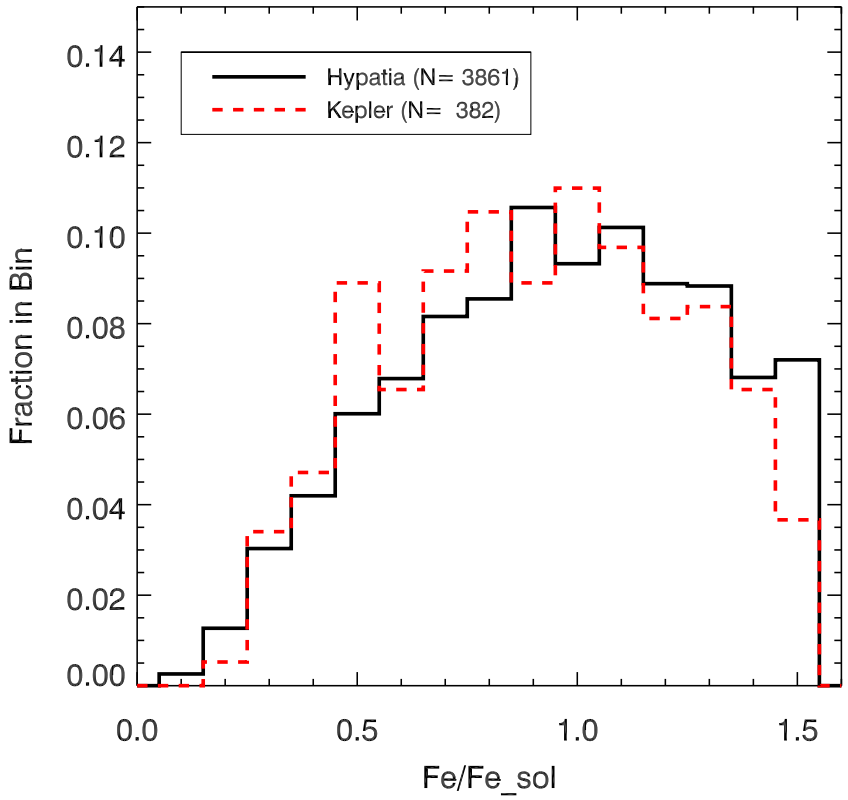

Figure 5.5 KS-Test comparing subset of Kepler host stars with the Hypatia catalog.

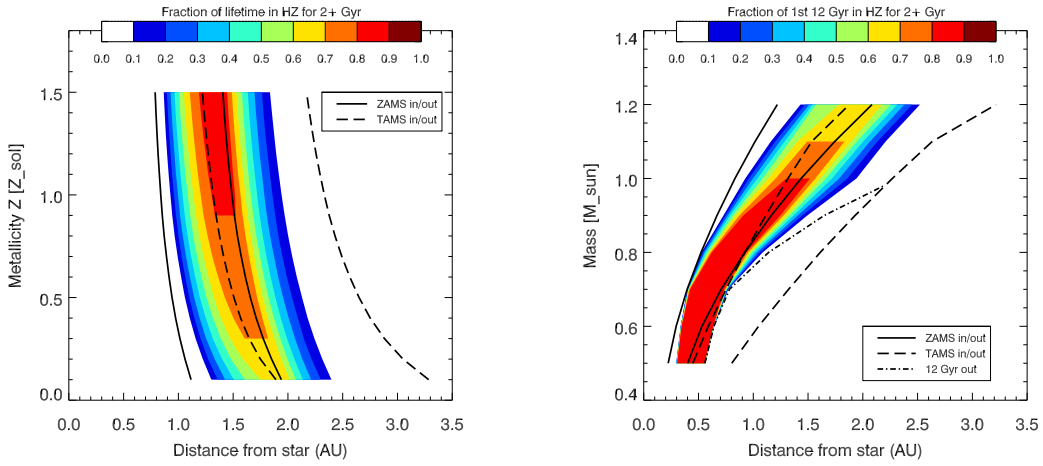

Figure 5.6 Probability of a particular orbital distance remaining continuously habitable for at least 2 Gyr, indicated by the color bar at the top. Left: metallicity vs. HZ distance; right: mass vs. HZ distance.

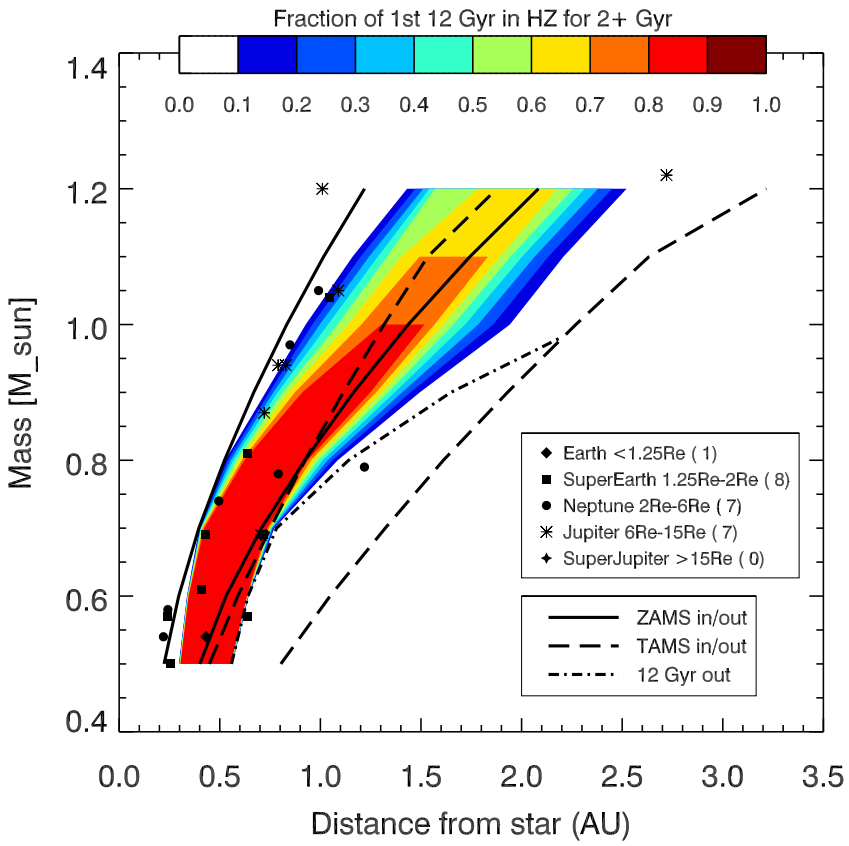

Figure 5.7 Planetary data from the NASA exoplanet archive, over-plotted. Again, a 12 Gyr cut-off has been applied for the lower mass stars. It is clear that most of the available data that falls in our range of habitable distances is for super-Earths, or Neptune-sized planets. These kinds of planets may or may not be "habitable" by the classical definition of habitability.

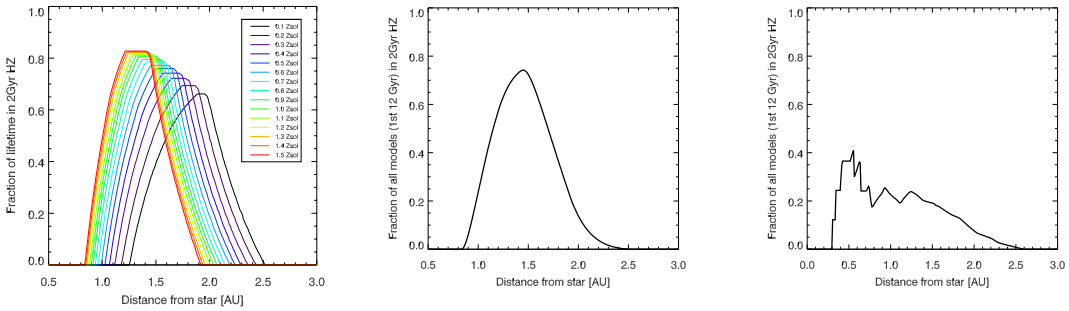

Figure 5.8 Left: fraction of the lifetime for each Z-model where a given distance would be in the HZ for at least 2 Gyr, assuming an unknown stellar age and metallicity, and assuming all Z-values are equally likely. M=1 $M_{\odot}$, 0.1 $Z_{\odot} \leq Z \leq 1.5$ $Z_{\odot}$. Middle: average of left panel, all Z-models. Right: Now for $Z = Z_{\odot}$, 0.5 $M_{\odot} \leq M \leq 1.2$ $M_{\odot}$. Since low mass stars are very long-lived, all models are considered only for the first 12 Gyr of their lifetimes. This represents the probability that a given distance around a 1 $Z_{\odot}$ star has been in the CHZ for at least 2 Gyr, assuming age and mass are unknown, and M-values from 0.5-1.2 $M_{\odot}$ are equally likely.

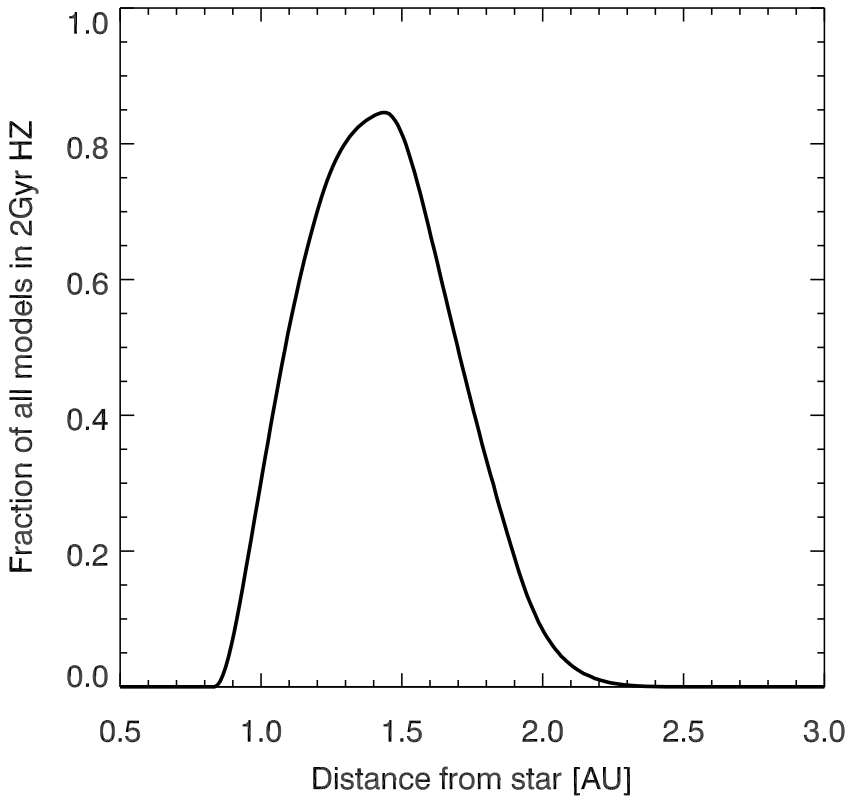

Figure 5.9 Now, the fraction of the total time of all M = $M_{\odot}$, weighted by the metallicity distribution of the Hypatia catalog. Again, this represents the probability that a given distance around a 1 $M_{\odot}$ star has been in the HZ for at least 2 Gyr, assuming the star's age *and* metallicity are unknown; we no longer consider that all Z-values from 0.1-1.5 $Z_{\odot}$ are equally likely as in Figure 5.8, rather, we use the actual distribution observed in the Hypatia catalog.

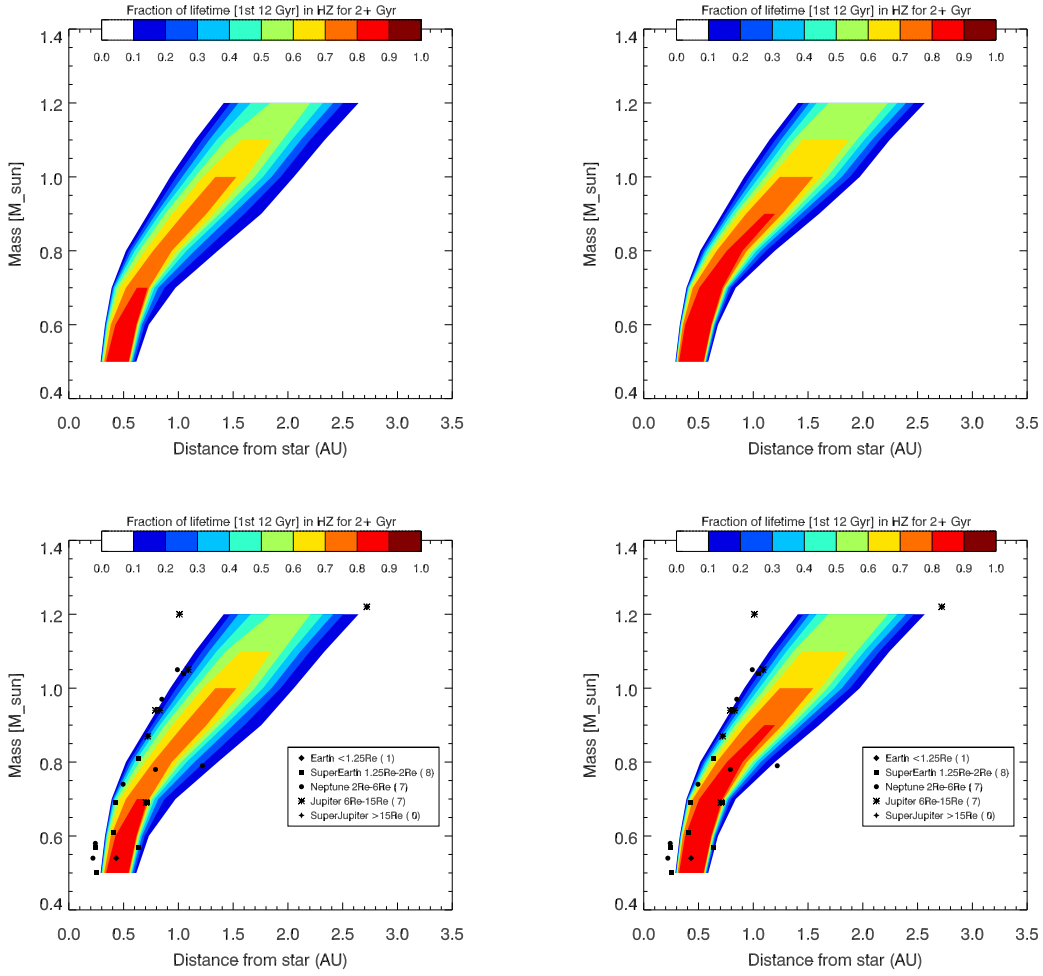

Figure 5.10 Top left: probability distribution for our catalog, if you did not know the stellar age or the precise metallicity measurement of the star; top right: probability distribution for the Hypatia catalog; bottom left: non-Hypatia contours with planet distribution over-plotted; bottom right: Hypatia contours with planets. The right-side panels include the 12 Gyr cut-off for the MS lifetime.

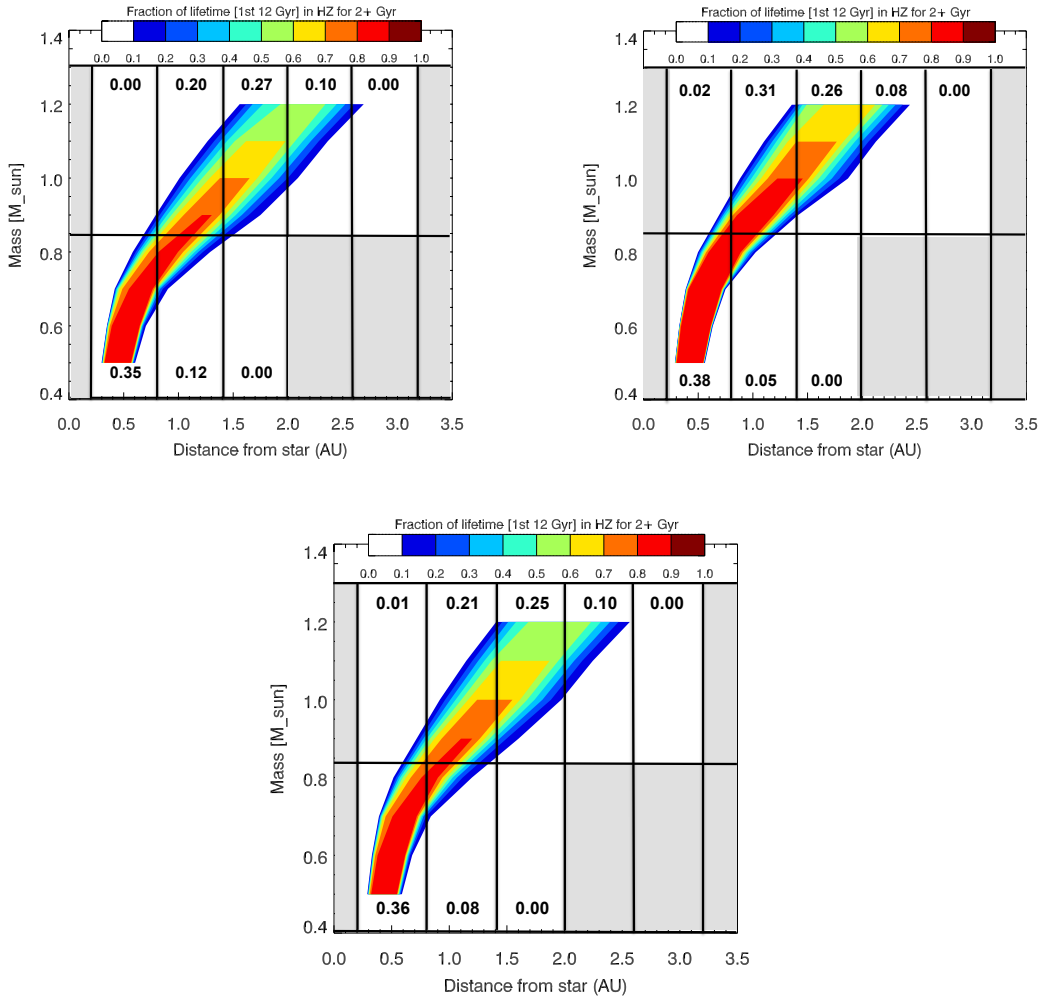

Figure 5.11 Fraction of lifetime (in the first 12 Gyr) a planet would spend in the HZ for at least 2 Gyr, averaged in 8 mass and distance grids. Distance bins have a width of 0.6 AU, and the mass bins are split into low mass (0.5-0.8 $M_{\odot}$) and high mass (0.9-1.2 $M_{\odot}$). Upper left is for the low metallicity case (0.1-0.8 $Z_{\odot}$), upper right is high metallicity (0.8-1.5 $Z_{\odot}$), and the bottom panel represents the Hypatia Catalog distribution (if we don't know the metallicity of the star). The numbers in each grid are used for ranking potential host stars of interest in the flowchart (Figure 5.12).

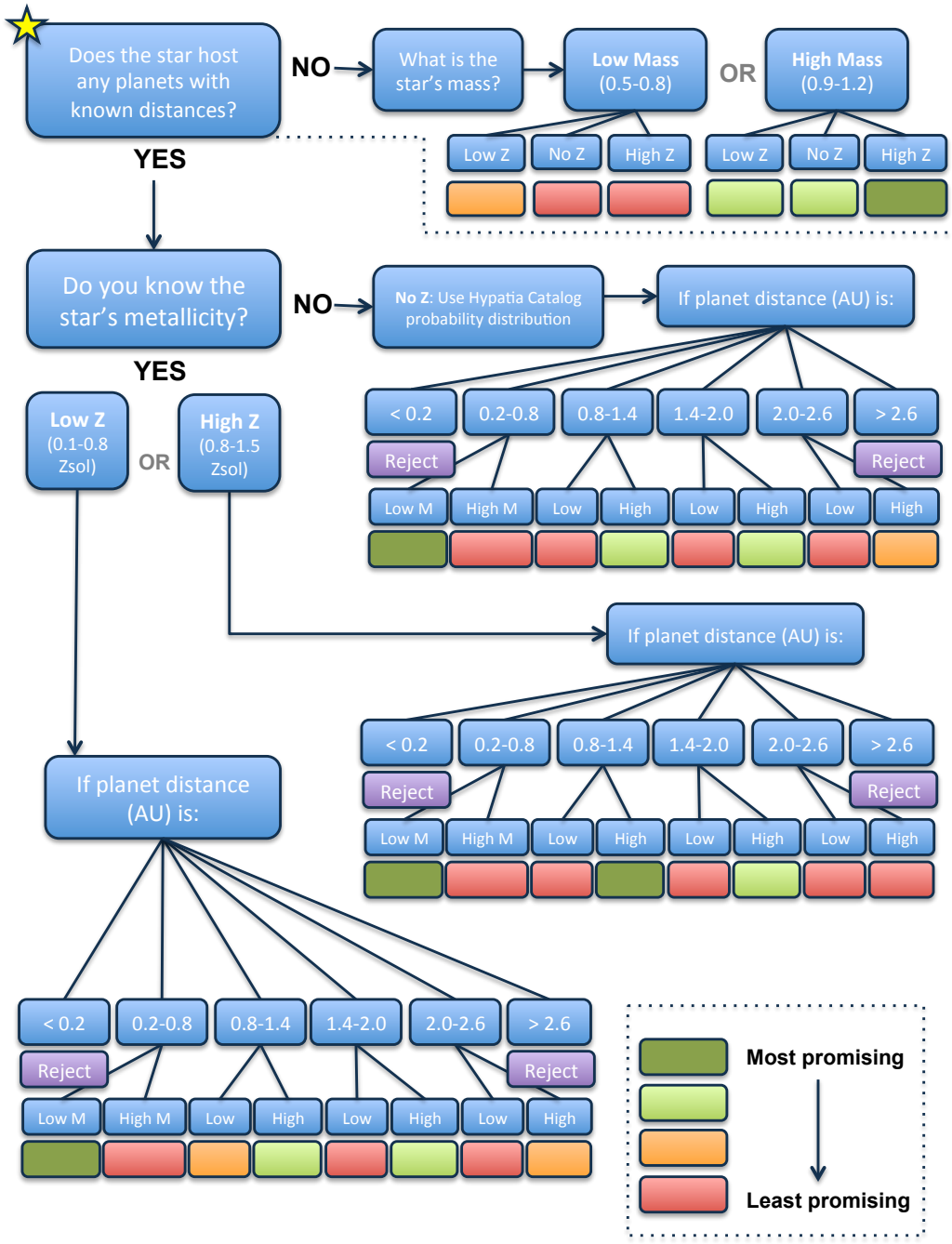

Figure 5.12 Flowchart for a general comparison of the habitability potential of a given host star. Based on a synthesis of my results, the mass and metallicity ranges referenced here represent the models included in the catalog of stellar evolution tracks. Here, dark green is most favorable, red is least favorable (see Figure 5.11).

Chapter 6

FINALE

I have presented the results of my work on modeling the stellar evolution for a large grid of low-mass and solar-type stars, using TYCHO. What has not been widely recognized before this work, and what I discuss at length in chapters 2 and 3 of this dissertation, is that it is important to consider the specific abundance ratio values present in individual stars, as well as the overall scaled metallicity (Z) value relative to solar; both of these properties can significantly influence the main sequence (MS) evolution of stars, due to differences in the stellar opacity.

I focused particularly on how variations in oxygen, carbon, magnesium, and neon at levels similar to those observed in nearby stars impact the stellar evolution, and how they compare if we instead only consider a range of scaled Z-values. An increase in oxygen, for example, increases the total heavy element abundance; however, the opacity will be different for different mixes of elements with the same integrated heavy element abundances, because certain elements contribute differently to the overall opacity per unit mass. Furthermore, if model comparisons with individual stars are made based only on the measured abundance of iron in the star ("metallicity" is often used interchangeably with [Fe/H]) and just assuming other elements are proportional to solar value, very large errors may be present.

I find that, of the elements in my study, oxygen makes the most difference in the stellar evolution, both because it is typically quite abundant in stars (preceded only by hydrogen and helium), and because of its high opacity per unit mass. Carbon is next in relative abundance, though we find that both neon and magnesium provide a larger contribution to stellar opacity and thus introduce greater changes to the MS lifetime,

L, and T_{eff} compared to carbon. For this set of elemental abundance ratios, the effects on lifetimes and luminosities are generally smaller than typical observational uncertainties. As discussed in this work, Gaia data will allow for higher precision distance measurements, and much more accurate determination of stellar luminosity values; the dominant source of error will thus become bolometric corrections. The effect of carbon abundance ratios will still likely be enough to be negligible, but the specific oxygen and magnesium abundance ratios in stars should certainly still be taken into account. Neon would also produce significant changes to the stellar surface properties over the MS evolution; even though it is very difficult to acquire precise abundance measurements of neon, it should definitely be included in any uncertainty estimates for quantities derived from stellar models.

Given the classical definition of the habitable zone (HZ) as simply the distance from a star at which liquid water would be stable on a planet's surface, the properties of the host star are of fundamental importance. I have approached the problem of planetary habitability from the astrophysical perspective, with a rigorous method that includes not only compensating for differences in stellar mass and metallicity, but also how variations of individual elements contribute to the evolution of an entire planetary system. For low opacities, MS lifetimes are shorter and the total L change over the MS is larger. This results in a relatively rapid change in the location of the HZ, which has obvious implications for how long a planet at a particular orbital distance will remain in a host star's continuously habitable zone (CHZ). Evaluating the long-term habitability potential of a system thus requires a robust characterization of the host star, and measurements of multiple elemental abundances.

We know that on Earth, the timescale for life to establish itself on the surface and significantly alter the atmosphere (such that it might be detectable via transmission spectroscopy) took approximately 2 Gyr. We have therefore proposed a 2 Gyr CHZ to

more efficiently estimate the habitability potential of a given system. This is a useful condition, though it may not be sufficient to describe the long-term habitability of a low-mass star (due to the extremely long lifetime as well as potential for high activity levels). Additionally, if a planet is located currently in the CHZ_2, it doesn't necessarily mean it should be treated as a good candidate for habitability; imagine a planet entering the HZ late in the star's MS lifetime, when it may be "geologically" dead. This and other characteristics of the planet, such as whether its atmosphere been stripped by high activity levels of the host star, are several other important aspects of habitability that should be considered.

Toward that end, I have recently implemented a minimalist coupled model for stellar activity, rotation, and mass loss into TYCHO. My goal, beyond extending TYCHO's capabilities to characterize stellar evolution even more completely, is to further assess the habitability potential of any given planetary system. With the updates to the code, I am able to not only estimate changes in the host star's temperature and luminosity over time (based on mass and composition), but I can also calculate how the stellar activity changes with increasing stellar age. M-dwarfs in particular are of great concern to many astronomers who are interested in probing the habitability around these stars, because their high levels of activity (e.g. high-energy X-ray emission) may ultimately negate the benefits of their extremely long MS lifetimes (in terms of whether they can provide a stable environment for the development of life on a planet) even if an orbiting planet is located in the star's CHZ for billions of years. Moreover, M-stars are observed to have fairly variable activity levels, even among stars of roughly the same age and spectral type. Although it may be difficult to estimate activity versus age for very low-mass stars, incorporating this model to TYCHO will at least allow for estimates of activity versus age for solar-type stars, which may be more homogenous in their early activity levels than M-dwarfs.

For this dissertation, I have created a catalog of precise stellar evolution tracks for a large grid of solar-type and low mass stars, which are publicly available in an online database. The database includes an interactive interpolation tool that allows the user to plot evolutionary tracks and HZs for a star at any combination of the main stellar parameters (mass, metallicity, specific abundance), of particular benefit to the astrobiology and exoplanet communities who may need to characterize a planetary system for a specific host star of interest. I have also created a flowchart that synthesizes the results of my work, which is again intended to help assess the habitability potential of a given system. Though the flowchart does not yet take stellar activity into account (as we have not done the necessary testing in TYCHO to confidently estimate how changes in stellar activity may impact planetary habitability over time) it is a useful consideration that allows for a quick and efficient method to estimate the habitability potential of candidate host stars. The main utility is for comparisons between two or more host star candidates, to help characterize which might be the more promising system; the flowchart also takes into account statistical probabilities for which systems are most likely to be the best candidates for long-term habitability, even if the user does not know the precise age or metallicity of the star.

I have argued that a host star's evolution and the time-dependent evolution of the associated HZ are of particular importance to consider in tandem with each new discovery of an exoplanet that may be *currently* in its parent star's HZ. Additionally, with my recent work on updating TYCHO to allow for the evolution of stellar activity, I have considered the impact this kind of activity might have on a planetary system as a whole. Habitability is a complex topic, and there are other criteria to consider as we work toward defining a planet's habitability, including the interior composition of the planet, the presence and/or composition of the planetary atmosphere, and the evolution of an atmosphere as it interacts with the circumstellar environment.

The latter is a topic that I am interested in pursuing in the future, potentially working to further refine the updates I have recently implemented in TYCHO to produce even more accurate models for stellar activity with time. This work is significant, in that no one has ever studied the co-evolution of stars and HZs based predominantly on the spread of specific individual elemental abundance ratios that are observed within stars. I have considered not only how the stellar evolution directly influences the location of the HZ around a star, but also how the lifetime of the HZ can change at different rates. This is a crucial factor to consider as we continue to search for a potentially habitable Earth-like planet.

REFERENCES

Airapetian, V. S., Glocer, A., Khazanov, G. V., et al. 2017, ApJL, 836, L3

Alexander, D. R. & Ferguson, J. W. 1994, ApJ, 437, 879

Allard, F. & Hauschildt, P. H. 1995, ApJ, 445, 433

Anbar, A. D., Duan, Y., Lyons, T. W., et al. 2007, Science, 317, 1903

Angulo, C., Arnould, M., Rayet, M., et al. 1999, Nucl. Phys. A, 656, 3

Arnett, D. 1996, (In:) Supernovae and Nucleosynthesis: An Investigation of the History of Matter, from the Big Bang to the Present, Princeton University Press

Arnett, D., Meakin, C., & Young, P. A. 2009, ApJ, 690, 1715

Arnett, D., Meakin, C., & Young, P. A. 2010, ApJ, 710, 1619

Arnett, D. & Meakin, C. 2011, ApJ, 733, 78

Aschwanden M. J., 2004, Physics of the Solar Corona. An Introduction. Praxis Publishing Ltd; Chichester, UK

Bailer-Jones, C.A.L. 2009, The Galaxy Disk in Cosmological Context, 254, 475

Barnes, S. A. & Kim, Y.-C. 2010, ApJ, 721, 675-685

Barstow, J. K. & Irwin, P. G. 2016, MNRAS: Letters, slw109

Batalha, N. M., Rowe, J. F., Bryson, S. T., et al. 2013, ApJS, 204, 24

Beom, M., Na, C., Ferguson, J. W., et al. 2016, ApJ, 826, 2

Bibring, J. P., Langevin, Y., Mustard, J. F., et al. 2006, Science, 312, 400

Blackman, E. G. & Owen, J. E. 2016, MNRAS, 458, 1548

Bond, J. C., Tinney, C. G., Butler, R. P., et al. 2006, MNRAS, 370, 163

Bond, J. C., Lauretta, D. S., Tinney, C. G., et al. 2008, ApJ, 682, 1234

Borucki, W. J., Koch, D., Basri, G., et al. 2010, Science, 327, 977

Borucki, W. J., Koch, D., Basri, G., et al. 2011, ApJ, 736, 19

Brocks, J. J., Logan, G. A., Buick, R., et al. 1999, Science, 285, 1033

Buccino, A. P., Lemarchand, G. A., & Mauas, P. J. D. 2006, Icarus, 183, 2

Buccino, A. P., Lemarchand, G. A., & Mauas, P. J. D. 2007, Icarus, 192, 582

Caldeira, K. & Kasting, J. F. 1992, Nature, 359, 226

Catanzarite, J. & Shao, M. 2011, ApJ, 738, 151

Charpinet, S., Fontaine, G., Brassard, P., et al. 2011, Nature, 480, 496

Cranmer, S. R. & Saar, S. H. 2011, ApJ, 741, 54

Crowe, S. A., Døssing, L. N., Beukes, N. J., et al. 2013, Nature, 501, 535

Danchi, W. C. & Lopez, B. 2013, ApJ, 769, 27

Domagal-Goldman, S. D., Segura, A., Claire, M. W., et al. 2014, ApJ, 792, 90

Dong, C., Jin, M., Lingam, M., et al. 2017, arXiv:1705.05535

Dotter, A., Chaboyer, B., Ferguson, J. W., et al. 2007, ApJ, 666, 1

Drake, J. J., & Testa, P. 2005, Nature, 436, 525

Feigelson, E. D., Hornschemeier, A. E., Micela, G., et al. 2004, ApJ, 611, 1107

Ferguson, J. W., Alexander, D. R., Allard, F., et al. 2005, ApJ, 623, 585

Forget, F. & Pierrehumbert, R. T. 1997, Science, 278, 1273

Forget, F. 2013, International Journal of Astrobiology, 12, 177

France, K., Froning, C. S., Linsky, J. L., et al. 2013, ApJ, 763, 149

Fressin, F., Torres, G., Rowe, J. F., et al. 2012, Nature, 482, 195

Gaidos, E. 2013, ApJ, 770, 90

Gallet, F., Charbonnel, C., & Amard, L. 2016, Orig Life Evol Biosph 46 (4), 395-401

Gallet, F., Charbonnel, C., Amard, L., et al. 2017, A&A, 597, A14

Geiss, J. & Bochsler, P. 1991, The Sun in Time, 98

Gillon, M., Triaud, A. H., Demory, B. O., et al. 2017, Nature, 542, 7642

González Hernández, J. I., Israelian, G., Santos, N. C., et al. 2010, ApJ, 720, 1592

Graboske, H. C., Dewitt, H. E., Grossman, A. S., et al. 1973, ApJ, 181, 457

Gregory, S. G. 2016, arXiv:1612.04587

Grevesse, N., & Sauval, A. J. 1998, Space Science Reviews, Springer, v. 85, Issue 1/2

Grevesse, N., Asplund, M., & Sauval, A. J. 2007, Space Sci. Rev., 130, 105

Güdel, M., Guinan, E. F., & Skinner, S. L. 1997b, ApJ, 483, 2

Güdel, M. 2004, A&A, 12, 71

Güdel, M. 2007, Living Reviews in Solar Physics, 4, 3

Güdel, M., Dvorak, R., Erkaev, N., et al. 2014, Protostars and Planets VI, 883

Guo, J., Zhang, F., Zhang, X., et al. 2010, Astrophys Space Sci, 325: 25

Hansen, C. J., Kawaler, S. A., & Trimble, V. 2004, (In:) Stellar Interiors: Physical Principles, Structure, and Evolution (2nd ed.), Springer, 19

Harman, C. E., Schweiterman, E. W., Schottelkotte, J. C., et al. 2015, ApJ, 812, 2

Hawley, S. L. 1993, PASP 105(691), 955

Hinkel, N. R., Timmes, F. X., Young, P. A., et al. 2014, AJ, 148, 54

Hinkel, N. R., Turnbull, M. C., Mamajek, E. E., et al. 2017, In Prep. "Properties for FGK-Stars Within 30pc: The ASU NExSS Database CATSUP"

Holland, H. D. 2006, Phil. Trans. R. Soc. B, 361, 903

Iglesias, C. A. & Rogers, F. J. 1996, ApJ, 464, 943

Iliadis, C., D'Auria, J. M., Starrfield, S., et al. 2001, ApJS, 134, 151

Jackson, A. P., Davis, T. A., & Wheatley, P. J. 2012, MNRAS, 422, 3

Johnstone, C. P., & Güdel, M. 2015, A&A, 578, A129

Jones, B. W., Sleep, P. N., & Underwood, D. R. 2006, ApJ, 649, 1010

Kaltenegger, L., Eiroa, C., Ribas, I., et al. 2009, Astrobiology, 10, 1

Kane, S. R. 2014, ApJ, 782, 111

Kane, S. R., Hill, M. L., Kasting, J. F., et al. 2016, ApJ, 830, 1

Kasting, J. F. 1988, Icarus, 74, 472

Kasting, J. F. 1991, Icarus, 94, 1

Kasting, J. F. & Grinspoon, D. H. 1991, The Sun in Time, 447

Kasting, J. F. 1993, Science, 259, 920

Kasting, J. F., Whitmire, D. P., & Reynolds, R. T. 1993, Icarus, 101, 108

Kasting, J. F. & Catling, D. 2003, Annu. Rev. Astron. Astrophys, 41, 429

Kasting, J. F., Kopparapu, R. K., Ramirez, R. M., et al. 2014, PNAS, 111, 12641

Kim, Y.-C. & Demarque, P. 1996, ApJ, 457, 340

Kopp, R. E., Kirschvink, J. L., Hilburn, I. A., et al. 2005, PNAS, 102, 11131

Kopparapu, R. K., Ramirez, R. M., Kasting, J. F., et al. 2013, ApJ, 765, 131

Kopparapu, R. K., Ramirez, R. M., SchottelKotte, J., et al. 2014, ApJL, 787, L29

Kraft, R. P. 1967, ApJ, 150, 551

Krissansen-Totton, J., Schwieterman, E. W., Charnay, B., et al. 2016, ApJ, 817,1

Lammer, H., Güdel, M., Kulikov, Y. et al. 2012, Earth Planet Sp, 64: 13

Landin, N. R., Mendes, L. T. S., & Vaz, L. P. R. 2010, A&A, 510, A46

Langanke, K. & Martínez-Pinedo, G. 2000, Nucl. Phys. A, 673, 481

Lebreton, Y., Michel, E., Goupil, M. J., et al. 1995, Astronomical and Astrophysical Objectives of Sub-Milliarcsecond Optical Astrometry, 166, 135

Lodders, K. 2010, In: Principles and Perspectives in Cosmochemistry, Astrophysics and Space Science Proceedings, Springer-Verlag Berlin Heidelberg, 379

Luger, R. & Barnes, R. 2015, Astrobiology, 15, 2

Mamajek, E. E., & Hillenbrand, L. A. 2008, ApJ, 687, 1264-1293

Massey, F. J. 1951, Journal of the American Statistical Association, 46, 253

Meakin, C. A. & Arnett, D. 2007, ApJ, 667, 448

Mishenina, T. V., Soubiran, C., Bienaymè, O., et al. 2008, A&A, 489, 923

Morse, P. M. 1940, ApJ, 92, 27

Morton, T. D., Bryson, S. T., Coughlin, J. L., et al. 2016, ApJ, 822, 86

Neves, V., Santos, N. C., Sousa, S. G., et al. 2009, A&A, 497, 563

Newton, E. R., Irwin, J., Charbonneau, D., et al. 2016, ApJl, 821, L19

Oishi, M., & Kamaya, H. 2016, Astrophysics and Space Science, 361(2) 1-6

O'Malley-James, J. T., & Kaltenegger, L. 2017, MNRAS, 469, L26

Pace, G., & Pasquini, L. 2004, A&A, 426, 1021

Pagano, M. D., Truitt, A., Young, P. A., et al. 2015, ApJ, 803, 90

Pallavicini, R., Golub, L., Rosner, R., et al. 1981, ApJ, 248, 279

Parker, E. N. 1955, ApJ, 121, 491

Parker, E. N. 1970, ApJ, 160, 383

Petigura, E. A., Howard, A. W., & Marcy, G. W. 2013, PNAS, 110, 19273

Pinsonneault, M. H., Kawaler, S. D., & Demarque, P. 1990, ApJS, 74

Pollack, J. B., Kasting, J. F., Richardson, S. M., et al. 1987, Icarus, 71, 203

Preibisch, T. & Feigelson, E. D. 2005, ApJS, 160, 390

Ramírez, I., Allende Prieto, C., & Lambert, D. L. 2007, A&A, 465, 271

Ramírez, I., Meléndez, J., & Asplund, M. 2009, A&A, 508, 17

Rauscher, T. & Thielemann, F. K. 2000, Atomic Data & Nuclear Data Tables, 75, 1

Reiners, A. & Mohanty, S. 2012, ApJ, 746, 43

Ribas, I., Guinan, E. F., Güdel, M., & Audard, M. 2005, ApJ, 622, 680

Rogers, F. J., Swenson, F. J., & Iglesias, C. A. 1996, ApJ, 456, 902

Rogers, F. J. & Nayfonov, A. 2002, ApJ, 576, 1064

Rushby, A. J., Claire, M. W., Osborn, H., et al. 2013, Astrobiology, 13, 833

Scholz, F. & Stephens, M. 1987, Journal of the American Statistical Assoc., 82, 399

Segura, T. L., Toon, O. B., Colaprete, A., et al. 2002, Science, 298, 1977

Segura, T. L., Toon, O .B., & Colaprete, A. 2008, J. Geophys. Res., 113, E11007

Segura, A., Walkowicz, L. M., Meadows, V. 2010, Astrobiology, 10, 7

Selsis, F., Kasting, J. F., Levrard, B., et al. 2007, A&A, 476, 1373

Serenelli, A. M., Basu, S., Ferguson, J. W., et al. 2009, ApJL, 705, 123

Serenelli, A. 2016, EPJ, A, 52(4), 1-13

Shields, A. L., Ballard, S., & Johnson, J. A. 2016, arXiv:1610.05765

Shkolnik, E. L., & Barman, T. S. 2014, AJ, 148, 64

Silva, L., Vladilo, G., Schulte, P. M., et al. 2016, arXiv:1604.08864

Simon, T., Herbig, G., & Boesgaard, A. M. 1985, ApJ, 293, 551

Skumanich, A. 1972, ApJ, 171, 565

Solomon, S. C. & Head, J. W. 1991, Science, 252, 252

Summons, R. E., Jahnke, L. L., Hope, J. M., et al. 1999, Nature, 400, 554

Sung, H., Bessell, M. S., & Sana, H. 2008, JKAS, 41, 1

Takeda, Y. 2007, PASJ, 59, 335

Tarter, J. C., Backus, P. R., Mancinelli, R. L., et al. 2007, Astrobiology, 7, 1

Telleschi, A., Güdel, M., Briggs, K. R., et al. 2005, ApJ, 622, 653

Telleschi, A., Güdel, M., Briggs, K. R., et al. 2007, A&A, 468, 425

Testa, P., Saar, S. H., & Drake, J. J. 2015, Phil. Trans. R. Soc. A, 373

Thoul, A. A., Bahcall, J. N., & Loeb, A. 1994, ApJ, 421, 828

Timmes, F. X. & Arnett, D. 1999, ApJS, 125, 277

Truitt, A., Young, P. A., Spacek, A., et al. 2015, ApJ, 804, 145

Truitt, A., & Young, P. A. 2017, ApJ, 835, 87

Turnbull, M. C., Glassman, T., Roberge, A., et al. 2012, PASP, 124, 418

Vaiana, G. S., Cassinelli, J. P., Fabbiano, G., et al. 1981, ApJ, 245, 163

Valle, G., Dell'Omodarme, M., Prada Moroni, P. G., et al. 2014, A&A, 567, A133

Valle, G., Dell'Omodarme, M., Prada Moroni, P. G., et al. 2015, A&A, 575, A12

VandenBerg, D. A., Bergbusch, P. A., Dotter, A., et al. 2012, ApJ, 755, 15

Vidotto, A. A., Jardine, M., Morin, J., et al. 2013, A&A, 557, A67

Vidotto, A. A. 2014, ASTRA Proceedings, 1, 19

Vidotto, A. A. 2016, 19th Cambridge Workshop on Cool Stars (CS19), 147

von Paris, P., Cabrera, J., Godolt, M., et al. 2011, A&A, 534, A26

Wenger, M., Ochsenbein, F., Egret, D., et al. 2000, A&A, 143, 9

Wiescher, M., Azuma, R. E., Gasques, L., et al. 2006, Mem. S.A.It., 77, 910

Wolff, S., & Simon, T. 1997, PASP, 109, 759

Wood, B. E., Mueller, H., Zank, G. P., et al. 2005, ApJL, 628, L143

Wordsworth, R. & Pierrehumbert, R. 2014, ApJL, 785, L20

Wright, N. J., Drake, J. J., Mamajek, E. E., & Henry, G. W. 2011, ApJ, 743, 48

Yang, J., Cowan, N. B., & Abbot, D. S. 2013, ApJL, 771, L45

Young, P. A. & Arnett, D. 2005, ApJ, 618, 908

Young, P. A., Liebst, K., & Pagano, M. 2012, ApJ, 755, 31

Young, P. A., Desch, S. J., Anbar, A. D., et al. 2014, Astrobiology, 14, 553

Zendejas, J., Segura, A., & Raga, A. C. 2010, Icarus, 210, 539

Ziegler, C., Law, N. M., Morton, T., et al. 2017, AJ, 153, 66

APPENDIX A

INTERACTIVE HABITABLE ZONE DEMONSTRATION

Introduction

This activity uses a hands-on physical model to illustrate the concept of the classical habitable zone to participants in either an unstructured informal education or classroom setting. Patrick Young and I designed and built this activity in the fall of 2015, based on concepts outlined in this work, with assistance in circuitry layout and assembly by Alex Spacek and Anusha Kalyaan. We have had the opportunity to test the utility of this demonstration at several ASU outreach events, including the"Earth and Space Exploration (ESE) Day" and "Night of the Open Door."

Building the Activity

Figure A.1 shows a rough sketch of the diagram that we used to assemble the circuit boards. We used three circuit boards with 9 V batteries, operational amplifiers, resistors, switches, and photosensitive diodes. These diodes generally allow more current through them the more light that shines on them, represented by I3 in Figure A.1. We linked the output voltages to a digital voltmeter display. We used different combinations of resistors (R1, R2, R3, and R4 in Figure A.1) to create different sensitivity ranges for each circuit board, such that the same amount of light results in different voltage outputs. The resistors must be chosen carefully so that the power through each ($P = I^2R$) never exceeds 0.25 W, the typical power limit for resistors. We also needed at least 20 mA of current (I3) for our digital reader to work. Putting all of this together allowed us to use three of the same flashlights to represent the three different kinds of stars (which would differ in brightness) resulting in variations in the amount of energy the "planets" appear to receive. The basic idea of the circuit is to use an operational amplifier to take in the voltage from a 9 V battery and output a range of voltages to a voltmeter display depending on the

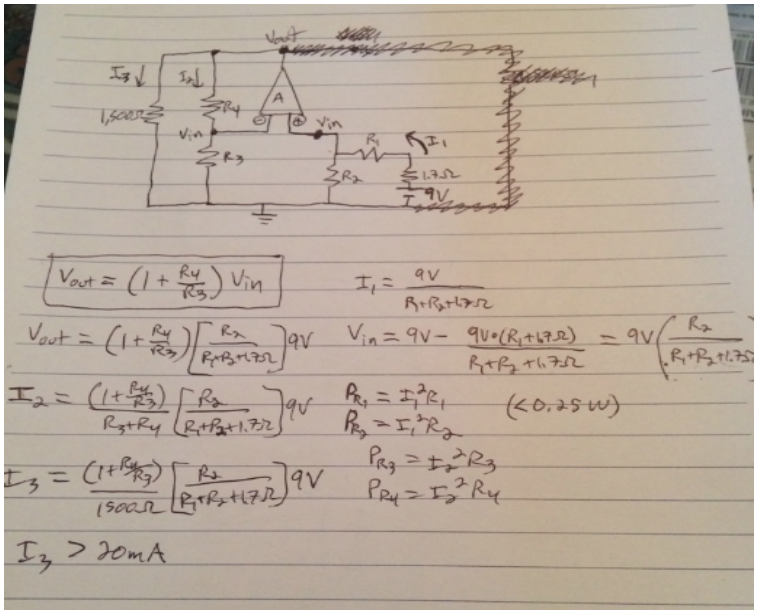

Figure A.1 Rough sketch of proposed circuit diagram during initial planning phase.

amount of light shining on a photodiode. The circuit, specifically the resistors used, is calibrated for each "planet" to output a certain voltage at a certain distance.

Figure A.2 shows the final circuit board (left) plus the mounting that we used to attach the sliding planet on the end (right). The circuit board hides behind the folding panel of the activity, so that only the planet and digital display is visible. The user can then slide the circuit board (which is why we attached felt sliders on the bottom) to move the photosensitive piece back and forth, which would cause the display to change as it responded to how much light from the flashlight it received, based on distance (as in Figures A.3 and A.4).

Learning Objectives

* Different stars have different brightnesses

* The amount of energy a planet receives goes down the farther it is from its star

* Planets around dim stars must be closer to the star to receive the same amount of

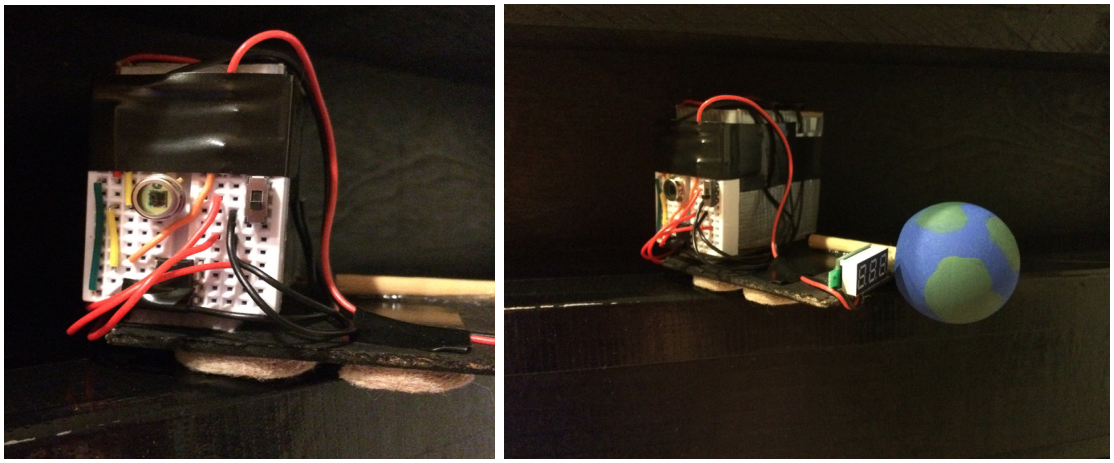

Figure A.2 Left: the photosensitive diode (circular piece) is clearly visible on the circuit board – this side faces the flashlight and measures light received. Right: we can see the planet "handle" and the digital LCD voltmeter, which displays amount of "energy" received by the planet at any given distance from the "star".

light as a planet at a given distance from a brighter star

* To support life like Earth, a planet cant receive too much or too little energy. There is a habitable zone at a specific range of distances from the star

* The HZ around a dim star is closer to the star than one around a bright star

This activity consists of a single, self-contained unit and requires only a suitable table or other platform for display and use. The three flaps with green squares can be raised to access the flashlights and light meter circuits. Both need to be turned on and off when beginning and ending the activity. The flashlight batteries will provide sufficient power for about two hours of use. It is recommended that spare batteries be kept with the activity. Ensure that the flashlights are aligned exactly horizontally.

With the flashlights and light meter switched on, the digital displays will show a number in arbitrary units indicating how much light they are receiving. The green squares representing the habitable zone have been placed such that the displays will

report approximately the same number for all three stars when the planet is within the habitable zone. The blue disk represents the brightest, hottest, most massive star, followed by the yellow, then the red. Important note: As the batteries in the flashlights are drained, the lights will become dimmer, and the numbers on the displays will become smaller at a given distance with time. This is normal operating behavior for the system. This occurs on a much longer timescale than it take for a person or group to do the activity, so it does not affect the procedure. It is, however, important to bring spare batteries!

Utility for Outreach

We introduce the topic by inquiring whether the participant has heard of planets around other stars or if they have ever wondered whether there is life on other planets. This can eventually segue into the question of whether your location ever seems too hot or too cold to live in. Use this to suggest whether there could be an entire planet could be too hot or cold for life. What determines the temperature of a planet?

We discuss several ideas, including the fact that the amount of energy received by a planet in orbit around a star varies with distance; now it is time to get the participant to interact with the activity. Participants can slide the planets along their tracks and watch the numbers change on the digital display. How do they think the amount of light a planet receives affects its temperature?

It is important to talk about different kinds of stars, and how it is possible that they can have different brightnesses. We ask the participants which kind of star they think is the brightest, and then tell them they actually have the chance to test their hypothesis via the interactive demo. Pick one star (red, yellow, or blue) and have the participant read off the number on the light meter. They should then move the other two planets to the same distance from their stars and compare the numbers on

the display. The blue star will display the highest number, followed by the yellow, followed by red. How does this compare to their guess?

It will become clear after moving the "planets" back and forth along their tracks for awhile, that a planet around a dim star needs to be closer to receive the same amount of energy (light) as a planet around a brighter star (see Figure A.3). Now ask if the participant thinks the planets around the dimmer stars can receive as much energy as the planet around the brighter star. Do they need to be closer, or farther away? Let them experiment. As long as the brighter stars planet is sufficiently far out, they will discover that they can make the numbers match up. You may need to adjust the bright stars planets position before this step.

Finally, we can introduce the idea of the "Habitable Zone" and remind the participant of the idea that a planet might be too hot or too cold for life. Where in the stellar system would it be too hot? Too close to the star, or too far out? How about too cold? Refer back to their answers to previous questions when guiding them. When they have the idea, explain that the green areas on the panel of the activity represent the range of distances at which a planet is not too hot and not too cold. Would they expect the planets to receive the same amount of light in the habitable zone for each star? Let them test their hypothesis. If they wanted to look for planets with life, where would they look? This has many potential implications to lead to a much more complex astrobiology-related discussion.

My experience working with kids and this activity has been entirely favorable; during the Earth and Space Exploratin (ESE) day 2015, we had many people come by the Astrobiology outreach table to play with the demo, and afterward, they were all able to discuss the big-picture ideas that they learned (see Figures A.4 and A.5). I believe that this demonstration is a clear and concise method with which we can attempt to communicate a relatively complex idea. It is fun for the kids because

Figure A.3 We attempted to calibrate the Habitable Zone distances based on the digital output on the LCD display. Each different "star" would produce a different amount of "energy" on the display, based on how we configured each circuit board. The small, red star shows a HZ distance much closer-in than for the larger, blue star.

they have a planet to slide around on a track with easily visible changes, and it is fun for me that I can talk with younger people about my research in an easy-to-understand way. This activity is successful at breaking down a complicated topic into basic smaller parts, slowly building up to a broader discussion about planetary habitability, concepts of astrobiology, and the potential for life in the Universe.

Figure A.4 Setting up the Astrobiology outreach table, Earth and Space Exploration (ESE) Day 2015, which includes our interactive HZ activity. We painted on green sections on the activity to represent the habitable zones, or basically the distance around each "star" where the digital output would be roughly the same value.

Figure A.5 Patrick Young discusses the activity with visitors to the Astrobiology outreach table, Earth and Space Exploration (ESE) Day 2015.